UNIVERSITY OF CALIFORNIA,
IRVINE

Laser-Foil Interactions with Space-Time Coupled Beams

DISSERTATION

submitted in partial satisfaction of the requirements
for the degree of

DOCTOR OF PHILOSOPHY

in Physics

by

Eric Carl Nelson

Dissertation Committee:
Professor Christopher P. J. Barty, Chair
Professor Franklin Dollar
Professor Howard Lee

2024

DEDICATION

To Emily, my twin sister

TABLE OF CONTENTS

LIST OF FIGURES

LIST OF TABLES

ACKNOWLEDGMENTS

I would like to thank my advisor, Chris Barty, for the opportunity to conduct a variety of research projects and pursue work that I found interesting. I've learned invaluable lessons about being a scientist and how to present my work in a meaningful way.

I would like to thank my friends and family for their support on this journey. I have met many wonderful people that have contributed to countless memories that I will forever cherish. The days of working long hours were made much easier with other members of the lab nearby. Being able to discuss projects, workshop ideas, and get feedback from them has been instrumental.

I would like to also thank Skyworks Cafe. They truly had good food for affordable prices.

Chapter 4 of this dissertation is a reprint of the material as it appears in [1], used with permission from Optica Publishing Group. The co-authors listed in this publication are Kyle Chesnut, Trevor Reutershan, Haytham Effarah, Kyle Charbonnet, and Christopher P. J. Barty.

VITA

Eric Carl Nelson

EDUCATION

Doctor of Philosophy in Physics **2024**
University of California, Irvine *Irvine, California*

Bachelor of Science in Physics (Minor in Mathematics) **2017**
University of Michigan, Dearborn *Dearborn, Michigan*

RESEARCH EXPERIENCE

Graduate Research Assistant **2019–2024**
University of California, Irvine *Irvine, California*

TEACHING EXPERIENCE

Teaching Assistant **2017–2019**
University of California, Irvine *Irvine, California*

REFEREED JOURNAL PUBLICATIONS

Pulse front distortions in focused spatially chirped beams **2024**
Optics Continuum

High-density dynamics of laser wakefield acceleration from gas plasmas to nanotubes **2021**
MDPI Photonics

REFEREED CONFERENCE PUBLICATIONS

Space-Time Correlated Foci of Exotic Spatially Chirped Femtosecond Beams **Mar 2023**
Ultrafast Optics XIII

ABSTRACT OF THE DISSERTATION

Laser-Foil Interactions with Space-Time Coupled Beams

By

Eric Carl Nelson

Doctor of Philosophy in Physics

University of California, Irvine, 2024

Professor Christopher P. J. Barty, Chair

This thesis presents a computational study on the propagation effects of space-time coupled laser beams, their interaction with thin hydrogen foils, and the resulting effect on accelerated protons. Laser-plasma simulations are typically done using particle-in-cell codes where analytic descriptions of Gaussian beam propagation, that make assumptions on the frequency dependent nature of ultrashort pulses, are used. A code was developed using Fourier propagation techniques that accurately describes the diffractive effects of arbitrary focused fields which was implemented into a particle-in-cell code. The accurate model shows varying laser-matter interaction dynamics compared to the approximated fields. The Fourier propagation code also enables the study of focused spatially chirped beams generated from the output of a single-pass, two-grating compressor. These fields have a space-time coupling that exhibit a pulse front tilt and pulse front curvature depending on the gratings used to generate them. When focused onto a hydrogen target, enhanced collimation and increased proton energies beyond that of a Gaussian beam are possible. Axisymmetric extensions of these space-time fields enable the generation of highly collimated proton jets. The results of this thesis provide insight into the effects accurate laser modeling and space-time couplings have on laser accelerated ions.

Chapter 1

Introduction

1.1 Laser Based Ion Acceleration

The advent of Chirped Pulse Amplification [2] (CPA) has pushed ultrashort lasers into a regime where peak intensities of $> 10^{18}\ W/cm^2$ are readily achieved. With this advancement, many application spaces have become available. The application that will be the focus of this thesis is laser based ion acceleration, where an intense, petawatt (PW) laser pulse in the near-infrared range (800 nm -1000 nm) that is on the order of $10^{18}\ W/cm^2$ or greater, interacts with a foil and ionizes and subsequently accelerates electrons and ions [3]. The ions that get accelerated currently have energies 10s of MeV to 100s of MeV depending on the type of acceleration mechanism they undergo. There are two primary applications of high energy protons that are of interest: proton therapy and fast ignition.

1.1.1 Proton Therapy

When protons propagate through media, they deposit dose at a very particular depth that depends on their energy. A dose-depth curve relates the energy to the depth and dose deposited. The dose-depth curve for three electron energies (5 MeV, 15 MeV, and 150 MeV), one photon energy (2.5 MeV), one proton energy (150 MeV), and one carbon ion energy (250 MeV) are visualized in Fig. 1.1. The proton and carbon ion beam have a

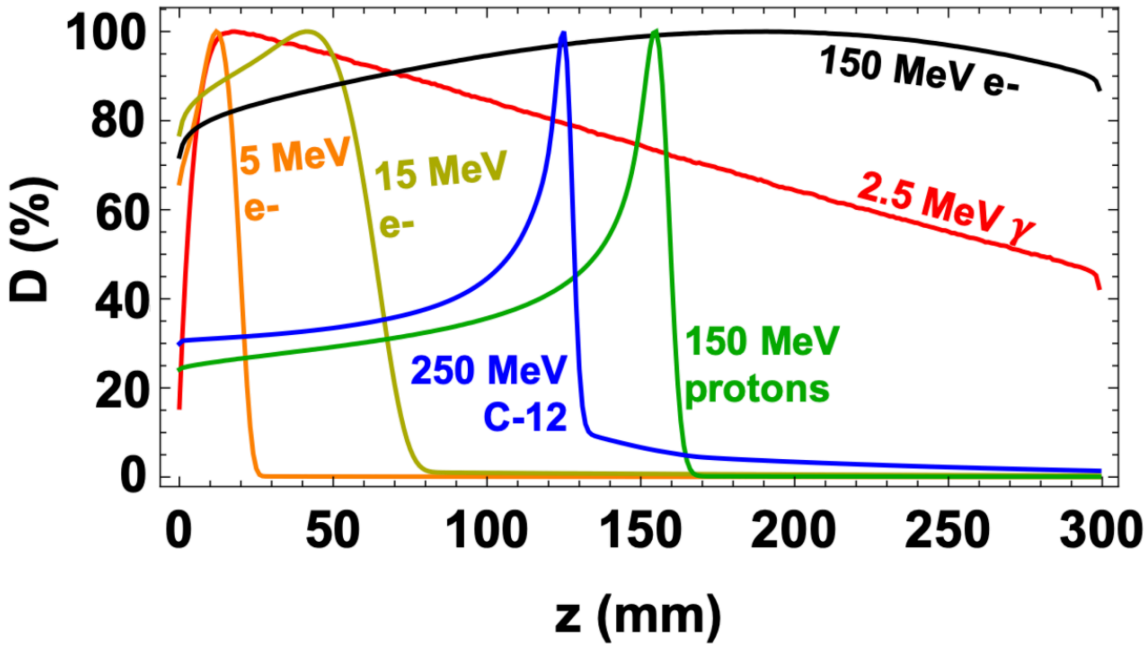

Figure 1.1: The dose-depth curve for a Gaussian distribution of an electron, photon, and ion beam in a water phantom, courtesy of [4].

different profile than both the electrons and photons. They penetrate a significant distance before depositing dose at a particular position (known as the Bragg peak). The electrons and photon deposit a significant amount of dose throughout their path. This gives the protons and ions an advantage in therapeutic settings. Dose can be isolated to a particular location while minimizing dose deposited on the way. Very few proton facilities exist, and so if laser technology advances enough to bring costs down, and protons or ions can be accelerated to high enough energies, it could be a viable path towards treatment.

1.1.2 Fast Ignition

The thought of using fusion based energy to power an electrical grid has been driving research in the field for decades. Vast literature has been published on steps towards better understanding and controlling fusion reactions. The first achievement of reaching a gain greater than unity was accomplished by the National Ignition Facility in 2022 [5]. Laser based fusion, or Inertial Confinement Fusion (ICF), is one route towards sustainable fusion energy sources. There are two main ways lasers are used to initiate a fusion reaction: indirect or direct drive (Fig. 1.2). Indirect drive involves a cryogenic deuterium-tritium (DT) fuel

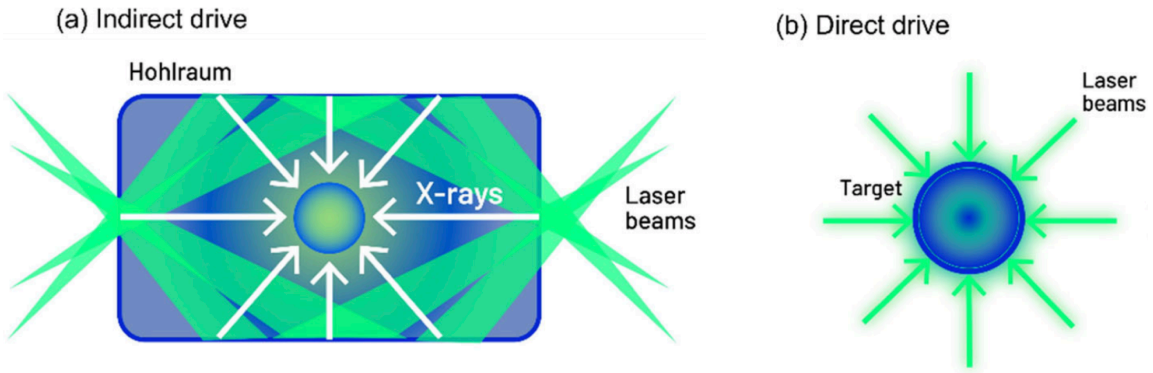

Figure 1.2: The a) indirect and b) direct drive scheme of ICF, courtesy of [6].

pellet suspended in a gold cylinder, known as a hohlraum. Lasers are then focused on the inside of the hohlraum, where x-rays are generated on the surface which are used to evenly compress the fuel. The other method, direct drive, simply focuses the lasers directly on the DT pellet to compress it. This technique for compression is referred to as the central hot spot method. The process is similar to a diesel engine, where pure compression ignites and starts the fusion burn reaction. An alternative method is to separate the compression from the heating. This technique is referred to as fast ignition [7]. The proposed method is to use lasers to compress the fuel (either in an indirect or direct fashion), and use a secondary source of energetic protons or ions [8, 9, 10, 11, 12, 13] to act as a spark and ignite the fuel once sufficient compression has been achieved. This is similar to a gasoline engine, which

partially compresses the fuel and then a spark plug ignites it. Fast ignition requires the fuel

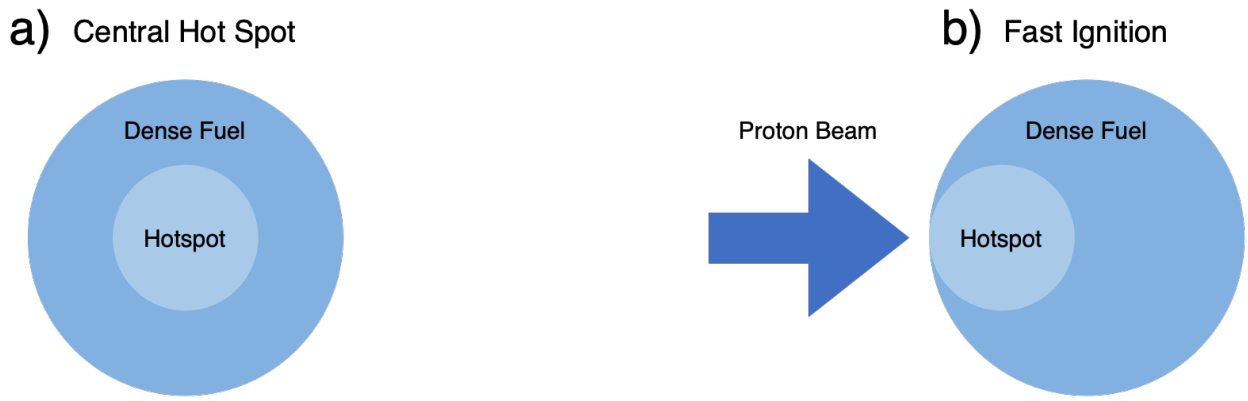

Figure 1.3: The a) central hotspot and b) fast ignition method, adapted from [6].

to be less symmetrically compressed, greatly reducing the effects that Rayleigh-Taylor-like instabilities have on the interaction. The fast ignition scheme also has a higher gain for a given laser energy. These advantages make fast ignition an attractive path towards fusion energy.

1.2 Motivation

Work has been done considering different foil shapes, materials, and patterns [14, 15, 16, 17, 18, 19, 20, 21] to enhance characteristics of an accelerated ion distribution such as collimation and peak ion energy. In this thesis, the ability to enhance ion acceleration through shaping the spatial and temporal distribution of a laser pulse, as opposed to shaping the foil, is explored. To do this, an accurate description of the propagation of arbitrary laser fields is needed. The spatial profile influences the laser-matter interaction and approximations must be avoided to ensure the fields used are correct. All the beam shapes considered are also achievable on current petawatt laser systems. Many techniques used for shaping the laser foil are only achievable in particle-in-cell simulations, and the practicality of the foil design, laser energy, and pulse duration parameters are out-of-reach and not yet experimentally viable.

1.3 Thesis Organization

This thesis describes simulation results modeling the propagation of different focused space-time structures and their effect on laser-foil interactions. It will be shown that the space-time couplings studied have impact on the energies and collimation of accelerated protons, and these values can be tuned through changing the spatial distribution of the laser pulse. Chapter 2 begins with a background on fundamental concepts relevant to the presented results. Chapter 3 describes code that was developed to model beam propagation and validates it against expected values from theory. This code is used for the results presented in the remaining chapters. Chapter 4 reveals the propagation effects of one particular space-time coupling generated from the focused output of a single-pass grating pair, where Chapter 5 presents the focusing properties of an axisymmetric extension of this type of beam. The characteristics of protons accelerated from a high-intensity laser pulse with the space-time couplings explored in the previous chapters are presented in Chapter 6. The thesis concludes with an outlook on high-intensity laser-foil interactions using lasers with space-time couplings.

Chapter 2

Background

2.1 Ultrafast Optics

2.1.1 Oscillators and Mode-locking

Mode-locked laser oscillators offer a robust method for generating ultrashort pulse trains, where the pulse duration may range from a few femtoseconds (fs) to picoseconds (ps) in duration. One of the most commonly used gain materials for mode-locked oscillators is Titanium Sapphire (Ti:Sapphire), which is able to achieve sub-5 fs pulse durations. Petawatt class Ti:Sapphire lasers operate around 30 J and 30 fs. Through careful design of a laser cavity, different longitudinal frequency modes lock in phase with each other (hence the term mode-locking). When multiple different frequencies align with each other, strong constructive interference occurs at one position with destructive interference elsewhere, generating a short pulse in the time domain. Keeping a fixed phase relationship between modes can be achieved with active or passive mode-locking methods. Active mode-locking requires the use of a device that modulates resonator losses to force the modes together. Passive mode-locking

modulates the loss through some inherent property of the system and doesn't require any active electronics. This can be achieved through a saturable absorber or through Kerr-lens mode-locking.

The Kerr effect is a nonlinear mechanism that uses the intensity-dependent index of refraction to create an effective saturable absorber. The refractive index is defined as:

$$n(I) = n_0 + n_2 I, \tag{2.1}$$

where n_0 is the linear refractive index, n_2 is the nonlinear refractive index, and I is the intensity of light. For Ti:Sapphire, $n_0 = 1.76$ and $n_2 = 3 \times 10^{-16}\ cm^2/W$. For a Gaussian pulse in space, which is a solution to the wave equation and a common stable profile in a laser cavity, the index of refraction is larger on-axis where the intensity is highest, and lower on the outside edge of the beam. This gradient in index creates a phase distribution of the form:

$$\phi = kn(I)z, \tag{2.2}$$

where k is the wavenumber of light, $n(I)$ is the refractive index defined in Eq. 2.1, and z is the length of the crystal. This phase distribution across the Gaussian beam profile is similar to a lens and focuses the laser. This can act as loss element in the cavity that modulates the amplitude and can force pulsed operation. Since the mode-locked operation requires all the frequencies to be in phase with each other, care must be taken to compensate for the dispersion the pulse experiences propagating through the cavity.

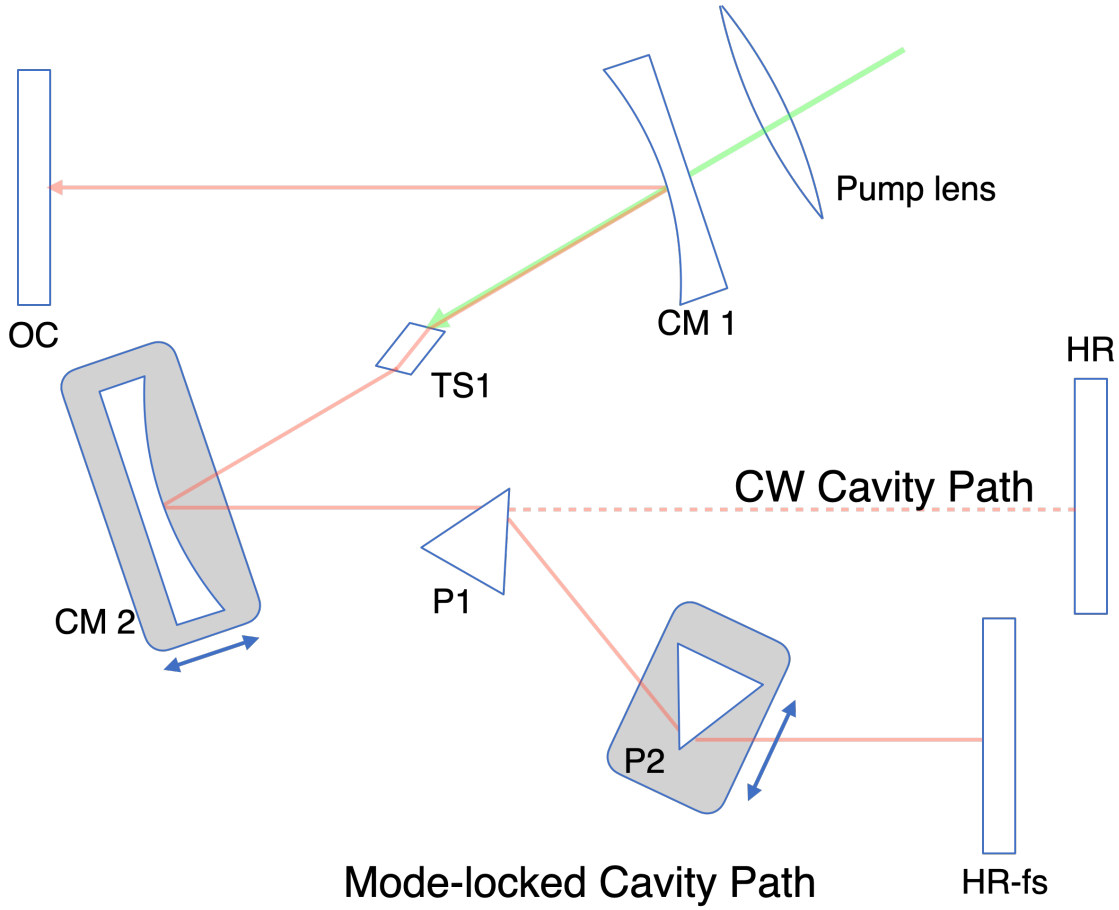

Figure 2.1: A schematic of a Ti:Sapphire laser in a z-cavity configuration. Without prisms, the cavity operates only in a continuous wave (CW) mode. With prisms inserted, the cavity can be CW or mode-locked. OC is the output coupler, CM refers to a curved mirror, P1 and P2 are prisms, HR is a high reflectivity mirror, HR-fs is a high reflectivity fs optimized mirror, and TS1 is the Ti:Sapphire crystal.

2.1.2 Dispersion

Dispersion is the phase delay experienced by different frequencies of light through taking different optical path lengths (OPL). Different frequencies can experience different OPLs based on a material property (index of refraction also depends on wavelength) or through propagating different geometric path lengths.

The wavelength dependent index of refraction is defined as:

$$n(\lambda) = \sqrt{1 + \sum_i \frac{B_i \lambda^2}{\lambda^2 - C_i}}, \tag{2.3}$$

and is known as the Sellmeier equation which relates the refractive index of a material, $n(\lambda)$, to the wavelength of light. The coefficients B_i and C_i are material dependent and are found experimentally. For example, the Sellmeier coefficients for fused silica, a common optical glass, are shown in Table. 2.1.

Coefficient	Value
B_1	0.6961663
B_2	0.4079426
B_3	0.8974794
C_1	0.0046791
C_2	0.0135121
C_3	97.9340025

Table 2.1: The Sellmeier coefficients for fused silica

The group delay dispersion (GDD) for a pulse traveling through a material of length L is defined as [22]:

$$\frac{d^2\phi}{d\omega^2} = \frac{4\pi^2 cL}{\omega^3} \frac{d^2 n(\lambda)}{d\lambda^2}. \tag{2.4}$$

where ω is the frequency of light, c is the speed of light, and $n(\lambda)$ is the refractive index defined in Eq. 2.3. The sign of the GDD is positive for common materials and near infrared wavelengths, which indicates that the red wavelengths travel faster in the material and lead in time.

A prism utilizes the wavelength dependence of the index of refraction in conjunction with Snell's Law to generate angular dispersion. Angular dispersion originates from different wavelengths of light traveling at different angles with respect to each other, forcing a different

traveled path length. The GDD for a prism pair is defined as:

$$\frac{d^2\phi}{d\omega^2} = \frac{4\pi^2 cL}{\omega^3}\frac{d^2P(\lambda)}{d\lambda^2}, \tag{2.5}$$

where $P(\lambda)$ is the optical path length each frequency travels inside each prism and in the space between prisms (a more thorough visualization and definition can be found in Ref. [23]).

The overall sign of the GDD for prism pair arranged at the angle of minimum deviation for common materials is negative. This indicates that a prism pair may be used to compensate for the positive dispersion of a material. Using a prism pair for dispersion compensation is common in short pulse oscillators, and is depicted in Fig. 2.1 within the mode-locked cavity path. A prism pair is used to compensate for the material dispersion of the crystal and mirrors.

Angular dispersion can also originate from the frequency-dependent diffraction from a grating (as opposed to the frequency-dependent refraction from a prism). The dispersion from a grating pair is discussed in detail in the following section.

2.1.3 Pulse Stretchers and Compressors

A pulse stretcher is a device that applies a temporal chirp on a short pulse that stretches the pulse in time and lowers the intensity. This is achieved by having different spectral components delayed relative to each other. Any sort of dispersive or diffractive component can cause a relative delay across a short pulse's frequency content. Most commonly, a prism pair or grating pair is used. There are many different types of stretchers, but one of the most commonly used is the Martinez stretcher [24], shown in Fig. 2.2. This stretcher works through having anti-parallel gratings placed a distance L apart, with a 2F telescope

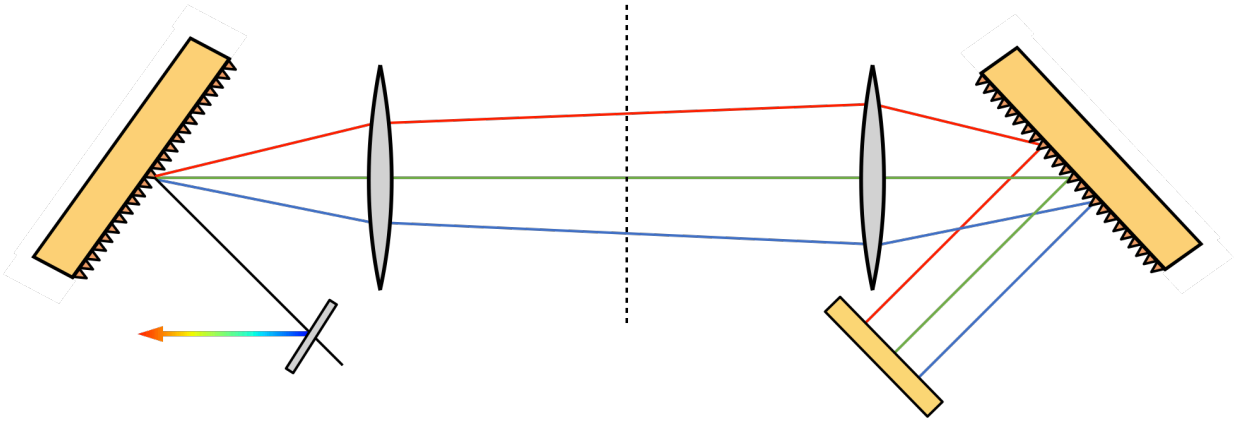

Figure 2.2: A schematic of a Martinez stretcher which introduces positive temporal chirp and GDD.

in between. By varying the distance between the second lens and second grating, the blue portion of the spectrum is forced to take a longer path than the red portion, causing the red portion to lead in time. The first grating imparts angular dispersion which gets magnified by the first lens and focused, causing the angular dispersion to get inverted and collimated by the second grating. The path length between the two imaging lenses does not vary, and so the length of the two focal lengths is subtracted from the total path length giving an effective path length:

$$L_{eff} = L - 2(f_1 + f_2) \tag{2.6}$$

with f_1 and f_2 being the focal length of the two lenses. The GDD of this is given by [22]:

$$\frac{d^2\phi}{d\omega^2} = -\frac{\lambda^3 L_{eff} M^2 d^2}{\pi c^2} \left[1 - (\lambda d - \sin\theta_i)^2\right]^{3/2}, \tag{2.7}$$

where λ is the wavelength, M is the magnification of the telescope, d is the groove density of the gratings, θ_i is the angle on incidence on the gratings, and c is the speed of light. The Martinez stretcher applies a positive temporal chirp, where the higher frequencies take a longer path than the lower frequencies, so that the low frequencies lead in time.

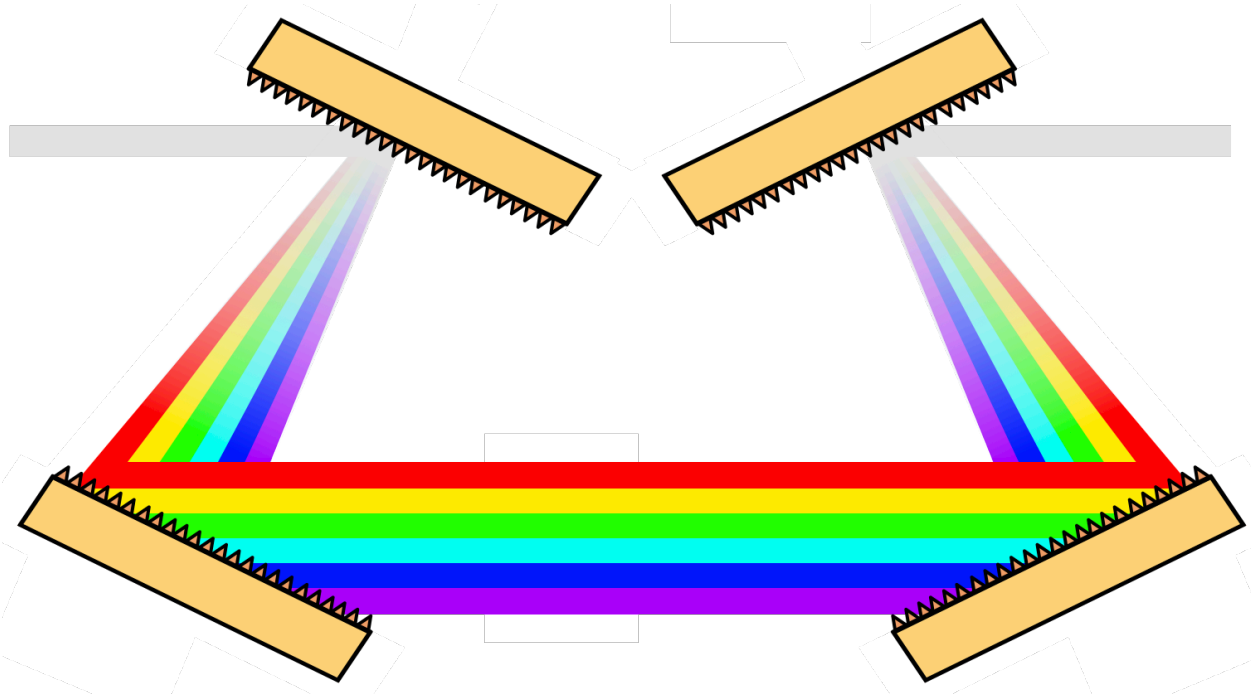

Figure 2.3: A 4-grating Treacy compressor. In this configuration, the red components of the spectrum take a longer path than the blue, resulting in a negative temporal chirp and GDD.

A compressor works by applying the opposite sign of temporal chirp on a pulse. Typically, this means a compressor applies a negative chirp to counter the positive chirp from the stretcher. The most widely used compressor is the Treacy compressor [25], consisting of either a double-passed grating pair, or a single pass, four grating arrangement (shown in Fig. 2.3). The GDD introduced by this configuration is [22]:

$$\frac{d^2\phi}{d\omega^2} = -\frac{\lambda^3 L_g d^2}{\pi c^2}\left[1-(\lambda d - \sin\theta_i)^2\right]^{3/2} \tag{2.8}$$

where L_g is the distance between gratings, normal to the grating surface. This equation has the same form as the Martinez stretcher but with opposite sign and $L_g = M^2 L_{eff}$, which means there is a configuration that will perfectly compensate the stretch introduced by a Martinez stretcher. In practice, PW lasers have an amplification setup after the stretcher which introduces other sources of dispersion from optics and bulk materials. Generally, GDD can be compensated, but there are residual higher order terms that remain after amplification

that necessarily increase the pulse duration and shape after compression.

2.1.4 Simultaneous Spatial and Temporal Focusing

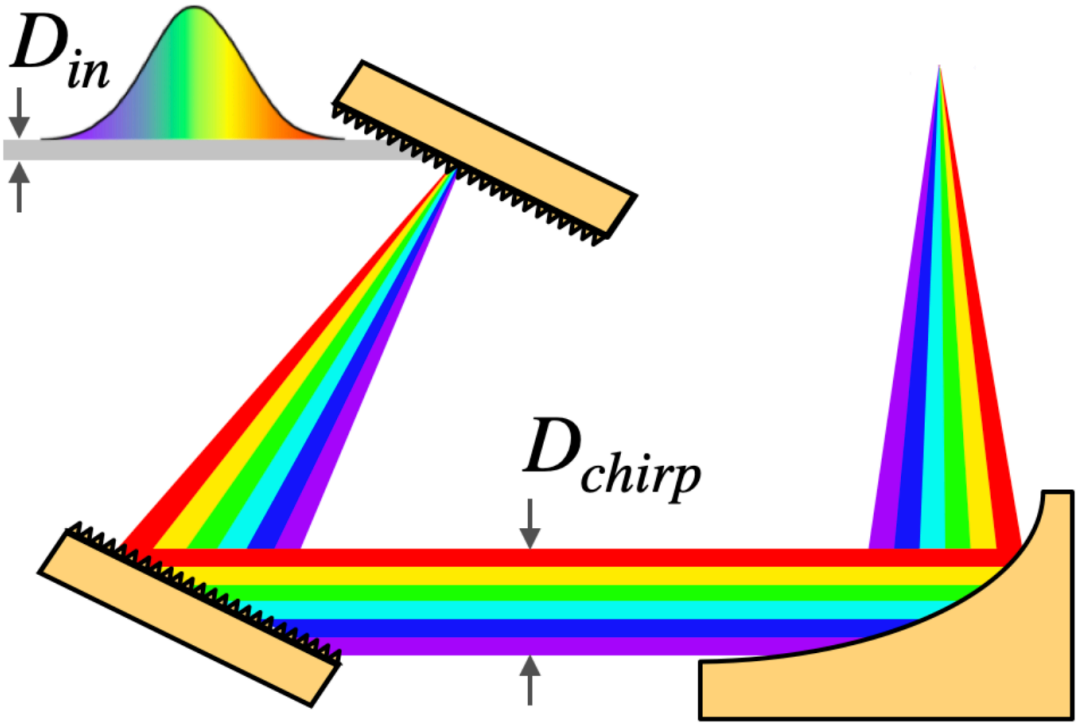

Figure 2.4: A two grating compressor oriented to create simultaneous spatial and temporal focusing of a pulse.

If the first two gratings from compressor from the CPA scheme are arranged in a single-pass two-grating arrangement, and the separation is doubled from the four-grating compressor, the resulting pulse after the the second grating will have no temporal dispersion, but will remain spatially chirped. The amount of spatial chirp is quantified by:

$$\beta_{BAR} = \frac{D_{chirp}}{D_{in}} \tag{2.9}$$

the ratio of the effective beam diameter of the chirped dimension to the diameter of the input beam to the compressor. If this field is focused, the individual frequency components gradually overlap and spatially focus. At the focal plane, the pulse reaches both its transform

limited pulse duration and the diffraction limited spot size. This technique is known as Simultaneous Spatial and Temporal Focusing (SSTF). The focused spatial chirp results in a pulse front tilt (PFT) at the focus.

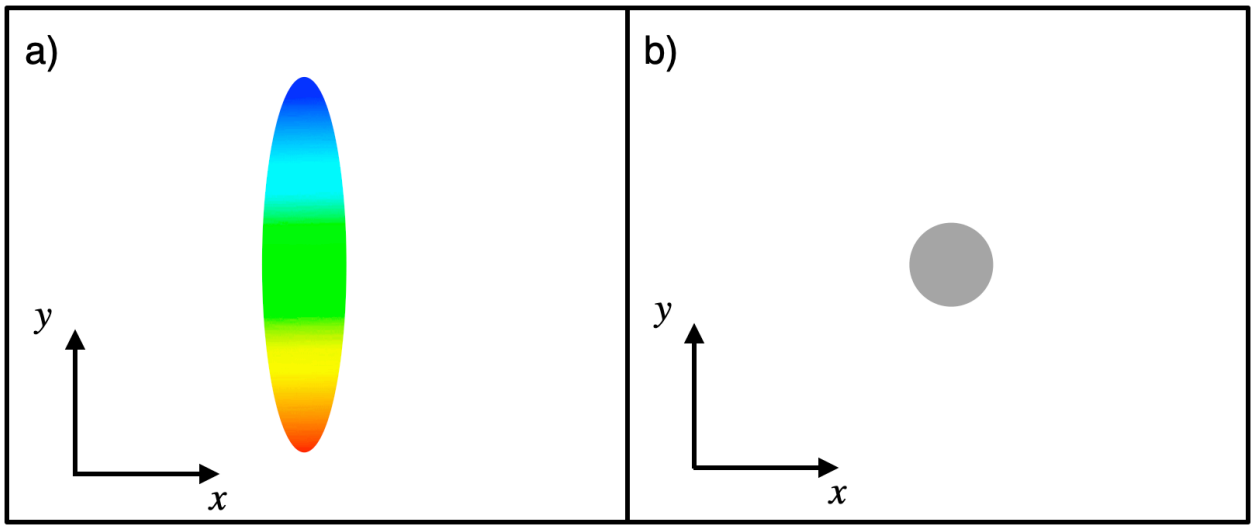

Figure 2.5: A representative schematic of the transverse components of a spatially chirped beam a) before focusing and b) at the focal plane. The color represents the frequency content, where the beam is spatially chirped in the y-dimension. Grey represents full overlap of all frequency content.

2.2 Fourier Propagation

Fourier optics is a technique for propagating fields of light, involving spatial Fourier transforms that treat light as a superposition of plane waves. The field of Fourier optics lends itself to computational techniques from being able to numerically solve analytic forms using Fast Fourier Transforms (FFT). The theory is derived for monochromatic light [26, 27], but in the case of short pulse lasers, each wavelength in the spectrum can be calculated and propagated separately and combined. It is useful to define the Fourier transform as

$$g(x,y) = \iint_{-\infty}^{\infty} G(f_x, f_y) \exp\left[j2\pi(f_x x + f_y y)\right] df_x df_y, \tag{2.10}$$

which can be written as

$$\mathcal{F}^{-1}\left[g(x,y)\right] = G(f_x, f_y), \tag{2.11}$$

where $G(f_x, f_y)$ is the Fourier transform result and f_x and f_y are the spatial frequencies corresponding to the x and y coordinates.

2.2.1 Rayleigh-Sommerfeld Propagation

The Rayleigh-Sommerfeld diffraction integral gives the most general solution to calculate the propagation of a field from one plane to another. The propagation scheme modeled is shown in Fig. 2.6, where the field U_1 is propagated a distance z away and evolves into field U_2. U_1 is defined with coordinate variables x_1 and y_1 at a particular z-position, z_1. Additionally, it is a function of frequency as well and will be written as $U_1(x_1, y_1, z_1, \omega)$. U_2 is defined on a grid with variables x_2 and y_2 at a particular z-position, z_2, and is also a function of frequency which will be written as $U_2(x_2, y_2, z_2, \omega)$. The variable, z, is set as $z = z_2 - z_1$. The Rayleigh-Sommerfeld diffraction integral is then defined as:

$$U_2(x_2, y_2, z_2, \omega) = \frac{1}{i\lambda} \int\int U_1(x_1, y_1, z_1, \omega) \frac{z e^{ikr}}{r^2} dx_1 dy_1, \tag{2.12}$$

with $r^2 = (x_2 - x_1)^2 + (y_2 - y_1)^2 + z^2$. This equation can be solved with numeric integration techniques, but requires significant computation time due to the double integral over the transverse dimensions, in addition to all the frequency components that are found in a short pulse. Conveniently, this integral can be defined as a convolution:

$$U_2(x_2, y_2, z_2, \omega) = U_1(x_1, y_1, z_1, \omega) * h(x_1, y_1, z_1, \omega), \tag{2.13}$$

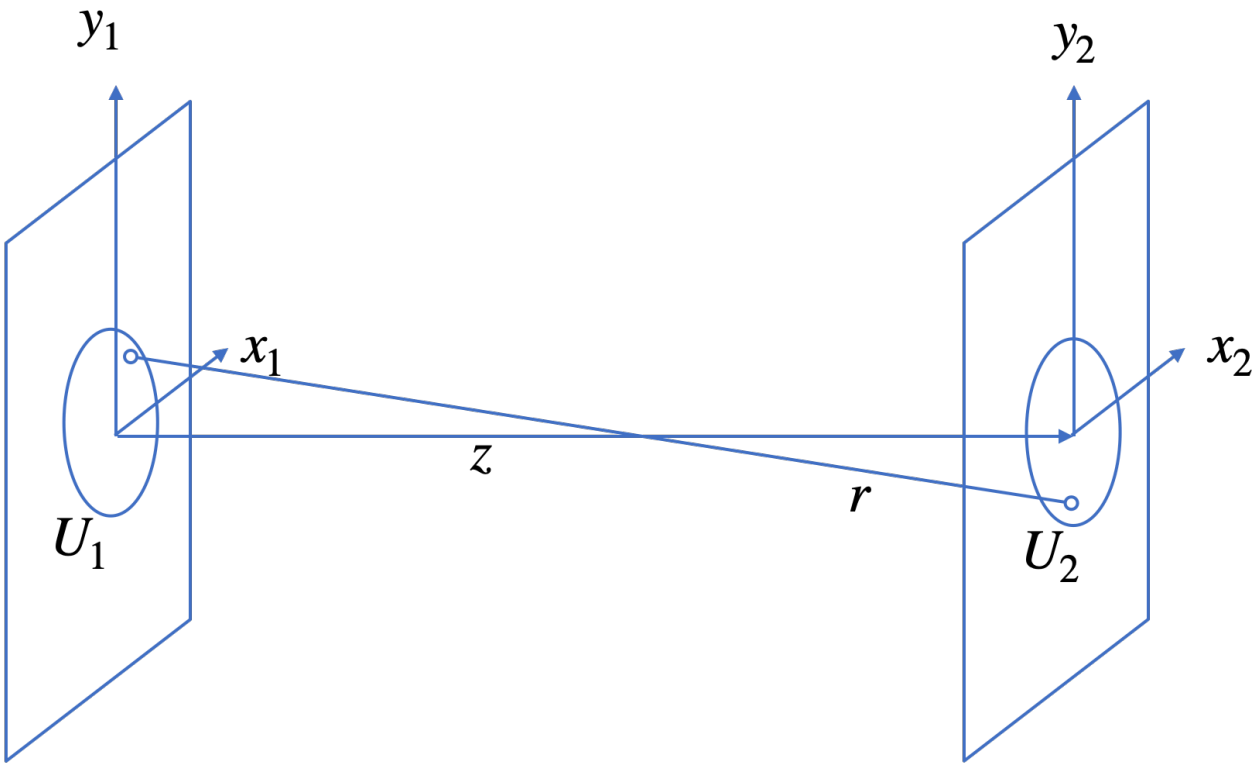

Figure 2.6: The Fourier propagation scheme of a source between two planes. Source U_1 is propagated to a plane z away and is defined as U_2

with $h(x_1, y_1, z_1) = -\frac{1}{2\pi}\frac{z}{r}\left(ik - \frac{1}{r}\right)\frac{e^{ikr}}{r}$ being the propagation kernel. Even more conveniently, this form can now be numerically solved using a Fourier transform using the property

$$U_2(x_2, y_2, z_2, \omega) = \mathcal{F}^{-1}\left[\mathcal{F}\left[U_1(x_1, y_1, z_1, \omega)\right]\mathcal{F}\left[h(x_1, y_1, z_1, \omega)\right]\right], \tag{2.14}$$

The Rayleigh-Sommerfeld propagation technique has no physical approximations and the only sources of error are numerical in nature. One drawback to the technique is that the two planes of propagation have to be the same dimensions and same sampling, which for fields that are being focused can result in large errors. For a small, focused spot (on the order of microns, for example) the step size of the numerical grid the field is defined on will typically be one order of magnitude less than the diameter to be properly sampled. Often, even better resolution is preferred for better resolved fields. For the input plane before focusing, the size of the beam can be quite large (especially for PW class beams on the order of 10 cm),

requiring the dimension of the numerical grid to be quite large, typically 3 times larger than the beam diameter for a Gaussian beam to be properly resolved when doing the FFTs. If a large aperture laser system with a $1/e^2$ beam diameter of 15 cm is focused down to a 5 μm spot, this would require a grid with dimensions 45 cm x 45 cm with a maximum step size of 0.5 μm. This results in a numerical grid defined by 2^{20} x 2^{20} points which is computationally difficult to compute in terms of memory (and this is not considering the extra dimension of the frequency/temporal information for the laser pulse!)

2.2.2 Fresnel Propagation

Two simple approximations can be made on the Rayleigh-Sommerfeld propagator that simplify the expression and calculation. First, it is assumed that z is large (which is true in a paraxial approximation) so that, in the denominator of equation 2.12, $r \approx z$. In the phase term of 2.12, k cannot be assumed small and so a Taylor expansion is done. First, r is rewritten as:

$$r = \sqrt{(x_2 - x_1)^2 + (y_2 - y_1)^2 + z^2} = z\sqrt{\frac{(x_2 - x_1)^2 + (y_2 - y_1)^2}{z^2} + 1}, \tag{2.15}$$

which can be simplified using the binomial expansion $\sqrt{1+b} \approx 1 + b/2$ for small b. This results in

$$r \approx z\left(1 + \frac{(x_2 - x_1)^2 + (y_2 - y_1)^2}{2z}\right). \tag{2.16}$$

Plugging these approximations back into Eq. 2.12 and rearranging terms we arrive at the Fresnel diffraction integral:

$$U_2(x_2, y_2, z_2, \omega) = \frac{e^{ikz}}{i\lambda z}\int\int U_1(x_1, y_1, z_1, \omega) e^{\frac{ik}{2z}\left[(x_2 - x_1)^2 + (y_2 - y_1)^2\right]} dx_1 dy_1 \tag{2.17}$$

This essentially is a parabolic approximation on the phase term in the exponential. This equation can also be written as a convolution and solved with Fourier transforms using Eq. 2.14 with $h(x_1, y_1, z_1) = \frac{e^{ikz}}{i\lambda z} \exp\left[\frac{ik}{2z}(x_1^2 + y_1^2)\right]$. The Fresnel propagation is also sometimes written in another form by expanding and grouping terms in the exponential:

$$U_2(x_2, y_2, z_2, \omega) = \frac{e^{ikz} e^{\frac{ik(x_2^2+y_2^2)}{2z}}}{i\lambda z} \int\int U_1(x_1, y_1, z_1, \omega) e^{\frac{ik}{2z}\left(x_1^2+y_1^2\right)} e^{\frac{-ik}{z}(x_1 x_2 + y_1 y_2)} dx_1 dy_1 \quad (2.18)$$

Then, using the definition of the Fourier transform from Eq. 2.14 and the property that:

$$f_{x_1} = \frac{x_2}{\lambda z},\ f_{y_1} = \frac{y_2}{\lambda z} \quad (2.19)$$

the final form can be expressed as:

$$U_2(x_2, y_2, z_2, \omega) = \frac{e^{ikz} e^{\frac{ik(x_2^2+y_2^2)}{2z}}}{i\lambda z} \mathcal{F}\left[U_1(x_1, y_1, z_1, \omega) e^{\frac{ik}{2z}\left(x_1^2+y_1^2\right)}\right]\left(\frac{x_2}{\lambda z}, \frac{y_2}{\lambda z}\right) \quad (2.20)$$

2.2.3 Fraunhofer Propagation

An additional approximation can be made on the Fresnel propagation, where it is assumed that the source dimensions are small where $x_1^2 + y_1^2$ are omitted from the phase term in Eq. 2.20, resulting in:

$$U_2(x_2, y_2, z_2, \omega) = \frac{e^{ikz} e^{\frac{ik(x_2^2+y_2^2)}{2z}}}{i\lambda z} \mathcal{F}\left[U_1(x_1, y_1, z_1, \omega)\right]\left(\frac{x_2}{\lambda z}, \frac{y_2}{\lambda z}\right) \quad (2.21)$$

This approximation is valid for large propagation distances, where x_2 and y_2 are much larger than x_1 and y_1. For this reason, the Fraunhofer approximation is valid for the far field only. This is a nice solution stating that the far field of a source, $U_1(x_1, y_1, z_1, \omega)$ is the Fourier transfrom multiplied by the phase factor $\frac{e^{ikz} e^{\frac{ik(x_2^2+y_2^2)}{2z}}}{i\lambda z}$.

2.2.4 Bluestein Method and the Chirped Z-Transform

The Bluestein method, also known as the chirped z-transform (CZT) [28, 29, 30] is a more general solution to the Discrete Fourier Transform (DFT) that is the common method used when numerically calculating Fourier transforms. The transform of interest is defined as:

$$X_k = \sum_{n=0}^{N-1} x_n z^{-nk} \qquad k = 0, \ldots, N-1, \tag{2.22}$$

with $z = \exp(i2\pi/N)$. For a typical DFT, the magnitude of z is confined to the unit circle such that $|z| = 1$. In the chirped z-transform, there is no such constraint on the magnitude, which enables the ability to arbitrarily sample the output plane after propagation. This difference is shown in Fig. 2.7. The Bluestein method breaks up the complex component

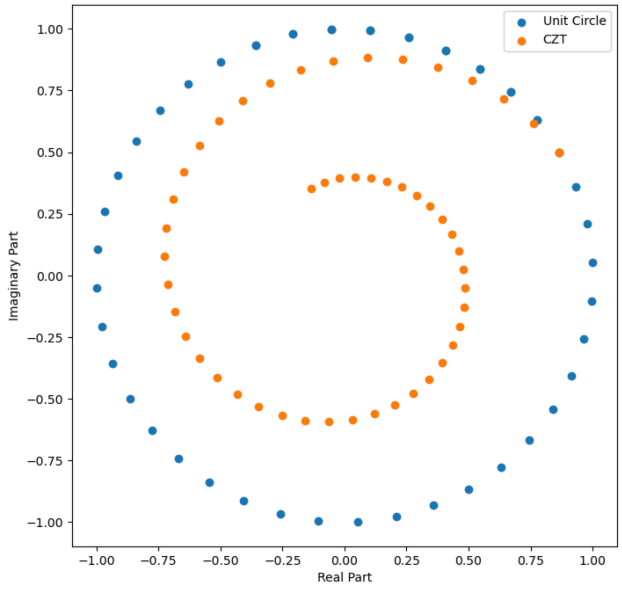

Figure 2.7: The chirped z-transform complex amplitude compared to the unit circle.

through writing X_k using the substitution:

$$nk = \frac{n^2 + k^2 - (k-n)^2}{2} \tag{2.23}$$

as:

$$X_k = z^{-\frac{1}{2}k^2} \sum_{n=0}^{N-1} x_n z^{-\frac{1}{2}n^2} z^{\frac{1}{2}(k-n)^2} = z^{-\frac{1}{2}k^2}(a_n * b_n) \tag{2.24}$$

which is a convolution between

$$\begin{aligned} a_n &= x_n z^{-\frac{1}{2}n^2} \qquad k = 0, \ldots, N-1 \\ b_n &= z^{\frac{1}{2}n^2} \qquad k = -N+1, \ldots, 0, \ldots, N-1, \end{aligned} \tag{2.25}$$

This convolution can be numerically calculated with Fourier transforms, enabling a computationally efficient implementation of the chirped z-transform.

2.2.5 Focusing

The beam may then be propagated or focused with a real lens of a particular radius of curvature, made of a certain material, defined by the Sellmeier equation or an ideal lens that can be hyperbolic, parabolic, or spherical.

The phase accumulation from a real lens of a certain material is given by [26]:

$$\phi_{lens}(x_1, y_1, \lambda) = k(n(\lambda)-1)\left[R_2\left(1-\sqrt{1-\frac{x_1^2+y_1^2}{R_2^2}}\right) - R_1\left(1-\sqrt{1-\frac{x_1^2+y_1^2}{R_1^2}}\right)\right], \tag{2.26}$$

R_1 and R_2 are the radius of curvature for the input and exit face of the lens, respectively.

The phase accumulation from ideal focusing (hyperbolic phase) is given by:

$$\phi_{lens}(x_1, y_1, \lambda) = -k\sqrt{f^2 + x^2 + y^2}, \tag{2.27}$$

The phase from a parabolic lens is given by:

$$\phi_{lens}(x_1, y_1, \lambda) = -\frac{k}{2f}\left(x^2 + y^2\right), \tag{2.28}$$

and the phase from a spherical lens is given by:

$$\phi_{lens}(x_1, y_1, \lambda) = k\sqrt{f^2 - x^2 - y^2}. \tag{2.29}$$

The phase profiles are plotted in Fig. 2.8 for an $F/1$ focusing optic.

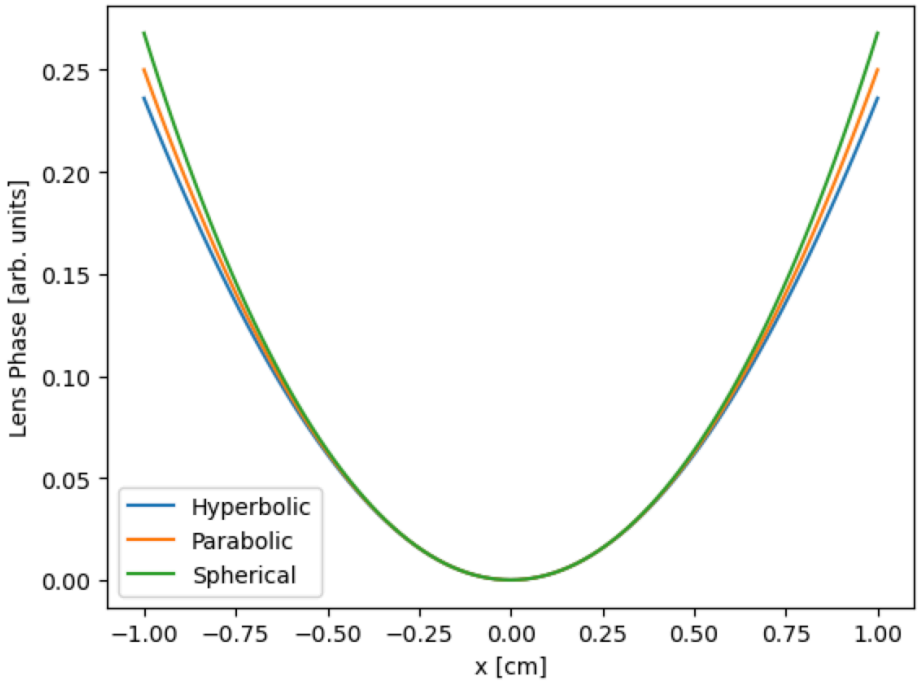

Figure 2.8: The phase profiles for an ideal hyperbolic, parabolic, and spherical lens

2.3 Particle in Cell Modeling using Smilei

The particle-in-cell (PIC) code Smilei [31] was used for simulating laser-plasma interactions. PIC codes are commonly used to describe the evolution of a plasma by approximating a plasma with a collection of macroparticles, where each macroparticle represents a certain

number of ions or electrons that has a larger charge and mass, but maintains the same charge to mass ratio. SMILEI is a kinetic PIC code, which uses a macroparticle's position, velocity, and current to model the evolution of the plasma by calculating and solving Maxwell's equations and the Lorentz force, satisfying Vlasov's equation. Mawell's equations and the Lorentz force are solved on a discrete numerical grid composed of spatial cells.

Each species in the plasma is described by a distribution function, $f_s(t, x, p)$. Each species consists of particles that have a certain charge (q_s), mass (m_s), position (x), and momentum (p). The distribution function is defined as:

$$f_s(t, x, p) = \sum_{p=1}^{N} w_p \; S(x - x_p(t)) \; \delta(p - p_p(t)), \tag{2.30}$$

where δ is the Dirac distribution, S is the shape function which describes a macroparticle, w_p is the macroparticle weight, V_c is the volume of a single cell, N_s is the number of macroparticles, and the subscript p denotes a particular macroparticle. Solving the Vlasov equation with this distribution function results in two equations of motion to describe the motion of marcroparticles:

$$\frac{dp_p}{dt} = q_s \left(E_p + \frac{p_p}{\gamma_p m_s} \times B_p \right) \tag{2.31}$$

$$\frac{dx_p}{dt} = \frac{p_p}{\gamma_p m_s} \tag{2.32}$$

where $\gamma_p = \sqrt{1 + \left(\frac{p_p}{m_s}\right)^2}$

Maxwell's equations are solved using the Finite Difference Time Domain method [32]. The fields are solved on the Yee grid [33], which staggers the electric field and magnetic fields in time. The electric fields are defined on integer times steps, and the magnetic fields on

half-integer steps.

The PIC simulation starts by loading the initial conditions of the plasma, including the density, temperature, and shape. The initial electric field is computed using Poisson's equation. After this, the PIC loop commences. The PIC loop is an algorithm used to calculate the fields on the grid and advance the particles. The steps of the PIC loop are shown in Fig. 2.9. It starts with pushing the particles using the kinetic equations of motion. The weights of the particles are then deposited onto the grid. If the particles don't fall directly on a node, the position is interpolated onto the grid points. Maxwell's equations are then used to solve the electric and magnetic fields. These fields are then applied again to the particles. Once this is done, the particles are pushed and the loop cycles until the simulation is ended. The simulation domain in SMILEI is defined such that the x-dimension is the longitudinal direction and axis of laser propagation, and the y-dimension and z-dimension are transverse coordinates.

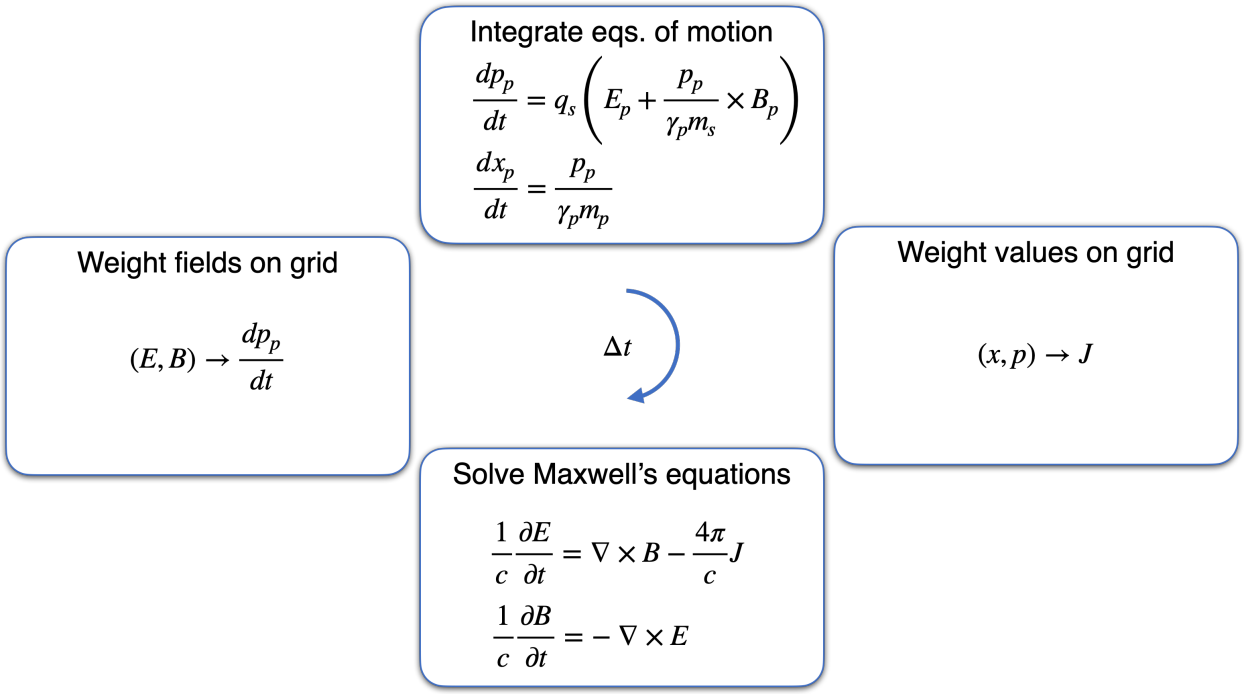

Figure 2.9: A representative model of the PIC loop, showing the algorithm used to model the evolution of a plasma.

2.4 Basics of Laser-Plasma Interactions

The laser-plasma interactions considered involve sufficiently high intensity pulsed lasers interacting with a high density foil, modeled as a plasma. The intensity of the laser field can be described by the normalized vector potential:

$$a_0 = \frac{eE}{m_e \omega_L c}, \tag{2.33}$$

where e is the charge of an electron, m_e is the mass of an electron, E is the amplitude of the electric field of the laser, ω_L is the central frequency of the laser, and c is the speed of light. a_0 is related to the intensity through:

$$a_0 = \sqrt{\frac{I\lambda_0^2}{1.37 \times 10^{18}}}, \tag{2.34}$$

where I is the intensity of the laser in $[W/cm^2]$, and λ_0 is the center wavelength of the laser in units $[\mu m]$. A plasma consists of a species of ions and neutralizing electrons. Typically, the ultrahigh intensity lasers have a pedestal on the pulse structure, whose peak intensity can be several orders of magnitude less intense than the main pulse. The pedestal that leads ahead of the pulse interacts with the solid density foil first. If the main peak is assumed to be 10^{18} W/cm^2, a pedestal with an intensity 10^5 orders of magnitude less will start to ionize the foil, stripping electrons of the surface before the main pulse arrives. This forms a preplasma of electrons on the front side of the foil that the main pulse interacts with. This preplasma expands and is usually modeled with an exponential profile [34] given by:

$$n_e = n_0 \exp(-x/l), \tag{2.35}$$

where n_e is the electron density of the plasma, n_0 is the original, unperturbed electron density of the solid foil, x is the longitudinal coordinate before the foil, and l is the characteristic

length of the preplasma. l is determined based on the shape of the pre-pulse.

Once the laser interacts with the plasma, it will displace electrons whose motion will be described by the Lorentz force:

$$F = -e(E + \frac{v}{c} \times B), \tag{2.36}$$

If we consider a field that has a spatial profile, such as a focused Gaussian beam, an electron interacting with the field will move from a region of high intensity towards a region of lower intensity based on the ponderomotive force:

$$F_p = -\frac{e^2}{4m_e\omega_0^2}\nabla E^2 \tag{2.37}$$

where the electron feels a force that is proportional to the gradient of the electric field.

A displaced electron is subsequently restored due to a charge separation in the plasma and will oscillate at a frequency known as the plasma frequency:

$$\omega_p = \sqrt{\frac{n_e e^2}{\gamma_L m_e \epsilon_0}}, \tag{2.38}$$

with ϵ_0 being the permittivity of free space and $\gamma_L = \sqrt{1 + a_0^2/2}$, which takes into account a corrective factor for strong, relativistic fields ($a_0 > 1$).

The Debye length is the distance of one plasma period ($1/\omega_p$) and is defined as:

$$\lambda_D = \sqrt{\frac{\epsilon_0 k_b T_e}{n_e e^2}}, \tag{2.39}$$

where k_b is the Boltzman constant and T_e is the thermal temperature of the electron. The Debye length is an important parameter which describes the distance over which a charged

particle feels the charge of surrounding particles. Another parameter commonly used in laser-plasma interactions is the critical density of the plasma:

$$n_c = \frac{\gamma_L m_e \epsilon_0 \omega_L}{e^2}. \tag{2.40}$$

The critical density is the point where $\omega_L = \omega_p$. If the plasma density is above this value, incident laser light is reflected. If the density is lower, laser light will penetrate the plasma. For 1 μm light, the critical density is $1.1 \times 10^{21}\ cm^{-3}$. Solid density is on the order of $100 n_c$. In a plasma that is above the critical density, an evanescent component of the incoming wave will penetrate into the plasma a distance known as the skin depth:

$$l_s = c/\omega_p. \tag{2.41}$$

When conducting numerical simulations, it is usually a good idea to resolve the Debye length and skin depth to properly model the laser-plasma interaction and avoid any numerical errors or artifacts. In practice, this can be quite difficult, especially in 3-dimensional simulations, due to the computational resources needed to resolve distances that are typically small.

2.5 Mechanisms of Ion Acceleration

There are many ion acceleration mechanisms including Target Normal Sheath Acceleration [35] (TNSA), Coulomb Explosion [36], Radiation Pressure Acceleration [37], Hole-Boring Acceleration [38], Light-Sail Acceleration [39, 40], and Break-out Afterburner [41]. Target Normal Sheath Acceleration is one of the most commonly studied and observed ion acceleration mechanisms. This is mainly in part that the TNSA mechanism occurs at intensities as low as $10^{18}\ W/cm^2$ for 800 nm to 1000 nm lasers, and so is present in many laser-foil interactions at early times. A schematic of the acceleration is depicted in Fig. 2.10. An

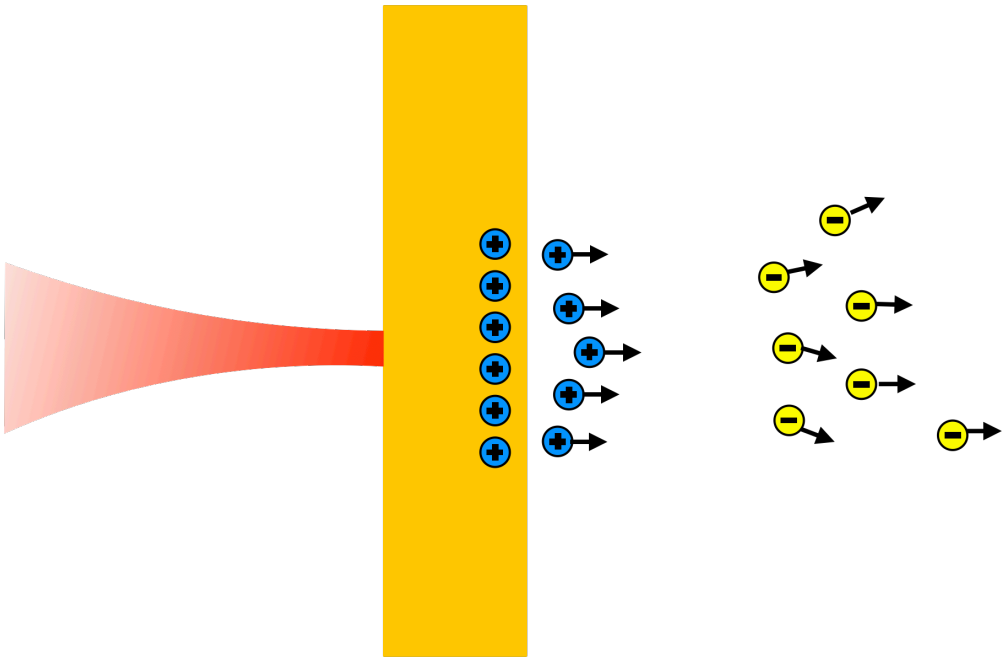

Figure 2.10: A schematic of the Target Normal Sheath Acceleration mechanism.

intense laser irradiates the front surface of a foil, forming a plasma. The pulse accelerates electrons in the forward direction which propagate through the target. They will scatter within the material, and the electrons with sufficient energy will manage to escape through the other side. This generates a sheath on the back surface, which generates a strong electric field due to the charge separation. This charge separation will accelerate the lightest ions present in the material (protons) followed by heavier ions.

A laser with sufficiently high intensity can penetrate a solid density target. At high a_0 values, the corrective γ_L term becomes large. This results in the plasma frequency in Eq. 2.38 decreasing, which increases the skin depth. Additionally, the critical density in Eq. 2.40 increases. The combination of these effects enable the laser to partially transmit through the foil in a process known as Relativistic Induced Transparency [42, 43] (RIT), heating electrons deeper into the foil. This changes the interaction dynamics and acceleration of electrons and protons though a stronger longitudinal field.

Chapter 3

Fourier Propagation Code

3.1 Introduction

An open-source, vectorized Fourier propagation code was developed in Python3 to enable the exploration of arbitrary laser pulses propagating in vacuum, and later interfaced with the particle-in-cell code, Smilei. The code takes in a user-defined field, that can either be defined as an analytic functional form, or passed as an array of measured data. The coordinate system of the code defines x and y as transverse coordinates and z as the axis of propagation.

For example, a Gaussian beam may be defined with the form:

$$E(x,y) = \exp\left(-\frac{(x-x_0)^2 + (y-y_0)^2}{w_{\text{in}}^2}\right), \tag{3.1}$$

where w_{in} is the $1/e^2$ beam radius of the intensity, x and y are spatial coordinates, and x_0 and y_0 are the center coordinates of the Gaussian distribution. The spectrum can also be

defined analytically, and a Gaussian spectrum in frequency can be defined as:

$$E(\omega) = \exp\left[-\frac{(\omega-\omega_0)^2}{\Delta\omega^2}\right], \tag{3.2}$$

where ω is the frequency coordinate, ω_0 is the central carrier frequency, and $\Delta\omega$ is the $1/e^2$ half-width of the spectral intensity. Multiplying these two distributions together gives the full field to be used in the code. This field is shown in Fig. 3.1, modeled as a Gaussian laser with a center wavelength, $\lambda_0 = 800\ nm$, $w_{in} = 0.5\ mm$, $\Delta\omega = 0.25\ Prad/s$, which translates to a FWHM pulse duration $\Delta t = 9.42\ fs$. The transverse field is depicted in Fig. 3.1a, the spatial-frequency representation in Fig. 3.1b, and the spatio-temporal field in Fig. 3.1c.

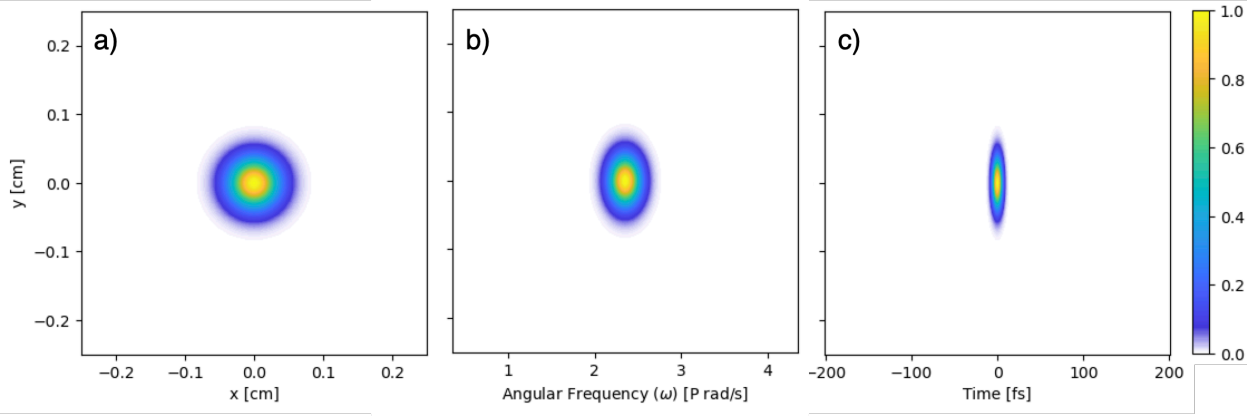

Figure 3.1: An example Gaussian pulse passed as input to the Fourier propagation code. The a) transverse distribution of the field, b) spatio-spectral distribution, and c) spatio-temporal distribution are shown.

The field is then propagated using the Rayleigh-Sommerfeld propagator for its accuracy, along with the Bluestein chirped-z transform for the ability to scale the input plane and propagation plane. The field can be visualized in the space-frequency, or space-time domain at any z-position along its propagation. The example Gaussian is focused with an ideal lens of focal length, $f = 10\ cm$ and shown in Fig. 3.2. With post-processing, the field can be visualized in a purely spatial representation, but the natural output from the Fourier propagation technique is inherently in the frequency domain (or temporal with a Fourier transform) at a given z-position. The code can also handle measured data, such as a beam

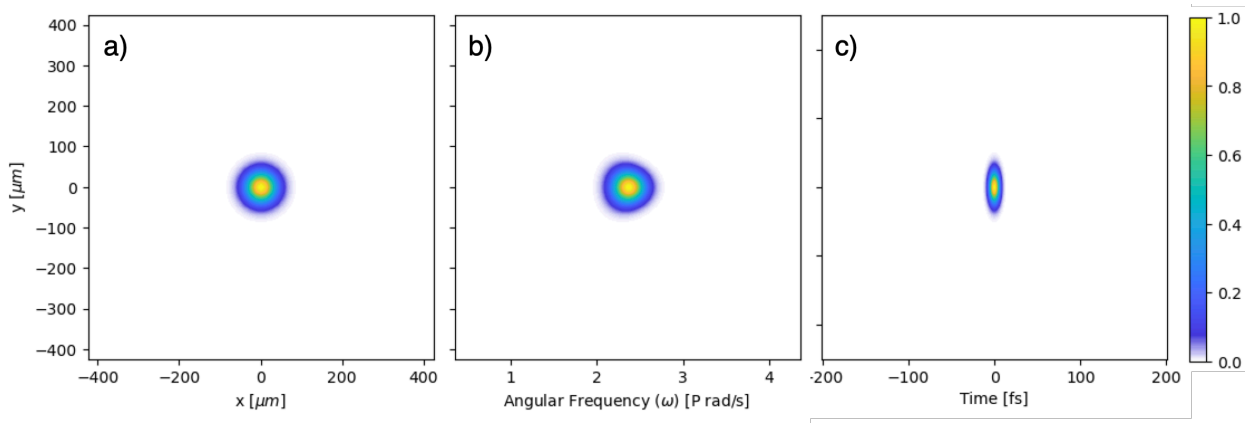

Figure 3.2: An example of a focused Gaussian pulse with an ideal lens of focal length $f = 10\ cm$. The a) transverse distribution of the field, b) spatio-spectral distribution, and c) spatio-temporal distribution are shown.

profile and spectrum.

3.2 Code Validation

The output of the Fourier propagation code is compared to theory to show its accuracy in calculating the correct fields during propagation. The theoretical Gaussian propagation expression is [44]:

$$E(x,y,z) = exp\left(-\frac{x^2+y^2}{w^2(z)} + i\varphi(z) - i\frac{\omega_0(x^2+y^2)}{2cR(z)}\right), \tag{3.3}$$

with $w(z) = w_0\sqrt{1+\left(\frac{z}{z_R}\right)^2}$ being the $1/e^2$ beam radius as a function of distance, $R(z) = z+\frac{z_R^2}{z}$ the radius of curvature, $\varphi = \tan^{-1}\left(\frac{z}{z_R}\right)$ the Gouy phase, and w_0 the $1/e^2$ beam radius at the focus. z_R is the Rayleigh length of the center wavelength, $z_R = \frac{\pi w_0^2}{\lambda_0}$. The expression used for the temporal envelope is:

$$E(t) = exp\left(-i\omega_0 t\right) exp\left(-4\ln 2\left(\frac{t}{\Delta t}\right)^2\right) \tag{3.4}$$

A 1 μm, 25 fs pulse is focused down to a 4 μm spot using the Fourier propagation code and compared to the theoretical propagation of Eq. 3.3, using two spatial dimensions and a temporal dimension. Equations 3.3 and 3.4 assume a monochromatic propagation, and so for a proper comparison, approximations are forced in the Fourier code, where all k, ω, and λ values are set to the carrier frequency value (k_0, ω_0, λ_0, respectively). Upon doing this, the analytic and Fourier propagated fields are compared at $z = f - z_R$, $z = f$, and $z = f + z_R$ in Fig. 3.3, where $z_R = 50.26$ μm. The spatial resolution for this comparison

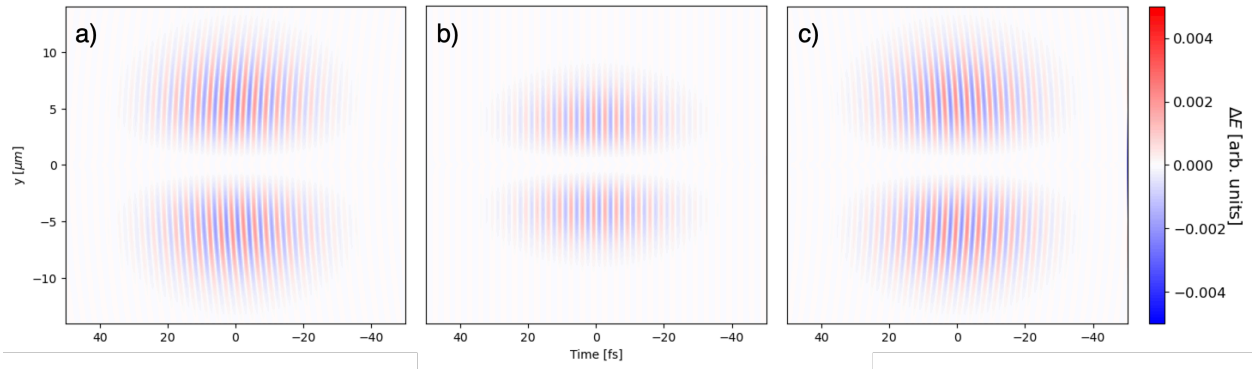

Figure 3.3: The absolute difference in fields between the analytic formalism and the Fourier propagated Gaussian pulses. The two field amplitudes are normalized to $|E| = 1$. The difference in fields are calculated at z-positions a) one Rayleigh range before the focus, b) at the focus, and c) one Rayleigh range after the focus.

was 0.117 μm, and the temporal resolution was 0.146 fs. Within the confocal parameter, there is at maximum an absolute difference between the two fields of 0.0035. This error is improved if the spatial and temporal resolution of the simulations is increased. The on-axis longitudinal intensity, $I(z, x = 0, y = 0)$ can also be compared between the two propagation methods. The on-axis intensity profile follows the form [44]:

$$I(x = 0, y = 0, z) = \frac{1}{1 + \left(\frac{z}{z_R}\right)^2} \tag{3.5}$$

The propagated field is compared to theory in Fig. 3.4 where the two intensity profiles match. Additionally, the Fourier propagated field properly accounts for the diffractive effect of focusing light and results in a focal spot shift of $\Delta f \approx z_R^2/f$ [44]. For the case simulated,

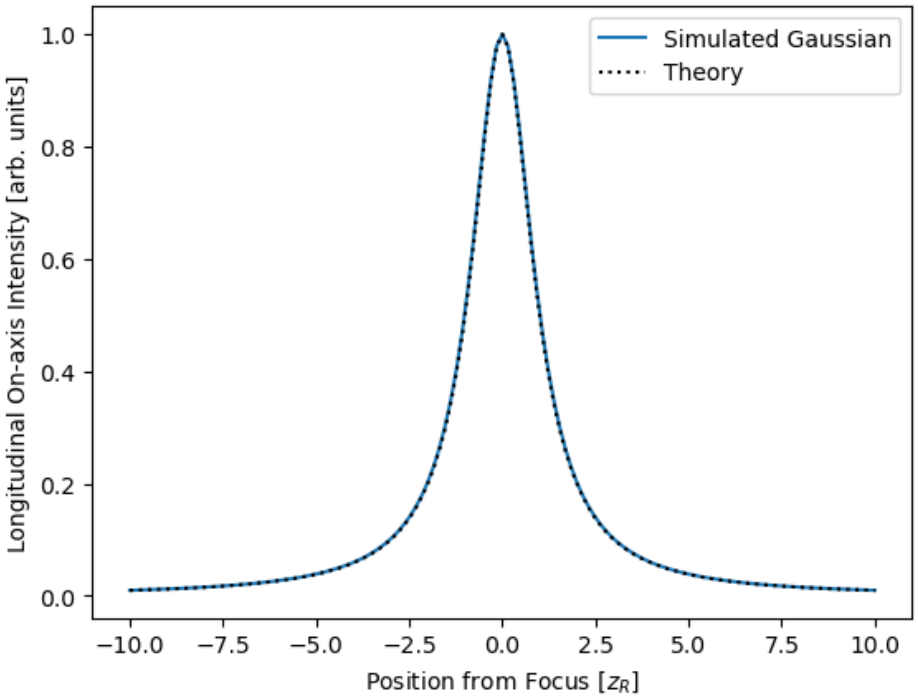

Figure 3.4: The on-axis intensity of a propagated field is compared to the expected value from Eq. 3.5

the focal shift results in a value of $\approx 26\ nm$, which is negligible on the scale shown and not visible.

3.3 Conclusion

The Fourier code is validated against the known theoretical propagation of a Gaussian beam. The model accurately describes the field as it propagates, capturing the full diffractive effects including the diffraction limited spot size, curved phase fronts, and field amplitude.

Chapter 4

1-Dimensional Spatially Chirped Beams

4.1 Introduction

The use and focusing of chirped beams was first proposed in 2004 as a route to produce ultra-high peak power laser pulses in a technique known as chirped beam amplification [45]. This concept, which is the spatial analog to chirped pulse amplification [2] (CPA), involves dispersing the spectral content of a pulse in a transverse spatial dimension to reduce its local intensity and thus avoid damage in amplifiers and final optics [46, 47]. Focusing a chirped beam simultaneously reduces the spatial and temporal extent of the pulse in a technique that is commonly referred to as simultaneous spatial and temporal focusing (SSTF) [48, 49]. The most frequently employed approach to SSTF is through the one-dimensional spatial chirp of a Gaussian beam profile generated with a grating pair with an appropriately pre-chirped pulse. As an ultrashort pulse travels through the grating pair, its spectral components are spatially separated in one dimension, necessarily reducing the

pulse's local spectral content and increasing the pulse's local pulse duration. As the beam focuses, the spectral components gradually spatially overlap until the pulse reaches both its minimum spatial width and its transform limited pulse duration at the focus. This leads to a pulse front tilt (PFT) whose orientation is a function of the magnitude of beam chirp and the f-number of the focusing system. SSTF has been used in multiphoton microscopy [50, 51, 52], micromachining, [53, 54, 55] and structured 3D printing [56].

Recently, focal spots with PFT have been studied in high intensity laser plasma experiments for electron acceleration where tuning the angle of the PFT enables electron steering [57, 58] and target normal sheath acceleration (TNSA) schemes for improved maximum electron energies in TNSA target interactions [59]. Next-generation high-intensity lasers are potentially reaching the ultra-broadband spectral regime, with temporal pulse widths near 10 fs [60, 61, 62], where the study of space-time couplings, such as PFT, are relevant [63]. These lasers could be used for advanced acceleration schemes based on chirped beams and SSTF interactions for studying novel laser-matter interactions, including traveling wave excitation for soft x-ray amplification [64, 65]. Additionally, SSTF systems can be used as part of a post-amplification pulse compression scheme [66].

Generating a high-peak-intensity PFT focal spot with the SSTF technique requires the use of a grating pair to spatially chirp the beam. Gratings impart a nonlinear spatial chirp across the bandwidth of the pulse, especially at near-infrared frequencies. In this work, we argue that for large-bandwidth pulses this grating-induced nonlinearity needs to be considered, as the linear approximation typically used in studying spatial chirp becomes significantly inaccurate. Careful choice of the gratings used to generate the spatial chirp is important because groove density and angle of incidence (AOI) affect the degree of nonlinearity, which in turn changes the space-time structure as the pulse propagates through the focus. The nonlinearity also imparts a pulse front curvature (PFC) and varies the intensity localization, necessarily changing the fundamental interaction of the focusing laser pulse with matter. The

characteristics of a chirped beam from spatial chirp configurations generated using different grating pairs are simulated and described.

4.2 Methods

4.2.1 System Design

A typical SSTF system consists of a grating pair that spreads the frequency components of a laser pulse in 1D, shown in Fig. 2.4. To have a transform limited pulse at the focus, a positive temporal pre-chirp must be imparted on the pulse to compensate for the temporal group delay dispersion from the grating pair. This is readily achieved, as the two gratings in Fig. 2.4 act as half of a Treacy compressor [25], whose induced temporal chirp on the incident laser pulse can be perfectly compensated with an upstream Martinez stretcher [24, 67]. To have temporal compensation with only half of a compressor, the separation between the gratings must be doubled from the values defined for a 4-grating or double-pass 2-grating arrangement. The amount of chirp in this system can be defined by the beam aspect ratio (Eq. 2.9) which can be tuned by varying the grating separation and changing the temporal pre-compensation.

4.2.2 Simulation Model

An open source linear Fourier optics code in Python3 was developed to simulate a user-defined electric field propagating through a lens and free space. The electric field can be visualized at any position throughout the focal volume to observe the effects different system parameters have on the pulse profile at and near the focus. Any spatial profile and spectrum can be modeled and propagated. A Gaussian beam in space and frequency is modeled for

its simplicity and ease of interpolating results. An initial electric field that is Gaussian in space and spectrum is defined before the focusing optic using Eqs. 3.1 and 3.2 to get:

$$E(x_1, y_1, z = 0, \omega) = E_0 E(\omega) E(x_1, y_1) = E_0 \exp\left[-\frac{(\omega - \omega_0)^2}{\Delta\omega^2}\right] \exp\left(-\frac{x_1^2 + y_1^2}{w_{\text{in}}^2}\right), \quad (4.1)$$

where $\Delta\omega$ is the $1/e^2$ half-width bandwidth of the spectrum, ω_0 is the center frequency, and $w_{\text{in}} = D_{\text{in}}/2$ is the $1/e^2$ beam radius of the field intensity. The simulations presented here are based on a typical Ti:Sapphire laser system with a center wavelength of 800 nm, a beam radius of 0.5 mm, a focal spot size radius of 50.5 μm, and a full width at half max bandwidth of 100 nm, resulting in a transform-limited pulse width of $\sim$ 9.4 fs. In the simulations, the initial electric field is defined on a square numeric grid with spatial lengths $L_{1,x} \times L_{1,y}$ and spacing Δx_1 and Δy_1, whose values depend on the initial conditions of the model, such as beam diameter, chirped beam diameter, and focal length.

The initial spatial electric field used to describe a linearly polarized beam with 1D linear

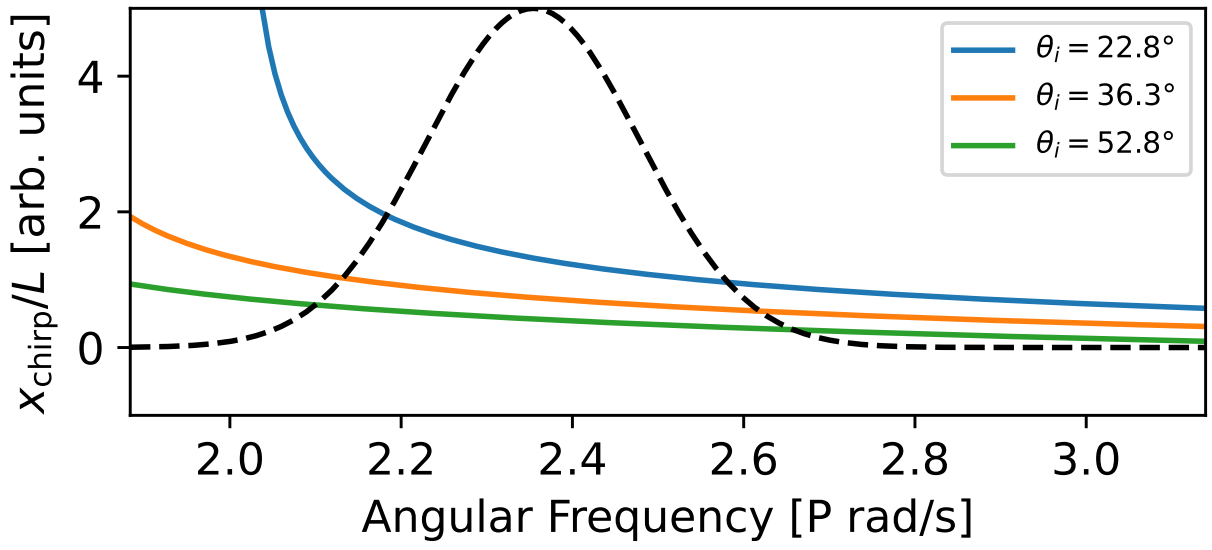

Figure 4.1: Normalized spatial chirp as a function of frequency is shown for three cases of AOI, θ_i, for a 1480 lines/mm grating pair used in a Ti:Sapphire CPA system [68, 69, 70, 71, 72]. The spectrum of the 9.4 fs, 800 nm Ti:Sapphire laser used in this paper is shown as a dashed line.

spatial chirp in the x-direction is typically expressed as [49, 51, 73, 74, 75]:

$$E(x_1, y_1) = \exp\left\{-\frac{[x_1 \pm \alpha(\omega - \omega_0)]^2 + y_1^2}{w_{\text{in}}^2}\right\}, \tag{4.2}$$

The chirp rate, α, which is the amount that each frequency component is separated from the previous, is assumed constant, resulting in a linear separation between frequency components. This approximation is valid only for pulses with small bandwidths based on a Taylor expansion analysis [74].

In practice, the spatial chirp from a grating pair is nonlinear in frequency and is derived from the grating equation, where the spatial dependence on frequency is:

$$x_{\text{chirp}}(\omega) = L\ \tan\left[\sin^{-1}\left(\frac{-2\pi mcd}{\omega} - \sin\theta_i\right)\right], \tag{4.3}$$

and the new chirp rate becomes:

$$\alpha(\omega) = \frac{dx_{\text{chirp}}(\omega)}{d\omega}, \tag{4.4}$$

where L is the separation between the gratings (normal to the grating surface), d is the groove density, m is the diffraction order, c is the speed of light, and θ_{AOI} is the angle of incidence on the grating.

Seen in Fig. 4.1, the spatial chirp generated by a grating pair is increasingly nonlinear for lower frequencies, so the linear chirp approximation breaks down and the full calculation must be considered. As smaller angles of incidence are used, the nonlinearity increases. This kind of chirp is referred to as nonlinear chirp. The definition of the electric field now has the form:

$$E(x_1, y_1, \omega) = \exp\left(-\frac{[x_1 - x_{\text{chirp}}(\omega)]^2 + y_1^2}{w_{\text{in}}^2}\right). \tag{4.5}$$

From here, the pulse can then be propagated through an ideal lens and to the focal plane of the system.

The temporal distribution can be calculated at any position by taking a Fourier transform with respect to time of this field.

4.3 Results

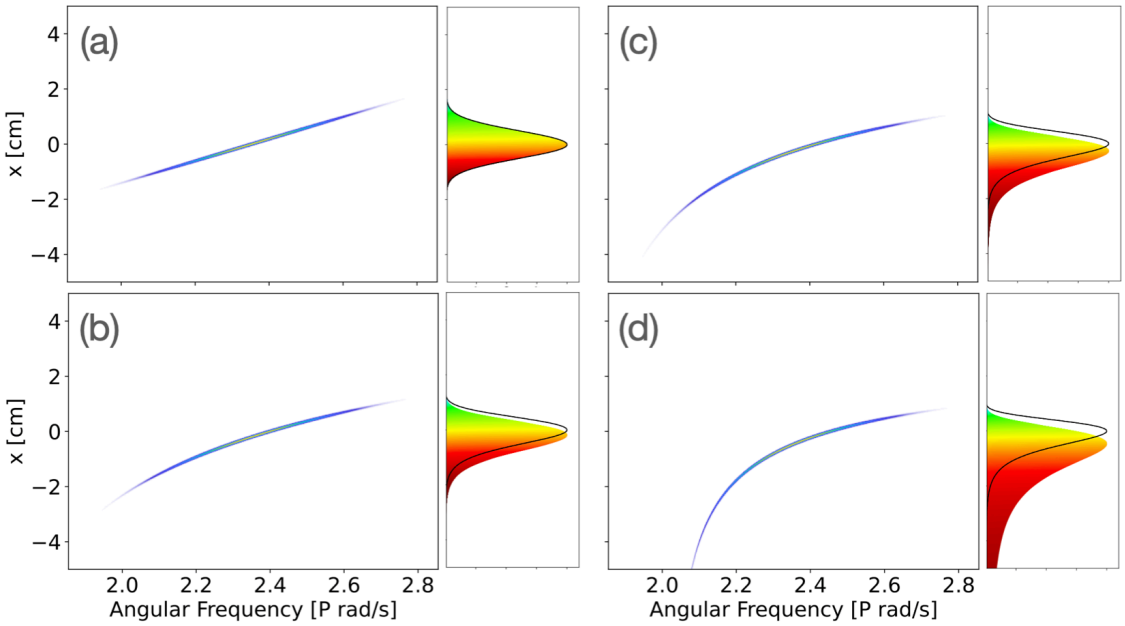

Figure 4.2: Comparison of the initial transverse fields for both linear and nonlinear spatial chirps. The chirp is shown in the space-frequency domain and also as a lineout of the intensity along the x-dimension. The colored components show the spatial chirp in the space-frequency domain, where the longer wavelengths have been diffracted more than the shorter. The solid black line shows the spatial chirp after a Fourier transform into the space-time domain. Shows a (a) linear chirp and (b)-(d) nonlinear chirp generated with angles of incidence: 52.8°, 36.3°, and 22.8°, respectively.

For all the simulations, ideal optics are assumed so that there is 100% efficiency into the $m = -1$ diffraction order of the gratings and the f-number of the system is set so there is paraxial focusing. Additionally, only the chirped spatial dimension (x) was simulated to enable increased resolution and reduce computational cost. Excluding the unchirped

spatial dimension (y) from the simulations is valid when considering large amounts of spatial chirp due to a significantly reduced contribution to intensity localization at the focus. For each grating arrangement simulated, perfect temporal chirp compensation is assumed. This enables a clearer interpretation of the influence of nonlinear spatial chirp.

The initial chirp can be represented in (x, ω) space shown in Fig. 4.2. Fig. 4.2a represents a linear chirp along the x-dimension, where a linear dependence can be seen in the spatial position of the frequency content. The higher frequencies are chirped in the positive x-direction and the lower frequencies in the negative x-direction. The frequencies are chirped symmetrically about the center frequency, ω_0. Figs. 4.2b-d show an equivalent chirp modeled with the grating equation (Eq. 4.5) for a 1480 lines/mm grating pair with varying angles of incidence. The spatial extent of the nonlinear chirps was chosen so that the angle the PFT makes with respect to the propagation axis at the focus is same for all cases. This was achieved by varying the grating separation. Each configuration was set so that the PFT angle (θ_{PFT}) was 45°. For the linear chirp, this corresponds to a $\beta_{BAR} \approx 21$, calculated from the relationship [76]:

$$\tan\left(\theta_{\mathrm{PFT}}\right) = \frac{w_{\mathrm{in}}\omega_0\sqrt{\beta_{BAR}^2 - 1}}{f\Delta\omega}, \tag{4.6}$$

with θ_{PFT} set to 45°. Due to the higher diffraction angle of the lower frequencies, there is more spectral content around the higher frequencies. This results in an asymmetry in the spatial extent of the beam. Even though the PFT at the focus was kept constant, the spatial and temporal representations of the field at the input plane of the simulations are different. The grating pair introduces the same directional dependence of chirp along the x-dimension, but the lower frequencies experience a large nonlinearity in the chirp rate, shown in Fig. 4.1. Depending on the the incidence angle used, the nonlinear dependence of the spatial chirp can be minimized. As AOI is increased, the spatial chirp becomes more linear.

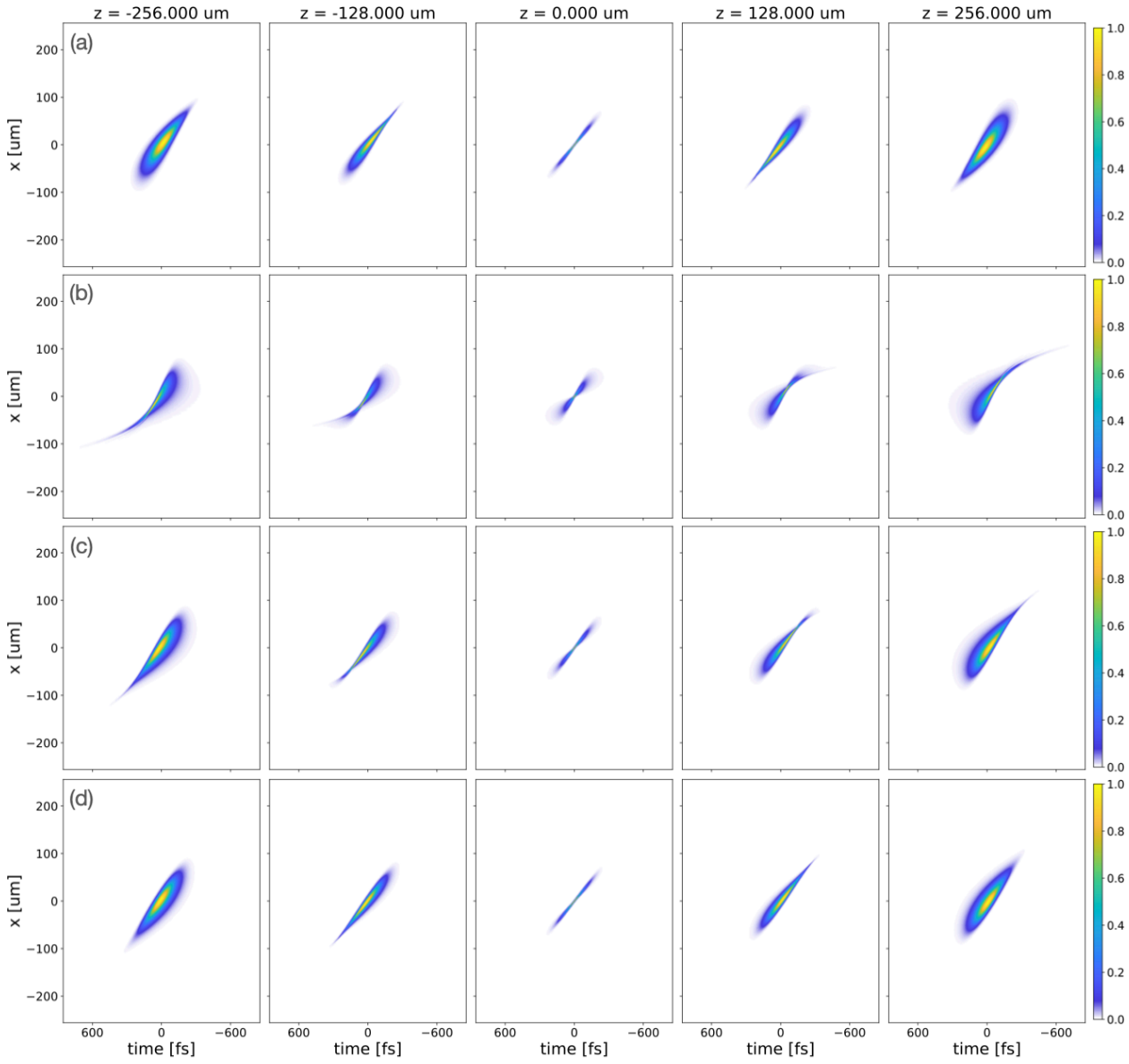

Figure 4.3: Propagation of a focused spatially chirped beam with a PFT of 45° for a linear frequency chirp and nonlinear chirp represented in (x, t) space. The temporal representations of the propagation of a (a) linear chirp and (b)-(d) nonlinear chirps generated with 1480 lines/mm gratings and incidence angles of 22.8°, 36.3°, and 52.8°, respectively, are shown.

To highlight the importance of considering the realistic chirp from a grating pair of an ultrashort pulse, the propagation of a linear chirp and equivalent nonlinear chirps are shown in Figs. 4.3 and 4.4. A grating pair with 1480 lines/mm at three typical incidence angles, 22.8°, 36.3°, and 52.8°, are simulated. These gratings and angles are used as common configurations (high dispersion, Littrow, and low dispersion, respectively) for Ti:Sapphire compressors with

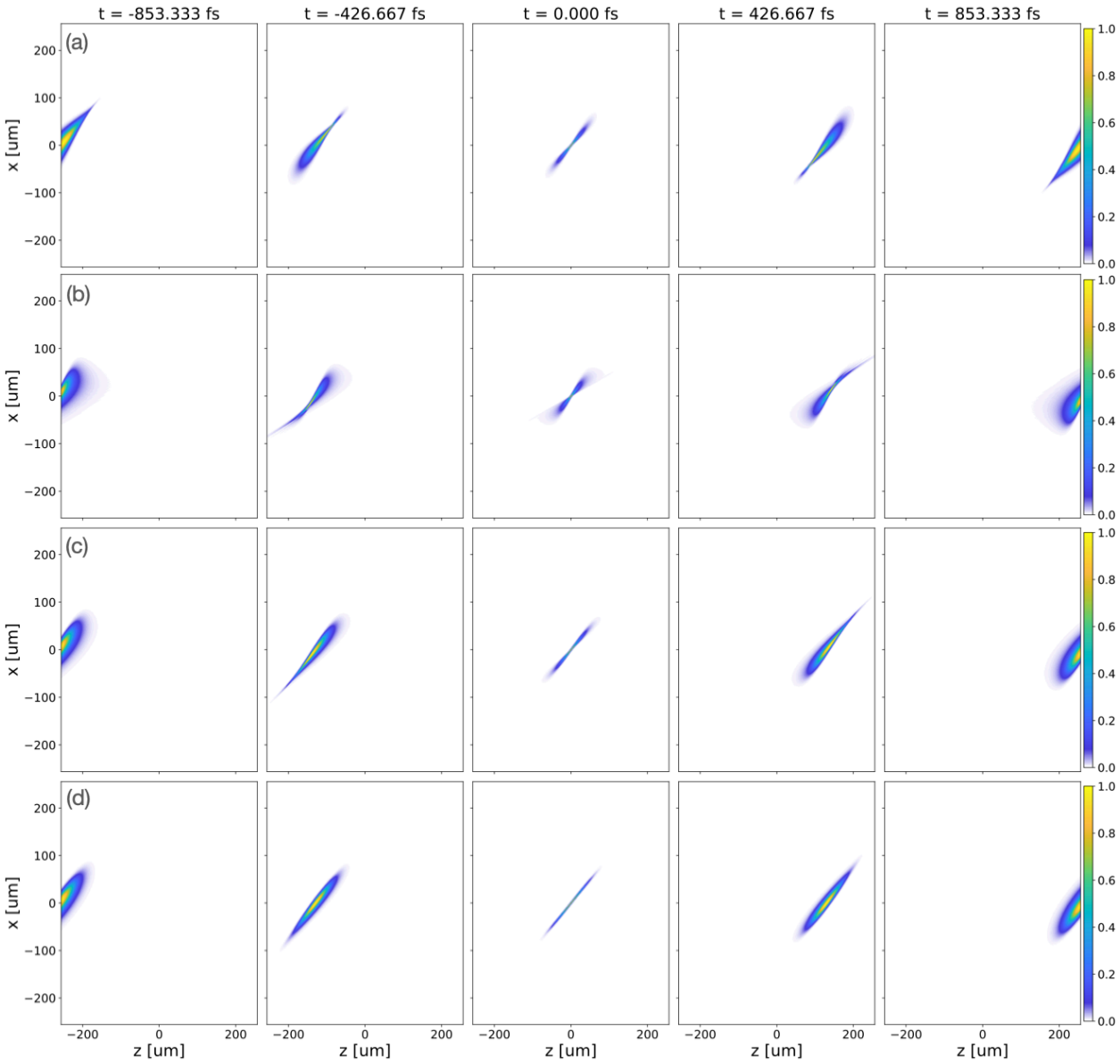

Figure 4.4: Propagation of a focused spatially chirped beam with a PFT of 45° for a linear frequency chirp and nonlinear chirp represented in (x, z) space. The spatial representation of the propagation of a (a) linear chirp and (b)-(d) nonlinear chirps generated with 1480 lines/mm gratings and incidence angles of 22.8°, 36°, and 52.8°, respectively, are shown.

high efficiency and high damage thresholds [68, 69, 70, 71]. Recent work is being conducted for this groove density on increasing supported bandwidths up to 400 nm [77]. Fig. 4.3 shows four different pulses propagating in (x, t) space at various z-positions and Fig. 4.4 shows the same pulses propagating in (x, z) space at various times, highlighting the PFC differences. Both frames of reference are important for visualization. To see how the pulse

interacts with a planar surface, in traveling wave excitation or dielectric laser acceleration for example, the (x, t) space at a z-position provides this information. The spatial dependence of the (x, z) space is relevant in electron acceleration where the gradient is proportional to the ponderomotive force. Figs. 4.3a and 4.4a illustrate the space-time and spatial focusing, respectively, of a beam chirped linearly in frequency. The PFT in this type of pulse has been shown to accelerate electrons normal to the tilted pulse front and focus an electron bunch due to the concave PFC [57, 58, 76]. Figs. 4.3b-d and 4.4b-d show the nonlinear spatial chirps.

Comparing the focal position (t = 0 fs and z = 0 μm) of both the linear and nonlinear chirps, the outside edges of the pulse structures are different, leading to various amounts of concave PFC across the cases. The chirp generated with the lower AOI has more noticeable curvature, whereas larger AOI chirps minimized the amount of variation in the pulse front. The chirp generated with the largest incidence angle had the biggest reduction in PFC at the focus, even less than the linear frequency approximation. Within the focal volume, as the pulse propagates to the focal plane, there are also significant differences in the pulse structure. In the leading frames, the curvature of the pulse front is flipped between the linear frequency approximation and the nonlinear chirp cases.

While the orientation of arrival time in the transverse extent of the pulse is the same across all cases (namely, the part of the beam in the positive x-direction leads in time), the sweeping of the smallest spatial extent across the transverse chirped dimension varies between the linear and nonlinear chirped cases. In the linear frequency approximation, the pulse sweeps from positive to negative x, whereas this direction is inverted in the realistic simulation of the grating pair. This property results in the peak intensity of the beam deviating from on-axis. Fig. 4.5 shows the location of the peak transverse intensity along with the peak intensity. The propagation effects for the linear approximation, 22.8°, 36.3°, and 52.8°cases are shown in Visualization 1, Visualization 2, Visualization 3, and Visualization 4, respectively.

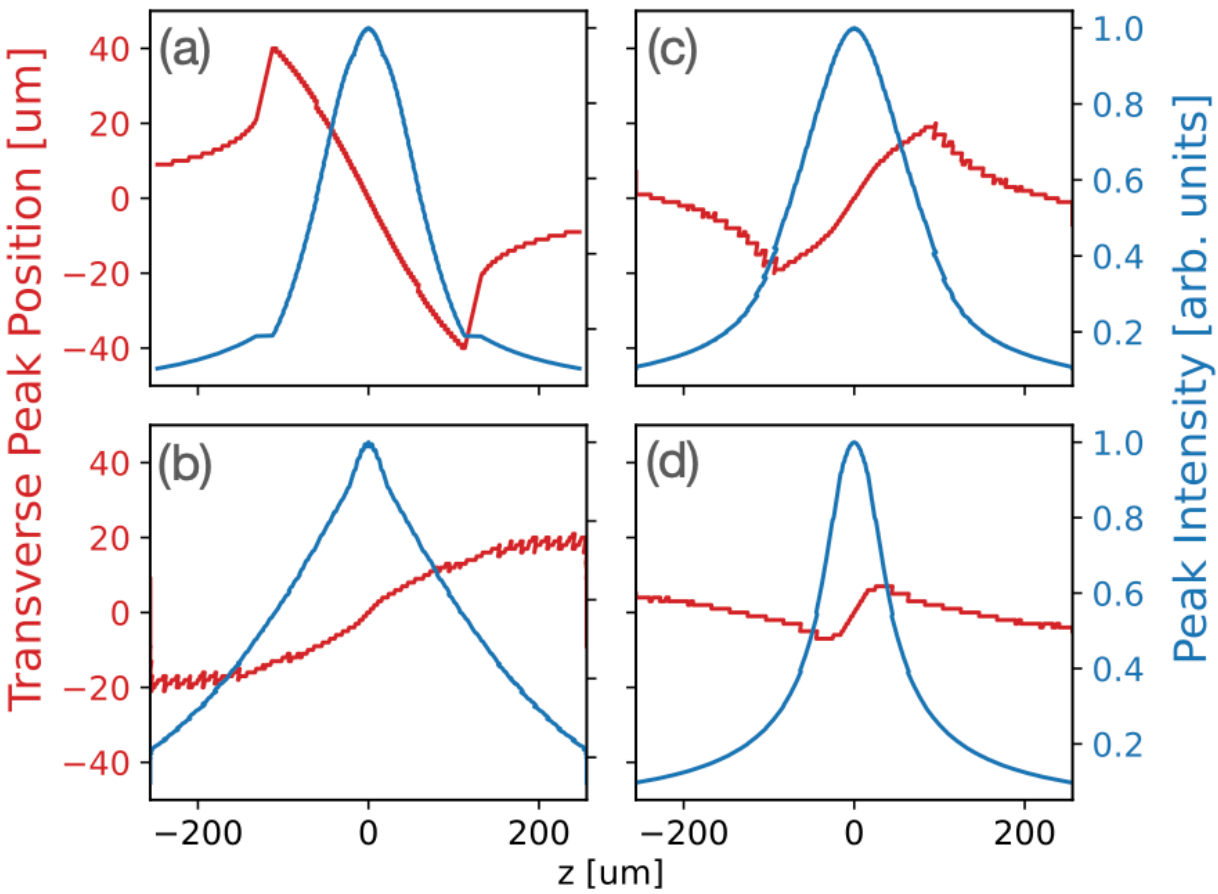

Figure 4.5: Transverse peak intensity position (red) and longitudinal intensity profile (blue) for the linear and nonlinear chirps. The (a) linear chirp and (b)-(d) nonlinear chirps for AOIs of 22.8°, 36.3°, and 52.8°, respectively, are shown.

The simulations were limited to a 1-μm resolution along the transverse dimension to reduce computation time. In all the cases, the peak intensity as the beam focuses is not on-axis ($x = 0, y = 0$) but varies with the propagation. This is contrary to the focusing of an unchirped beam where the peak intensity stays on-axis while propagating through a focus [44]. The peak intensity is more localized both longitudinally and transversely in the high AOI grating configuration (Fig. 4.5d), and progressively increases in transverse deviation for smaller angles of incidence. The linear frequency chirp approximation in Fig. 4.5a, has the largest translation in the transverse dimension, and the lowest incidence angle of 22.8° (Fig. 4.5b) has the largest longitudinal extent.

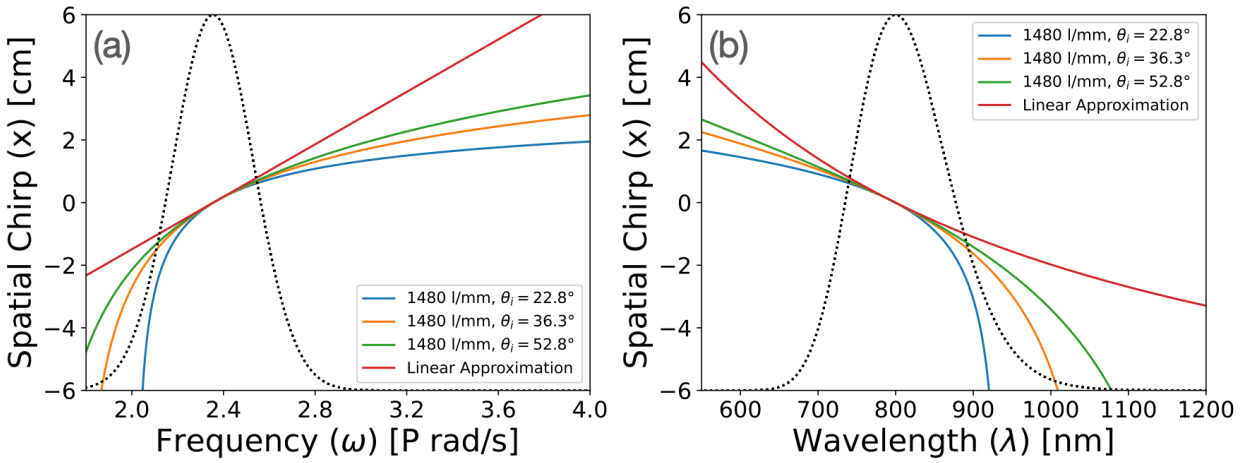

Figure 4.6: Spatial chirp as defined by Eq. 4.5 for a PFT of 45° with varying angles of incidence. The dotted line overlays the spectrum for the simulated Gaussian pulse. The spatial chirp as a function of (a) frequency and as a function of (b) wavelength.

Fig. 4.6 compares the dependence of the spatial chirp as a function of frequency and wavelength for different angles of incidence for a PFT of 45°. iconIn Fig. 4.6a, as the angle increases, the nonlinearity is reduced but never approaches linear. Converting from frequency to wavelength (Fig. 4.6b) illuminates the difference in pulse front structure of the cases shown in Figs. 4.3 and 4.4. In this representation, as the angle decreases, the spatial chirp approaches a linear trend across the bandwidth, whereas the linear frequency chirp approximation has a nonlinear trend with the opposite concavity than that from the grating pair. The grating cases are concave down, and the linear chirp is concave up. These lead to different pulse front orientations and pulse front curvatures seen in Figs. 4.3 and 4.4.

4.4 Conclusion

With the increased interest in spatio-temporal control of ultrashort pulses for high intensity laser applications, such as SSTF, it is important to understand how these pulses evolve as they propagate through the focus. For large bandwidth pulses, the linear approximation of spatial chirp from a grating pair breaks down and provides an unrealistic model for focused

spatially chirped beams. The effect of the spatial chirp nonlinearity introduced by the grating pair can change the orientation and severity of the pulse front curvature within the focal volume and, therefore, change its interaction with matter. By choosing an appropriate angle of incidence, the characteristics of the focal volume can be tuned for a given PFT. The code developed enables the ability to propagate an arbitrarily defined electric field through a focus which enables the study of higher order chirp or more complex pulse structures.

Chapter 5

2-Dimensional Spatially Chirped Beams

5.1 Introduction

Controlling the space-time structure of ultrashort pulses has become an active area of interest for generating exotic structures of focused light [78, 79, 80]. The space-time couplings required for SSTF can be fabricated through spatial light modulators [81, 82] and with dispersive or diffractive optics [83, 84]. Typically, a single pass, two grating compressor is used to generate a spatially chirped beam in one dimension that is subsequently focused, generating the SSTF space-time structure. An axisymmetric extension of 1D spatial chirp is evaluated, referred to as radial spatial chirp. The axisymmetric extension uses concentric ring, circular gratings in a similar single pass, two grating configuration. This results in a radially dependent spatial chirp from the diffraction, shown in Fig. 5.1. The radial spatial chirp maintains many of the qualities of SSTF pulses with the added symmetrization of the pulse front and the enabled capacity for vector polarization states to be studied. Fig. 5.1

shows all the possible variations of radial chirp and polarization configurations compared to 1D spatial chirp.

A path is provided for generating approximate forms of a radial spatial chirp that are highly efficient and enable easier tuning through a coherent beam combining approach of several 1D spatially chirped beams. This enables the use of current grating technology to generate beams comparable to radial spatial chirp with high damage threshold optics that have been optimized for high power lasers to enable the use of vector beams in intense laser-matter interactions, where high fluence values limit the use of transmissive optics and polarizers.

Radially chirped beams have been preliminarily studied to various extents. The focus of a radial spatial chirp generated with an axicon pair, which provides a negative spatial chirp, has been studied for its bessel-like space-time structure [85]. Radially chirped picosecond pulses have been examined for the generation of non-differentiable angular dispersion [82] to aid in propagation invariant space-time pulses with variable group velocity tuning [86, 87]. The nonlinear intra-material effects of a focused radially chirped beam have been numerically studied by varying the initial temporal group delay dispersion of the chirped pulse [88]. Additionally, focused linearly chirped, radially polarized beams have been examined [89] as a unique form of vector beams with spatio-temporal couplings. A full characterization of the properties of radial, spatially chirped beams is provided.

5.2 Methods

A pair of concentric ring gratings [90] (Fig. 5.2) can be used to generate a positive radial spatial chirp pattern, where the longer wavelengths are diffracted more such that the redder portion of the beam is farther from the propagation axis, shown in Fig. 5.1d. The amount of spatial chirp is quantified by the beam aspect ratio defined in Eq. 2.9. The distance of

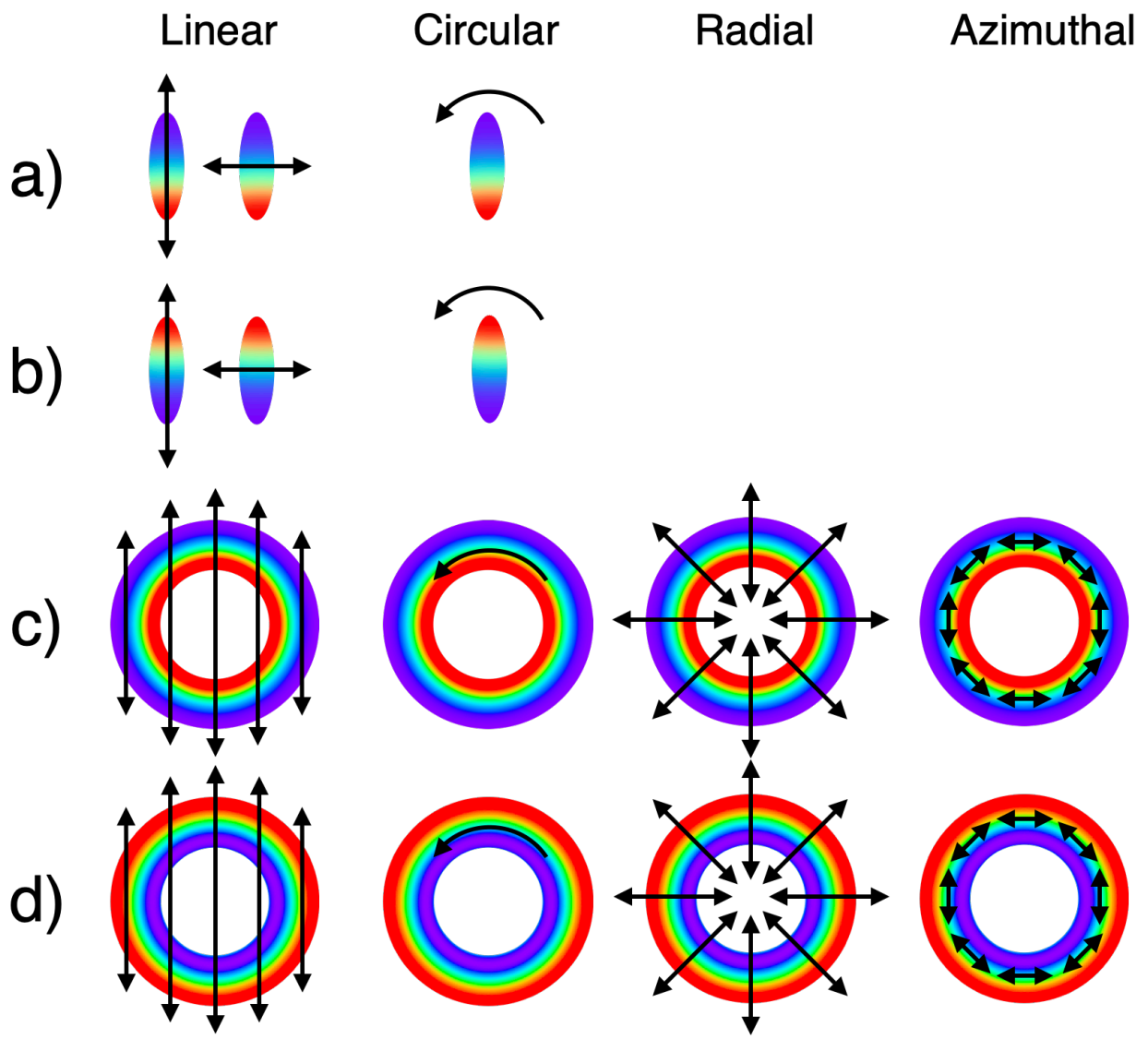

Figure 5.1: The various spatial chirp patterns and polarization orientations for a,b) 1D chirp and c,d) 2D chirp. Negative spatial chirp is shown in c) and positive spatial chirp is shown in d). The color represents the spatial dependence of the spectrum at the output of a single-pass, two grating compressor.

the center carrier frequency of the pulse from the propagation axis is defined as δr. In this configuration, D_{chirp} and δr are coupled based on the grating equation, where increasing the grating separation increases both D_{chirp} and δr. Negative spatial chirp can be achieved by using a reflective axicon pair on the output of this scheme to invert the orientation so that the longer wavelengths are closer to the propagation axis (Fig. 5.1c). The axicons can also be oriented to tune δr independently. A transmissive, refractive axicon pair can

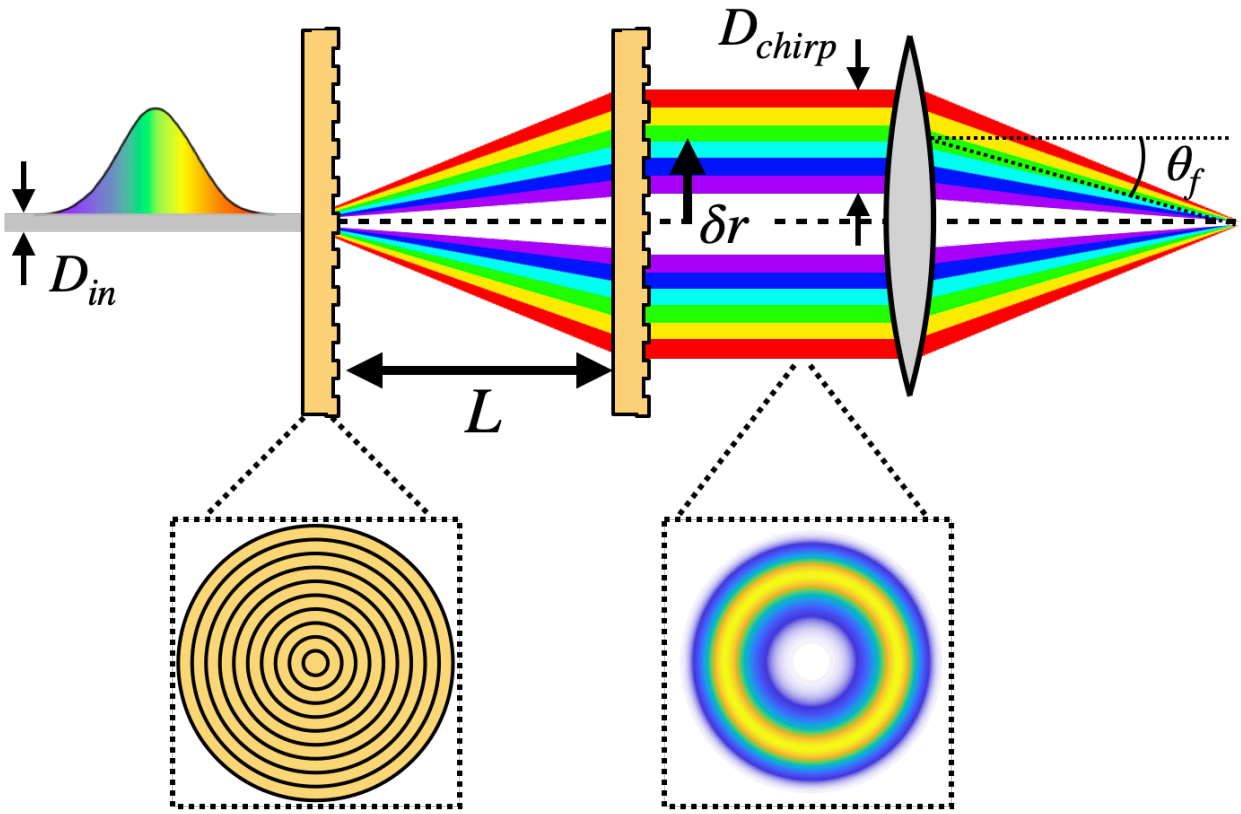

Figure 5.2: A single pass, concentric ring grating pair used to generate radial spatial chirp. The insets show the transverse profile of a concentric ring grating and the annular beam profile after the second grating.

also be used to generate negative spatial chirp [85], where shorter wavelengths refract more through the axicon material which places them on the outside edge of the beam. In order to achieve large amounts of spatial chirp over reasonable propagation distances, axicons with apex angles near the critical, total internal reflection angle must be used in order to increase the angular dispersion from the refraction. Additionally, by utilizing ring lenses [91] the spatial chirp from a grating pair can be relay imaged to flip the sign of spatial chirp.

Alternatively, approximate forms of the radial spatial chirp can be achieved through a multi-beam superposition of properly oriented 1D spatial chirps. Conventional optics can be used to generate the spatial chirp using highly efficient grating groove densities and angles of incidence. This configuration also simplifies modification of the orientation of each independent beam for control over the sign of spatial chirp, δr, and polarization.

The spatial chirp in the following simulations are derived from the grating equation to ensure accurate space-time profiles when propagated [1], and δr will be assumed to be a tunable variable through the methodologies described above. The initial spatial chirp can be quantified in the spatial-spectral domain shown in Fig. 5.3. The spatially chirped beams are simulated and propagated using the Bluestein method [30] and the Rayleigh-Sommerfeld propagator, which enables an arbitrarily sampled input plane and propagation plane. The laser simulated is based off a typical Ti:Sapphire oscillator, with a pulse centered at 800 nm with 100 nm full-width-at-half-maximum Gaussian bandwidth and a $1/e^2$ intensity beam radius 0.5 mm. Various configurations of spatial chirp, δr, and polarizations are modeled and propagated through a focal volume. The fields are propagated in the spatial-spectral domain to any longitudinal position within the focus, and can be Fourier transformed to visualize the space-time structure. For all simulations, ideal optics and paraxial focusing are assumed to enable an easier interpretation of the results directly related to the varied beam parameters.

5.3 Results

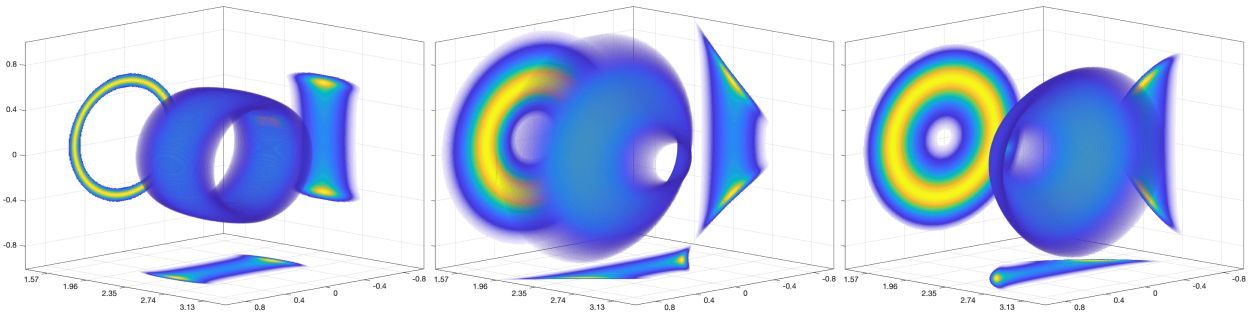

Figure 5.3: The spatio-spectral representation of an a) unchirped annular beam, b) positive radial spatial chirp, and c) negative radial spatial chirp.

Figure. 5.3 illustrates the spatio-spectral field at the input plane of the simulation for three cases: a) an unchirped annular beam that is Gaussian across its transverse profile, b) the

output of a concentric ring grating pair, and c) the grating pair output inverted around the central frequency to achieve a negative spatial chirp. The nonlinear dependence of the spatial chirp from the gratings can be seen in the lower frequencies which get diffracted at a higher rate. Radially chirping a beam results in a tunable, conical pulse front as it approaches the focus.

5.3.1 Linear Polarization

Fig. 5.4 shows the propagation of three configurations of a linearly polarized, radially chirped beam focused with an ideal lens with $f = 10\ cm$. Fig. 5.4a shows the focusing properties

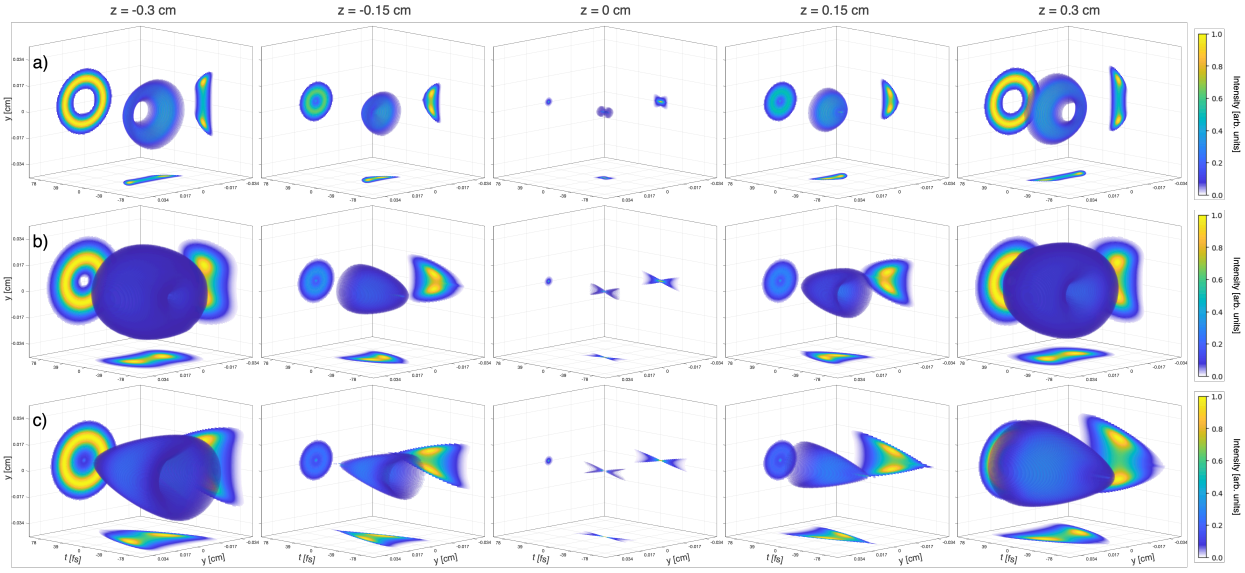

Figure 5.4: The propagation for a) an unchirped annular beam, b) a positive radially chirped beam, and c) a negative radially chirped beam. The radial chirp was generated with a grating pair of 500 lines/mm at 0^o, a $\delta r = 0.5\ cm$, and $\beta_{BAR} = 5$

of an annular ring beam. The apparent conical structure is from the off-axis focusing which results in tilted phase fronts with respect to the propagation axis. Fig. 5.4b,c show the focal volume structures of a positive and negative radial spatial chirp. The orientation of the conical pulse front flips between the two cases and the pulse structure along the propagation axis is varied. Both the PFT angle and the angle of the tilted phase fronts contribute to

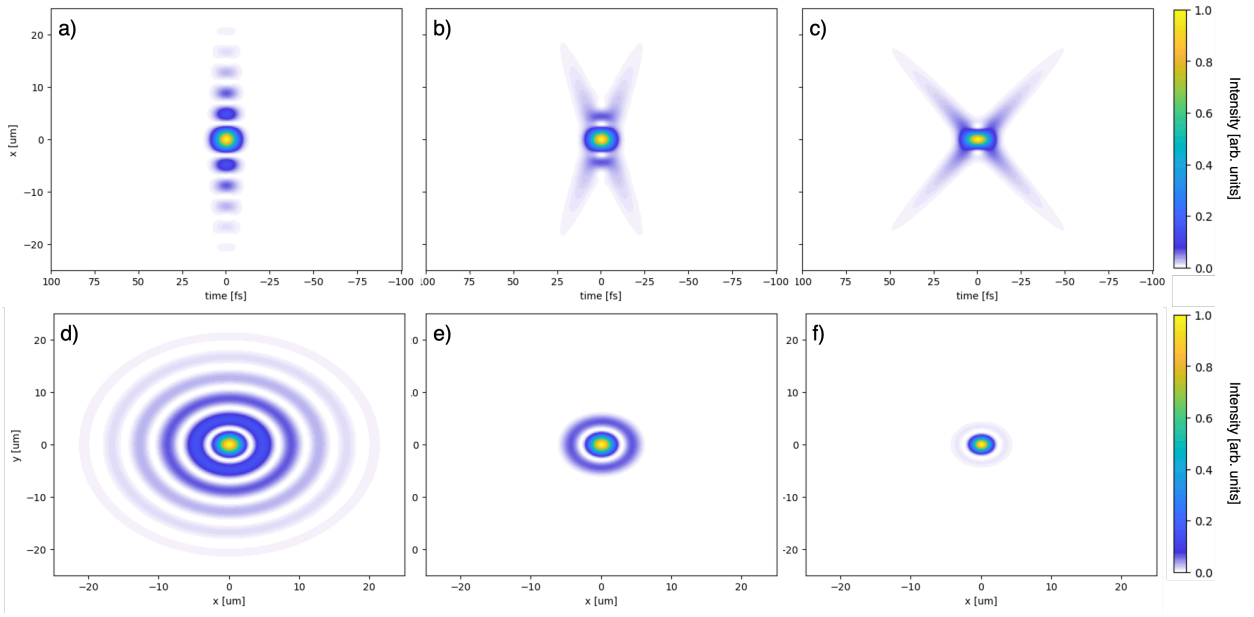

Figure 5.5: (x,t) and (x,y) representations of the focus ($f = 10\ cm$) for a linearly polarized pulse with $\delta r = 0.5$ cm and β_{BAR} of a,d) 1, b,e) 2, c,f) 5 generated with a 500 lines/mm grating pair.

the shape of the focal structure and are two parameters that can be controlled through the amount of spatial chirp (β_{BAR}) and the distance of the central frequency from the propagation axis (δr).

These values are varied independently to highlight the effect of each, and the resulting fields at the focal plane are compared in Figs. 5.5 and 5.6. In Fig. 5.5, β_{BAR} is varied for a constant $\delta r = 0.5\ cm$. As β_{BAR} increases, the PFT angle increases. Increasing β_{BAR} also has the advantage of decreasing the local bandwidth, thus increasing the local pulse duration away from the focus. This effect has been shown to enable intra-material writing due to a decrease in the onset of nonlinear, power related effects such as self-focusing [73, 92]. In Fig. 5.6, δr is modified while keeping β_{BAR} fixed. As δr increases, the frequency of the transverse interference modulation increases and the central spot diameter decreases.

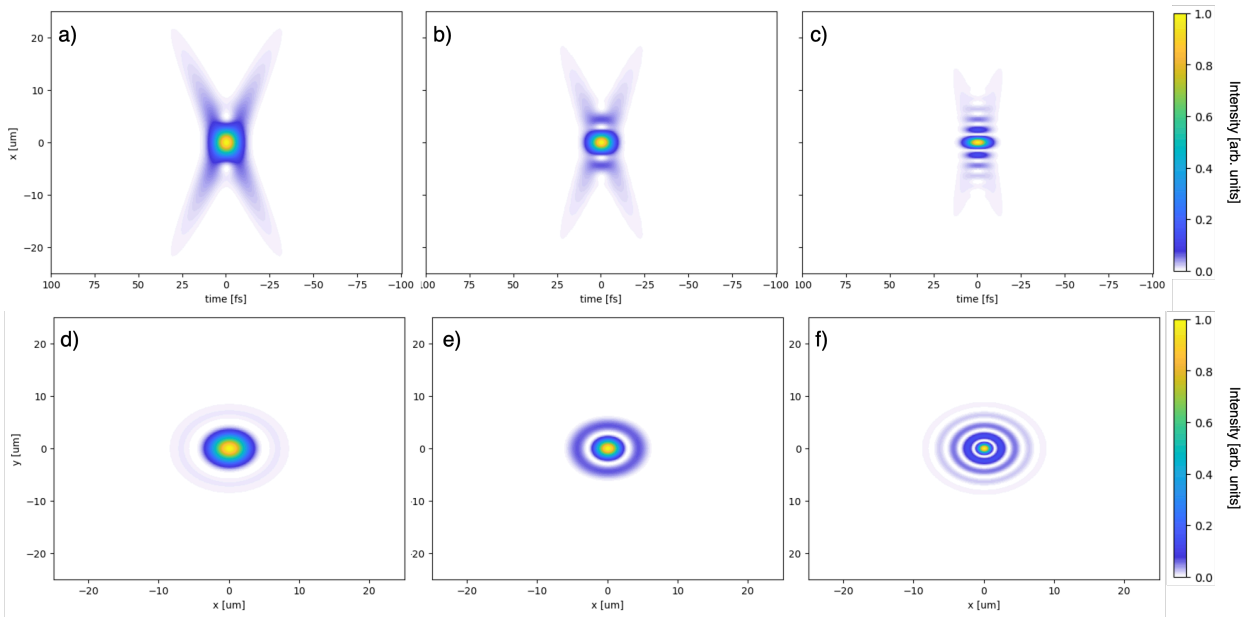

Figure 5.6: (x,t) and (x,y) representations of the focus ($f = 10\ cm$) for a linearly polarized pulse with $\beta_{BAR} = 5$ generated with a 500 lines/mm grating pair and δr of a,d) 0.25 cm, b,e) 0.5 cm, c,f) 1 cm.

5.3.2 Radial Polarization

Similar trends are observed when considering radial polarization. The primary difference is that there is no transverse electric field on axis due to the spatially dependent orientation of the polarization. The envelope of the off-axis structure is comparable to linear polarization, but near the focus, the intensity localization of the transverse fields are different. With radial polarization, the peak transverse intensity is less localized around the propagation axis due to the reduced constructive interference from the spatially dependent polarization state. As the radially polarized fields come to a focus, the on-axis component of the transverse field evolves into a longitudinal field along the propagation direction. The longitudinal field can become quite significant for low f-number systems and can achieve sub-diffraction limited spot sizes [93, 94]. Additionally, these strong longitudinal fields have been shown to effectively accelerate electrons [95].

β_{BAR} and δr are also varied independently in Figs. 5.7 and 5.8. The trend of increasing

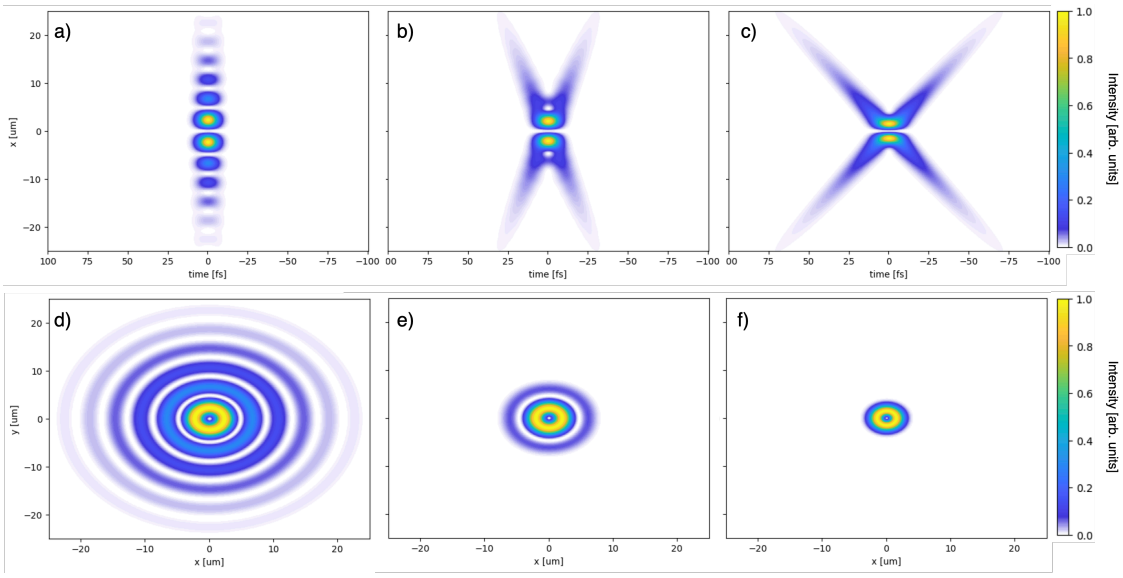

Figure 5.7: (x,t) and (x,y) representation of the focus ($f = 10\ cm$) for a radially polarized pulse with $\delta r = 0.5$ cm and β_{BAR} of a,d) 1, b,e) 2, c,f) 5 generated with a 500 lines/mm grating pair.

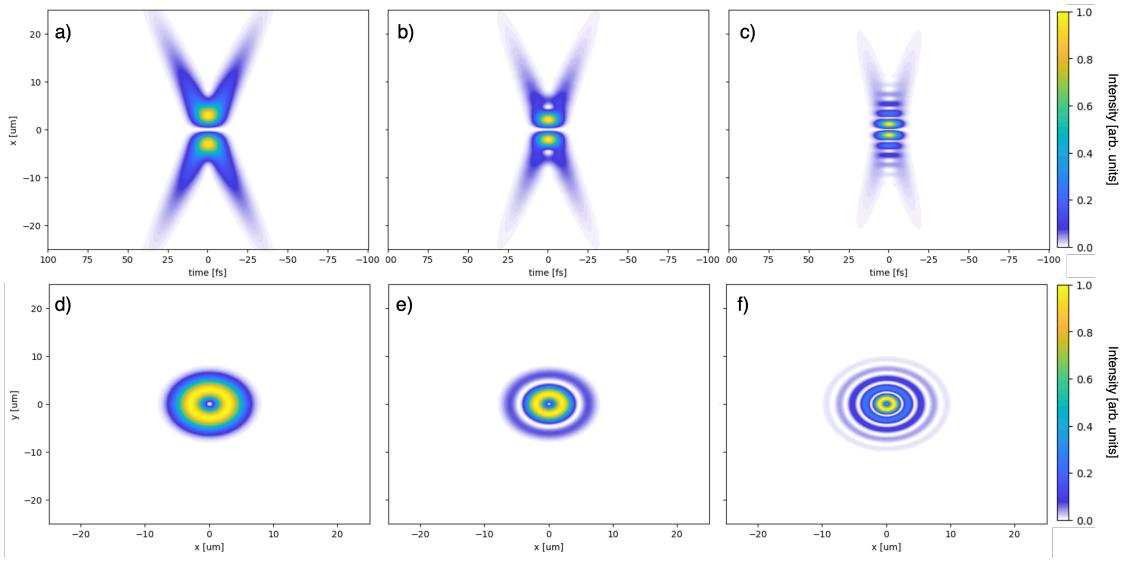

Figure 5.8: (x,t) and (x,y) representations of the focus ($f = 10\ cm$) for a radially polarized pulse with $\beta_{BAR} = 5$ generated with a 500 lines/mm grating pair and δr of a,d) 0.25 cm, b,e) 0.5 cm, c,f) 1 cm.

the PFT angle with increasing β_{BAR}, and increasing intensity modulations with δr are also present for radial polarization. The primary difference is the lack of transverse field intensity on-axis.

The electric field at the focus can also be visualized to confirm the polarization structure of the pulses. In Fig. 5.9, the transverse electric field is shown at the focus for $t = 0$ for a radially chirped beam with $\delta r = 0.5\ cm$ and a $\beta_{BAR} = 5$

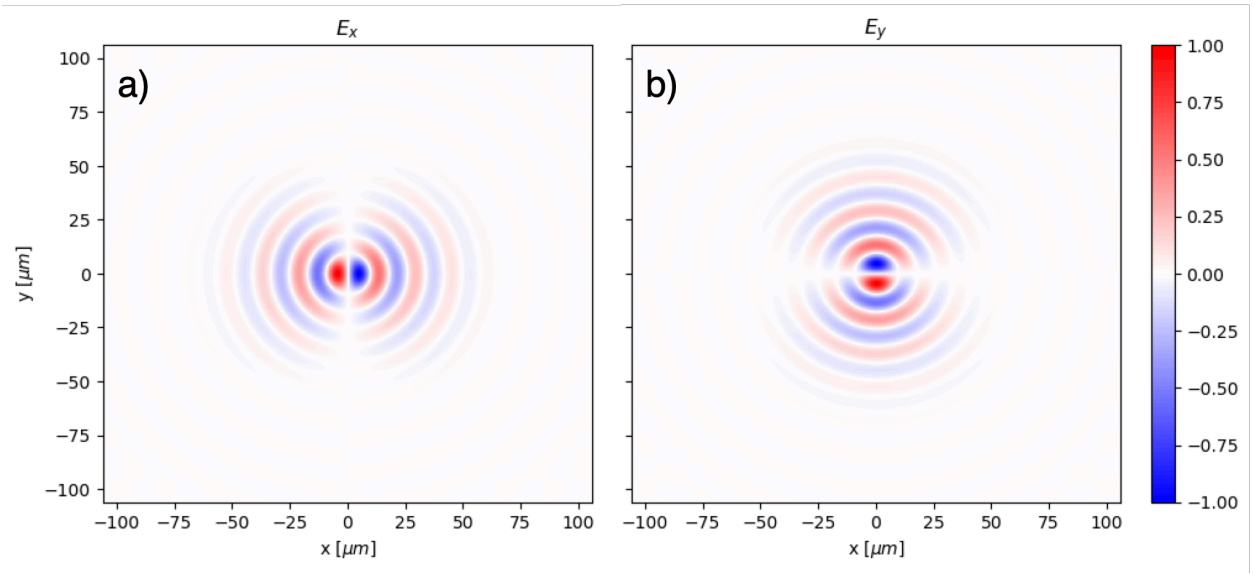

Figure 5.9: The (x,y) representation for a radially polarized pulse at the focus ($f = 10\ cm$) for a $\beta_{BAR} = 5$ and $\delta r = 0.5\ cm$ are shown for a) E_x and b) E_y.

5.3.3 Azimuthal Polarization

Azimuthal polarization is another spatially dependent polarization state, visualized in Fig. 5.1. The polarization is not defined on axis at $x = 0$, $y = 0$, so the field amplitude must reach zero as in the case of the radial polarization. The intensity profile of the azimuthal polarization looks identical to the radial polarization, but the electric field structure differs. The electric field at the focus for the azimuthally polarized beam is shown in Fig. 5.10. The annular nature of the radially chirped beams naturally leads to the use of the radial and azimuthal vector polarization states.

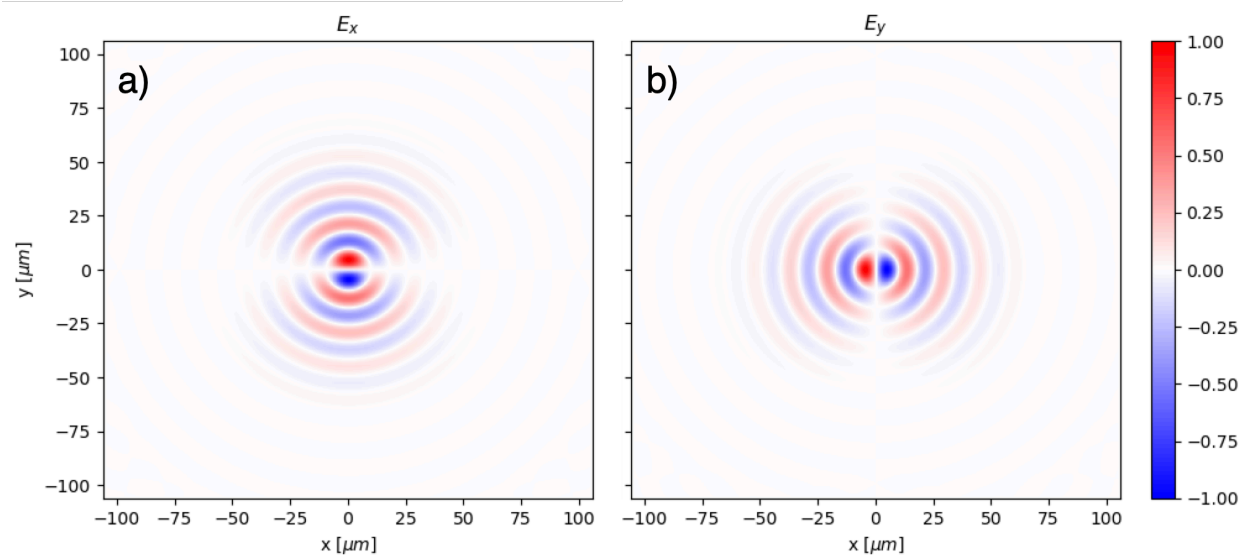

Figure 5.10: The (x,y) representation for an azimuthally polarized pulse at the focus ($f = 10\ cm$) for a $\beta_{BAR} = 5$ and $\delta r = 0.5\ cm$ are shown for a) E_x and b) E_y.

5.3.4 Circular Polarization

Circular polarization is a variation of a linear polarization state, where two orthogonal field components are 90^o out-of-phase with each other.

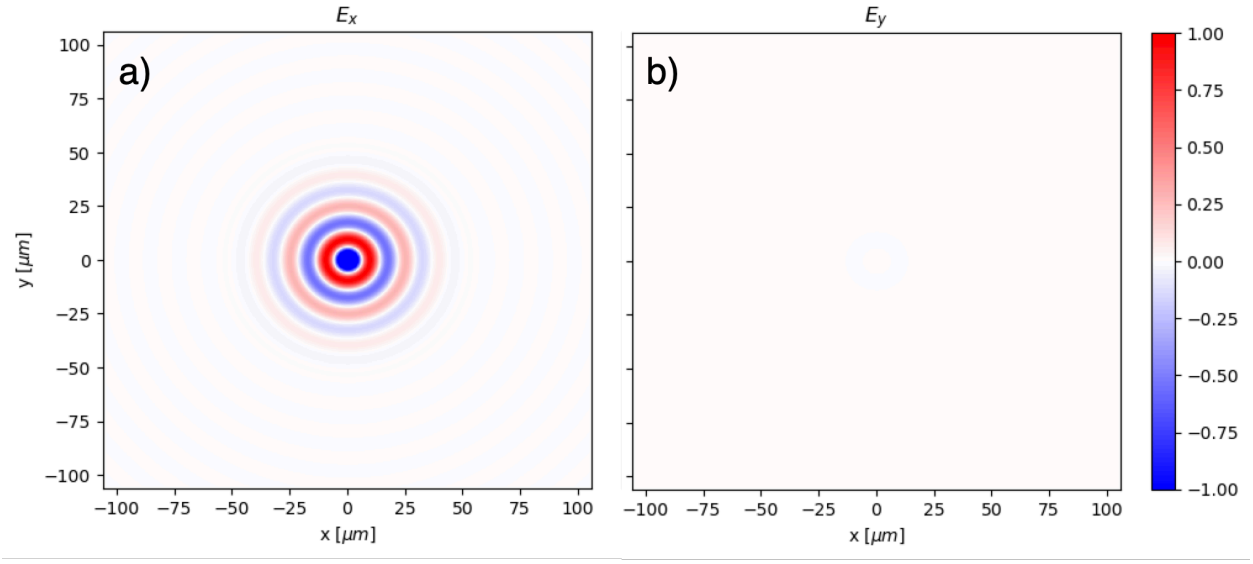

Figure 5.11: The (x,y) representation for a circularly polarized pulse at the focus for a $\beta_{BAR} = 5$ and $\delta r = 0.5\ cm$ are shown for a) E_x and b) E_y

Circular polarization is commonly seen in high-intensity laser accelerated ion simulations and experiments because of its unique structure that minimizes $J \times B$ heating of electrons from an intense laser [96]. The $J \times B$ term seen in the Lorentz force equation becomes zero, which drastically reduces electron heating and gives rise to different acceleration dynamics. Circularly polarized light is typically sought after when studying the RPA mechanism due to the reduction in electron heating. The electric field at the focus for a circularly polarized beam is shown in Fig. 5.11.

5.3.5 Tunable Longitudinal Group Velocity

Additionally, the tunability of the pulse front angle of the radial chirp enables much more drastic control of the on-axis group velocity compared to that of an annular beam focused through an axicon [97]. By tuning the grating separation or groove density to give varying values of PFT and δr, in conjunction with different focusing conditions, the group velocity can be tuned from superluminal to subluminal, and to even negative values.

The on-axis group velocity for these radial spatially chirped beams is not constant throughout propagation. Fig. 5.12 shows how the group velocity changes during propagation near the focus for different values of spatial chirp. The variable group velocity is due to two primary effects. First, the PFT angle of a focused, spatially chirped beam does not remain constant throughout propagation and gradually increases to a maximum at the focus, following the form [76]:

$$\theta_{PFT} = \tan^{-1}\left[\frac{w_{in}\sqrt{\beta_{BAR}}}{\Delta\omega f}\left(\frac{1}{1+z^2/z_R^2}\right)\right] \tag{5.1}$$

where z is the propagation distance from the focus. For positive PFT, the increase in PFT angle during propagation towards the focus increases group velocity. Similarly, the decrease in PFT angle during propagation away from the focus decreases group velocity. The opposite

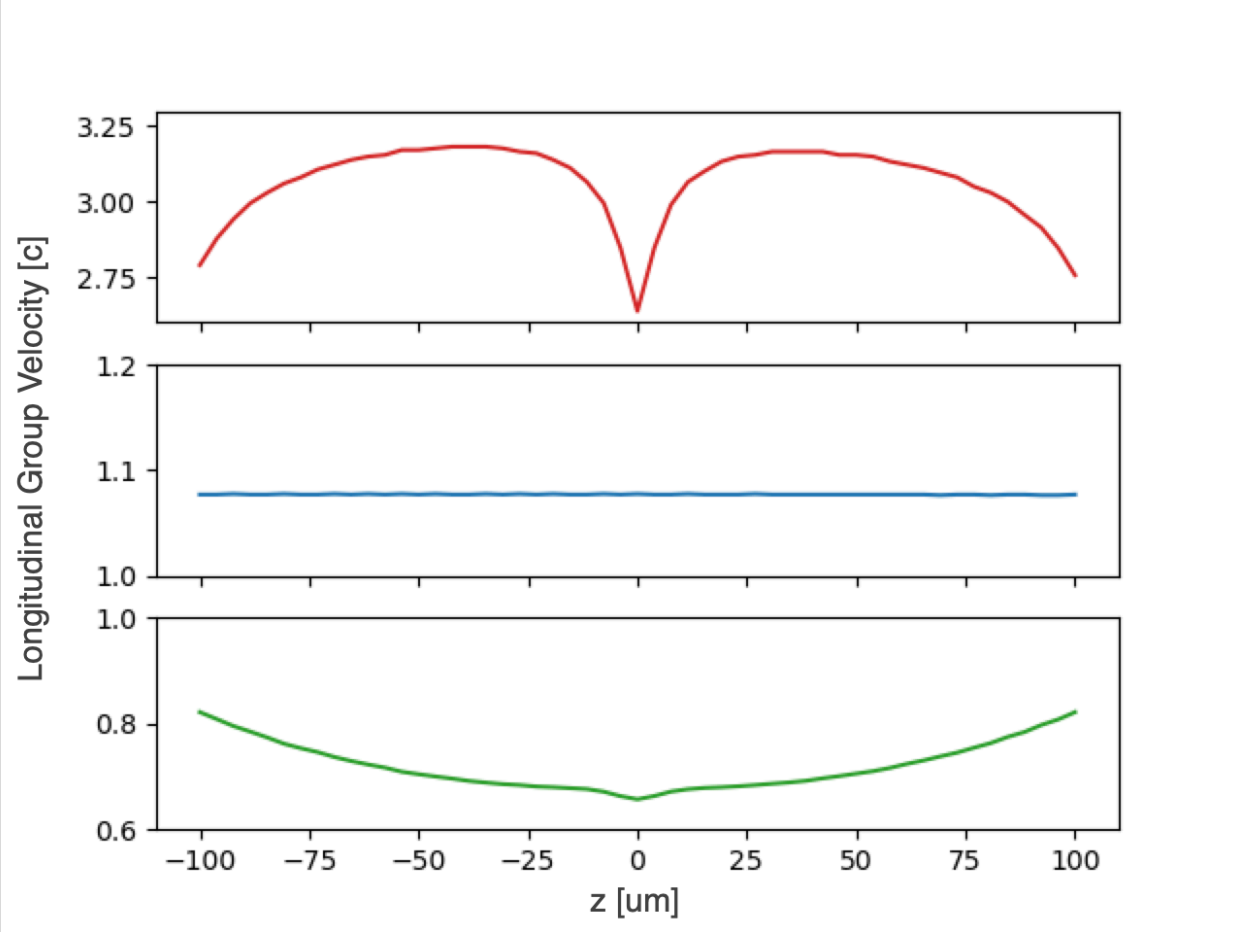

Figure 5.12: The group velocity as a function of position from the focus of a (a) negative spatial chirp, (b) no spatial chirp, and a (c) positive spatial chirp. The simulation parameters were: $\beta_{BAR} = 20$, $f = 5\ cm$, 500 lines/mm groove density gratings.

is true for negative PFT. The second effect is that the centroids of a focused spatially chirped beam do not propagate in a straight line from the lens to the focus, but rather translate across the transverse dimension, shown in Fig. 4.5. This shift causes the group velocity to rapidly slow near the focus for both negative and positive spatial chirps. The combination of these effects results in the opposite concavity of group velocity for negative and positive spatial chirp but with similar dips near the focus.

The longitudinal group velocity at the focus ($z = 0$) (assuming a linear chirp approximation) follows the form:

$$v_{g,z} = \frac{c}{n\cos\theta_f(\omega_0)}\left[1 - \tan\theta_f(\omega_0)\frac{w_{in}\sqrt{\beta_{BAR}^2 - 1}}{\Delta\omega f\left(1 + (\theta_f(\omega_0))^2\right)}\right]^{-1} \tag{5.2}$$

where ω_0 is the carrier frequency of the pulse, $\theta_f(\omega_0) = \delta r/f$ and n is the material index of refraction (n=1 in the following simulations for vacuum propagation). Fig. 5.13a shows how the on-axis group velocity varies for three different f-number systems. The on-axis group velocities reach an asymptote in both the positive and negative group velocity regimes, meaning that the value can be varied from extremely negative to extremely positive values with careful tuning of the PFT angle for a given focusing system. These regimes are explicitly illustrated in Fig. 5.14, where the three cases of group velocity are portrayed with a representative model of a radially chirped beam in the x-z plane. With a sufficiently negative PFT with respect to the propagation direction (positive spatial chirp depicted in 5.1d) in Fig. 5.14a, the longitudinal group velocity will result in a value less than the speed of light as the beams cross the z-axis. With positive PFT (negative spatial chirp depicted in 5.1c), the value can be either greater than c or negative. For relatively small angles of PFT and shallow focusing, the value will be greater than c, as in Fig. 5.14b. As the pulse front increases or F/# decreases, the pulse front can be tilted so strongly that it becomes an extremely negative tilt with respect to the z-axis, resulting in a strong negative longitudinal group velocity effect, illustrated in Fig. 5.14c. Smaller f-numbers require smaller values of PFT to achieve drastically large positive or negative group velocities due to the stronger focus decreasing the angle the phase fronts make with respect to the z-axis. Fig. 5.14a, and 5.14c illustrate two chirps of equal PFT angle but opposite signs relative to the phase fronts. But, due to the focusing effects, they cross over the z-axis with different relative orientations. A larger PFT angle will result in a more noticeable difference between a positive and negative chirp, as will stronger focusing. Fig. 5.14d shows an unchirped beam, where there is no tilt of the pulse front relative to the phase fronts.

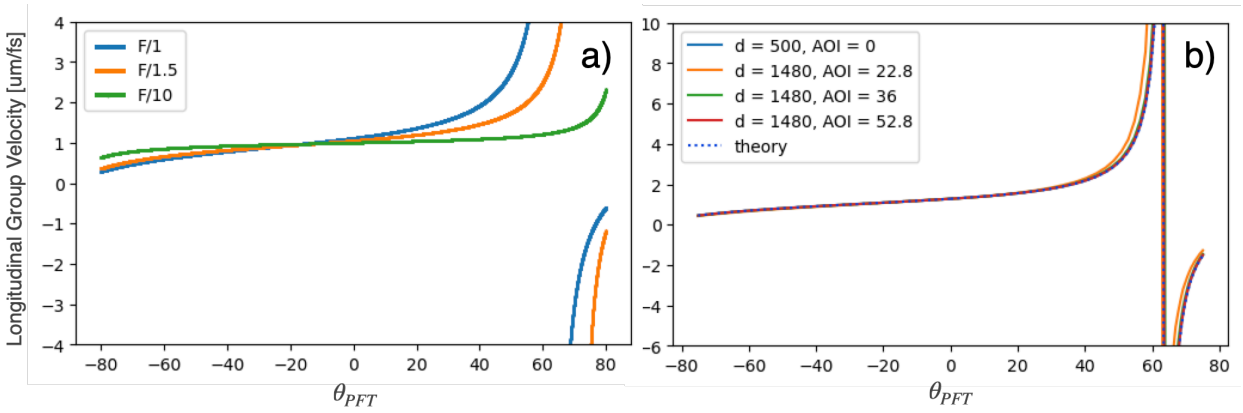

Figure 5.13: Group velocity as a function of PFT angle for a) different f-number focusing systems by varying focal length and for an F/1 system varying groove density and AOI.

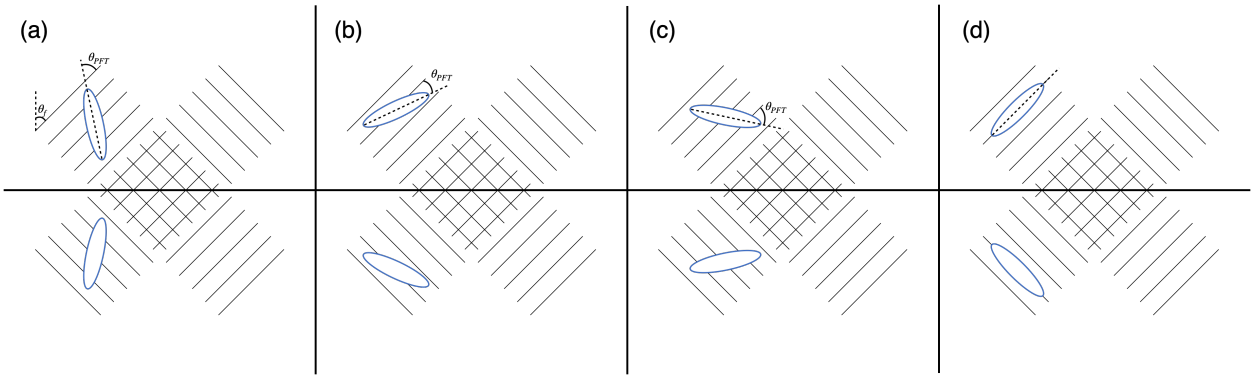

Figure 5.14: The four different regimes of focusing possible with symmetrically chirped beams. The pulse front tilt angle, θ_{PFT} is defined with respect to the phase fronts which are shown as solid lines. (a) negative PFT, (b) positive PFT, (c) positive PFT and $\theta_{PFT} + \theta_f > 90^o$, (d) no PFT.

Fig. 5.13b shows the group velocity trend for different groove density gratings at various orientations. Due the nonlinear nature of the spatial chirp from the grating pair, using different angles of incidence and grating periods can have varying effects on the pulse front structure. As the nonlinearity from the spatial chirp generated from a grating pair increases, the group velocity starts to diverge from the expected value. The largest nonlinearity occurs for high groove density gratings at low angles of incidence, which is the only configuration that results in the asymptote shifting to the left towards lower values of pulse front tilt. Thus, using high groove density gratings at a shallow AOI requires less drastic pulse front tilt to achieve a certain group velocity compared to using lower groove densities or higher

angles on incidence.

5.3.6 Multi-Beam Approach

Generating a radial chirp with a concentric ring grating pair is a simple method, but has limited tunability, requiring off axis reflective axicons or other specialty optics to independently control β_{BAR}, δr, and chirp orientation. An alternative approach of approximating a radial

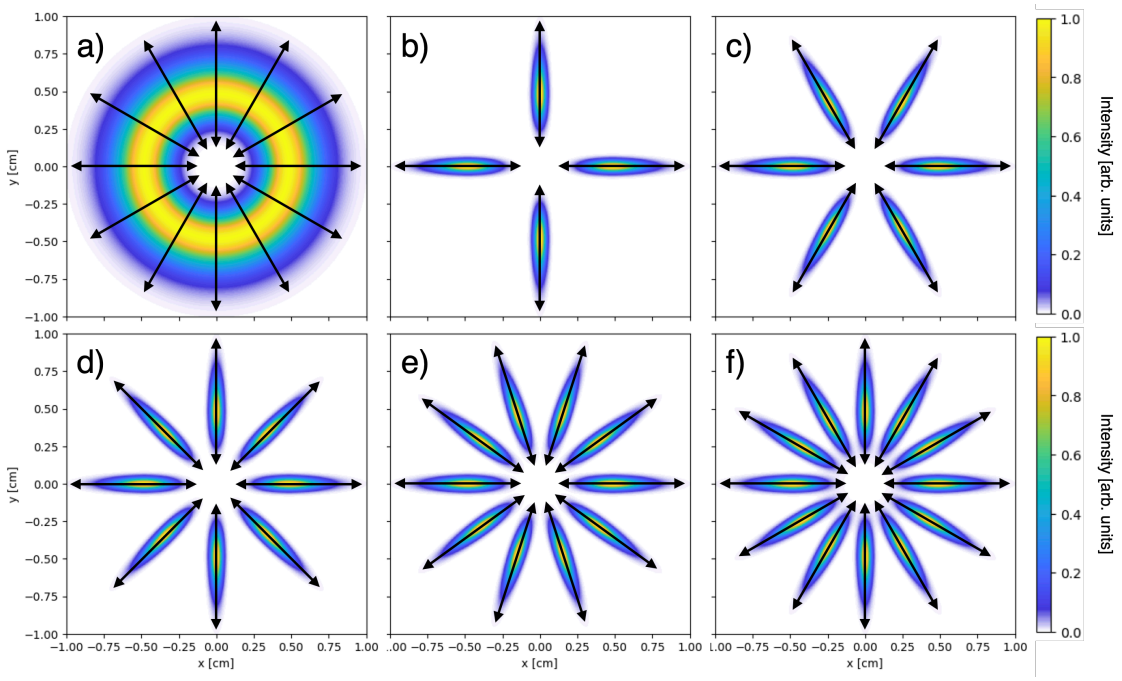

Figure 5.15: The transverse intensity before focusing for a radially polarized a) radially chirped beam and b)-f) 4, 6, 8, 10, and 12 1D spatially chirped beam approximations.

chirp is shown using multiple beam lines that are coherently combined, which offers the benefit of using conventional optics and increasing the ease of tunability, offering highly efficient, arbitrary control over the pulse structure. Fig. 5.15 shows the transverse profile at the input plane before a focusing optic for a positive radially chirped beam with radial polarization, along with various numbers of 1D spatially chirped beams. The 1D spatially chirped beams are arranged such that they have the same orientation, spatial chirp, δr, and polarization as the radially chirped beam. This arrangement is a discrete approximation to the radial chirp,

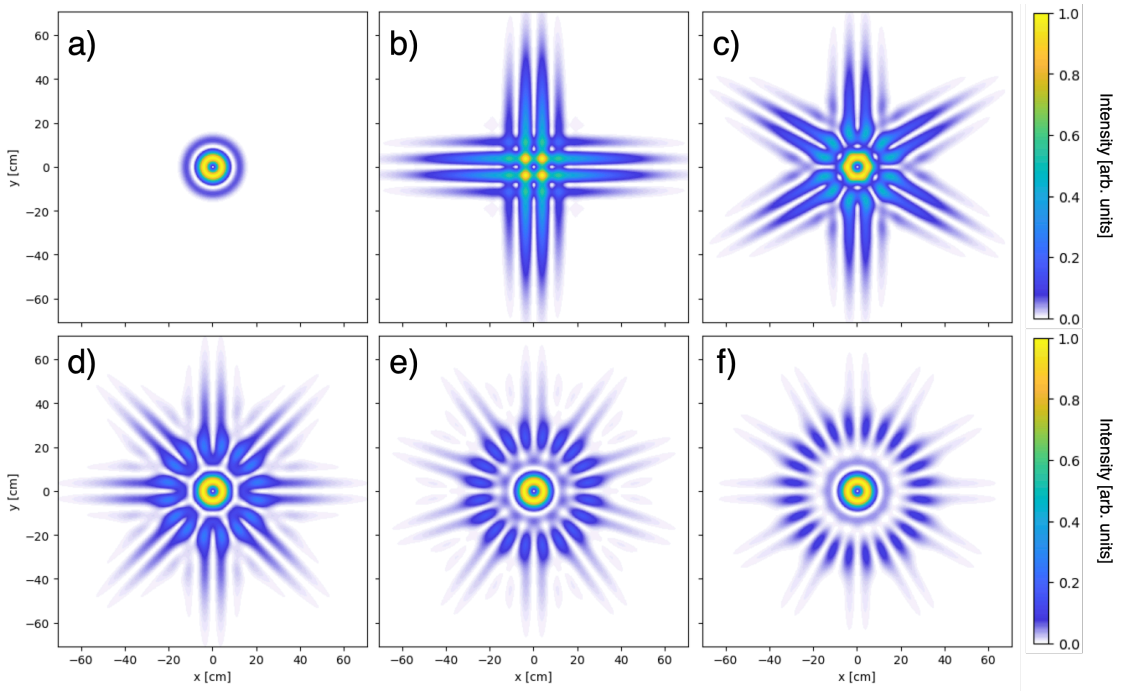

Figure 5.16: The transverse intensity at the focus for a radially polarized a) radially chirped beam and b)-f) 4, 6, 8, 10, and 12 1D spatially chirped beam approximations.

and the more beams that are added, the closer it models the full spatio-temporal structure of the radially chirped input beam.

The focal plane becomes more closely approximated to the focus of the radially chirped beam as number of beams increases, depicted in Fig. 5.16. The primary central peak starts to form for 6 beams, but additional high intensity lobes remain on the outside edge of the beam. The relative, radially integrated intensity can be seen in Fig. 5.17. Once 10 beams are used, the peak intensity of the outside edge drops to less than 10 percent. The central lobe becomes more prominent relative to the wings as the number of beams increases. The ability to arbitrarily control the orientation and polarization of each beam line enables the ability to create any polarization structure with typical half- or quarter-waveplates.

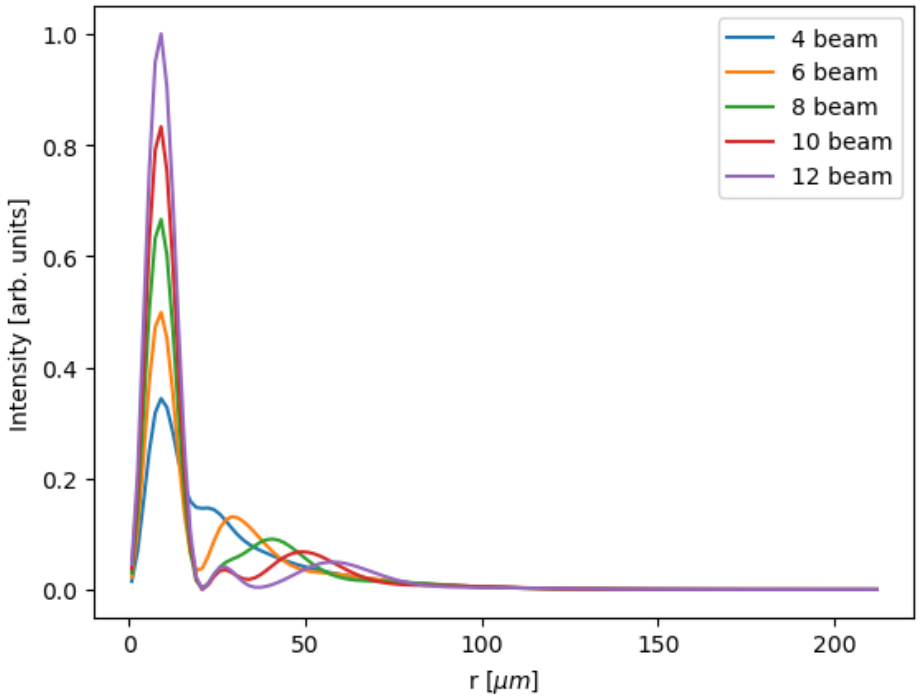

Figure 5.17: The radially integrated intensity profile at the focus for 4, 6, 8, 10, and 12 beam approximations to the radial chirp.

5.4 Conclusion

With the increased interest in spatio-temporal control of ultrashort pulses and the study of vector beams, it is important to study how these complex pulses evolve as they propagate through their foci. The radially chirped beams presented have many tunable properties and focusing effects, such as a symmetrized pulse front, variable longitudinal group velocity, and polarization. The ability to approximate the radially chirped beam using 1D spatially chirped beams enables the use of high efficiency optical components for the generation of the pulse structure.

Chapter 6

Laser-Foil Interactions with Focused Spatially Chirped Beams

6.1 Introduction

The spatial intensity profile and PFT of the focused spatially chirped beams offers potentially interesting interaction dynamics with a foil beyond that of the typically studied Gaussian beam. Much of the electron and proton acceleration relates to the orientation of the electric field oscillations when interacting with the foil and also the gradient of the intensity of the pulse resulting in the direction of the ponderomotive force. For focused spatially chirped beams, the pulse front curvature directly affects the intensity gradient, and the pulse front tilt decouples the electric field oscillation from the plane of constant intensity. The particle-in-cell code, Smilei, was used to model the laser-foil interaction. Smilei, like many PIC codes, offers the ability to model several spatial and temporal laser pulse profiles, such as Gaussian, trapezoidal, polynomial, along with the ability for custom profiles that are defined within the PIC simulation window. For complex space-time coupled beams, the analytic expression

for the field at a plane within the simulation may not be known, making it impossible to model within Smilei. To solve this issue, enabling the study of focused spatially chirped beam laser-foil interactions, the Fourier propagation code was implemented as a front-end to Smilei. The field is known before focusing, which is then propagated to the edge of the PIC simulation window. The field is then passed into Smilei with a hand off technique, where the PIC loop then takes over the propagation and interaction dynamics. This feature enables the study of not only focused spatially chirped beams, but any arbitrary field (as long as the field is known at any point along its propagation path). Even measured experimental pulse information can be imported into the front-end and propagated through the PIC simulation, using a measured spatial profile, pulse characterization, and phase information.

6.2 Fourier Propagation Implementation

The implementation starts with a user-supplied input field defined in either position-frequency space or position-temporal space. If the input is in temporal space, the field is first Fourier transformed into frequency space which is required for the Fourier propagation. The field is then focused by applying the phase of an ideal focusing optic. The field is propagated in vacuum using Rayleigh-Sommerfeld propagation from the focusing optic to the edge of the PIC simulation window. Additionally, the Bluestein technique is used to enable the input plane field and focal plane field to have different sampling requirements. Typically, the spatial scale of PW lasers before focusing are 10s of cm in diameter and are focused down to around 10 μm in diameter. The ability to scale the two planes relative to the size of the beam drastically reduces the computational time and memory resources needed for the Fourier propagation. Once the field is propagated and defined at the PIC simulation window, it is Fourier transformed to retrieve the space-time field, which is the required input into Smilei. The field at this plane is interpolated to have the same resolution as the desired

PIC simulation and then passed as a laser field into SMILEI. At this point, SMILEI fully takes over and the simulation is initialized and the PIC loop commences.

6.2.1 Code Validation

The Fourier front-end hand-off technique is validated to give accurate fields within SMILEI. The built-in Gaussian laser in SMILEI is compared to the approximated Fourier propagated pulse (the monochromatic assumption discussed in Section 3.2), in order to match the model used in SMILEI. The parameters used in the PIC simulation and Fourier propagation are shown in Table. 6.1. The spatial window dimensions are defined by the x, y, and z dimension parameters. The step size of the grid resolution is defined by dx, dy, and dz, respectively. The time duration is the extent of the temporal window, with step size dt. The Fourier code is defined for two transverse spatial coordinates and a temporal coordinate, while the PIC simulation has three spatial coordinates and a temporal coordinate. The input plane of the Fourier code is defined in Table. 6.1 as the Fourier Input Grid. The plane after focusing and propagating to the PIC simulation window is referred to as the Fourier Output Grid. PIC Grid are the parameters for the PIC simulation.

The propagation of the two methods is compared in Fig. 6.1 for a 25 fs, 1 μm pulse focused to a 4 μm, $1/e^2$ radius spot size. In both cases, the laser of focused at $x = 50$ μm. The

Parameters	Fourier Input Grid	Fourier Output Grid	PIC Grid
dy	$0.5882cm$	$0.117\mu m$	$0.0625\mu m$
dz	$0.5882cm$	$0.117\mu m$	$0.0625\mu m$
dx	N/A	N/A	$0.0625\mu m$
dt	$0.146fs$	$0.146fs$	$0.114fs$
y-dimension	$150cm$	$60\mu m$	$28\mu m$
z-dimension	$150cm$	$60\mu m$	$28\mu m$
x-dimension	N/A	N/A	$100\mu m$
time duration	$300fs$	$300fs$	$600fs$

Table 6.1: Grid parameters for the laser input, laser output, and PIC grids.

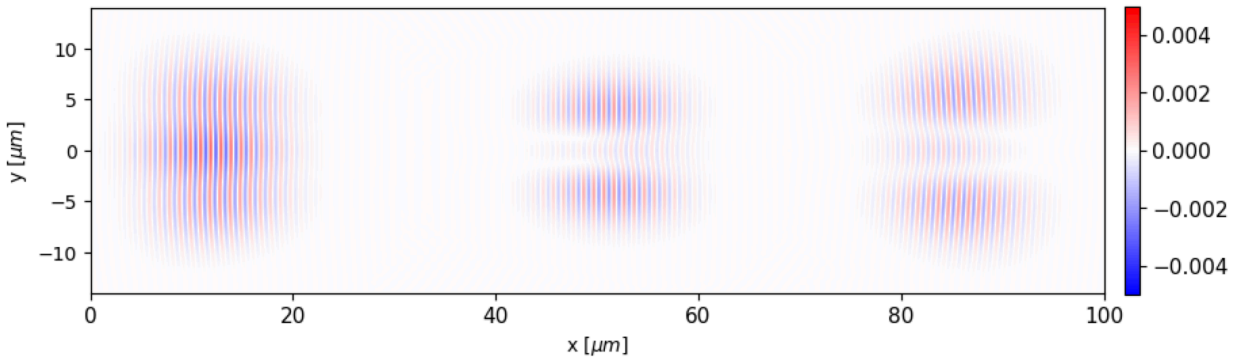

Figure 6.1: The absolute difference in electric field between the approximate form of a Gaussian using Fourier propagation and the built-in analytic Gaussian beam, both with the peak electric field normalized to 1. The fields are shown at three time steps throughout the simulation, 116.7 fs, 250.13 fs, and 366.9 fs

absolute difference between the two fields at three different locations, $x = 14\mu m$, $x = 50\mu m$, and $x = 86\mu m$ are shown. The maximum absolute difference between the two cases is less than 0.0035. The fields are not exactly symmetric about the focus due to errors that accumulate during the propagation in the PIC simulation.

The absolute error between the full, non-approximated Fourier propagated pulse, which captures the polychromatic nature of the pulse, is also evaluated in Fig. 6.2. There is a

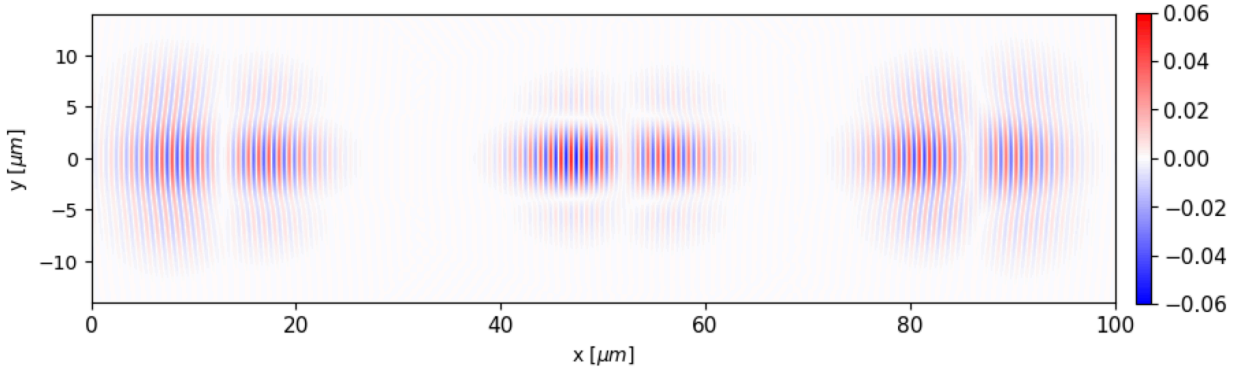

Figure 6.2: The absolute difference in electric field between the non-approximate form of a Gaussian using Fourier propagation and the built-in analytic Gaussian beam, both with the peak electric field normalized to 1. The fields are shown at three time steps throughout the simulation, 116.7 fs, 250.13 fs, and 366.9 fs

much more significant difference between the two pulses, as the full calculation starts to

deviate from the approximation that is natively used in SMILEI. The absolute difference between the two fields is 0.06, an order of magnitude increase from the previously modeled Fourier propagated pulse. This begins to illuminate that the approximate field is not quite accurate when ultrashort pulses are considered. One of the primary differences is that the non-approximate field focuses each frequency component to a different spot size. Typically, the Rayleigh range and spot size are treated as a constant value with the analytic formalism. In reality, both of these terms depend on the wavelength of light that is being focused.

One outcome of this is that there is a radially dependent frequency chirp at the focus of a realistically focused laser pulse, where the focal spot becomes red-shifted further from the propagation axis. This effect is shown in Fig. 6.3, where the instantaneous frequency is plot-

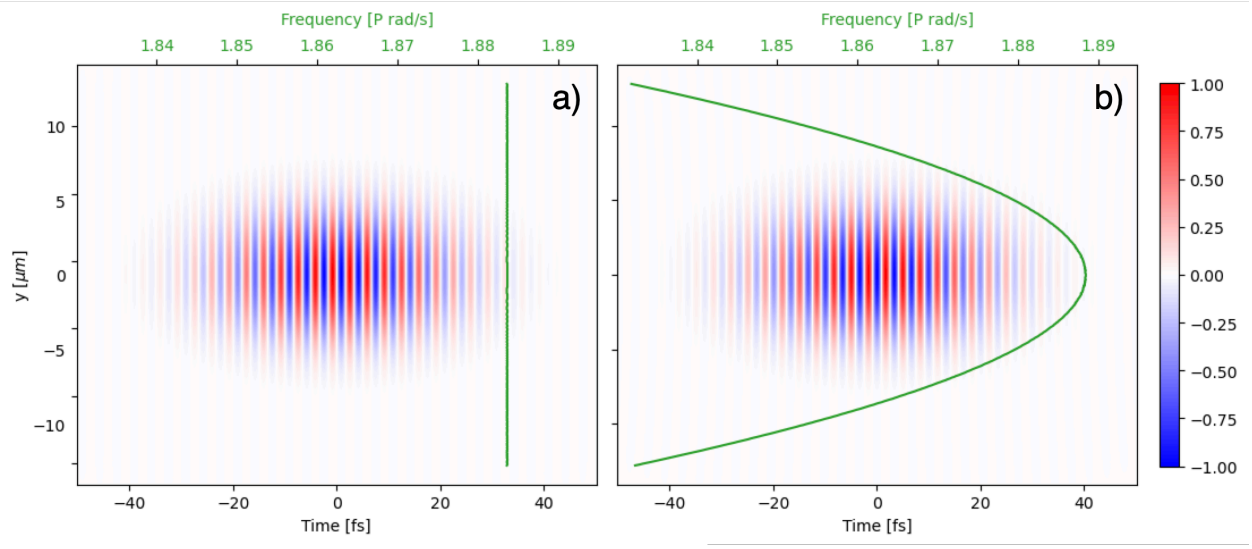

Figure 6.3: The normalized electric fields are shown at the focus for the a) approximate form of Gaussian beam propagation used in SMILEI, and the b) full-calculation using the Fourier code. The instantaneous frequency is overlaid illustrating the shift in center frequency across the transverse dimension for the non-approximate propagation.

ted over the electric field at the focus for pulses focused with and without the monochromatic assumption. In both cases, the electric field profiles look identical, but the spectrum across the transverse dimension significantly varies for the non-approximate field propagation. In Fig. 6.3a, the center frequency across the transverse (y) dimension remains constant. In Fig.

6.3b, the center frequency on-axis (at $y = 0$) is slightly blue-shifted, and becomes increasingly red-shifted radially away from the center axis. This effect originates from the smaller focal spot sizes of lower wavelengths at the focus and their relative intensity compared to the larger, higher wavelength spot sizes.

To further validate the accurate propagation of the Gaussian profile, a comparison of the laser-matter interaction of the two pulses with a hydrogen foil are simulated. Using the same PIC parameters in Table. 6.1, both beams are focused onto a 800 nm thick hydrogen foil that is placed 8.5 μm from the left simulation window. The lasers were modeled as 25 J, 25 fs PW laser pulse, focused down to a 4 μm, $1/e^2$ spot radius on the foil. The foil had a proton and electron density of $30n_c$, modeled with 16 particles per cell. The PIC simulation was done in 3D. The interaction geometry is shown in Fig. 6.4, where the simulation snapshot is shown at 66.75 fs, right before the pulse interacts with the foil. To compare the results of the PIC

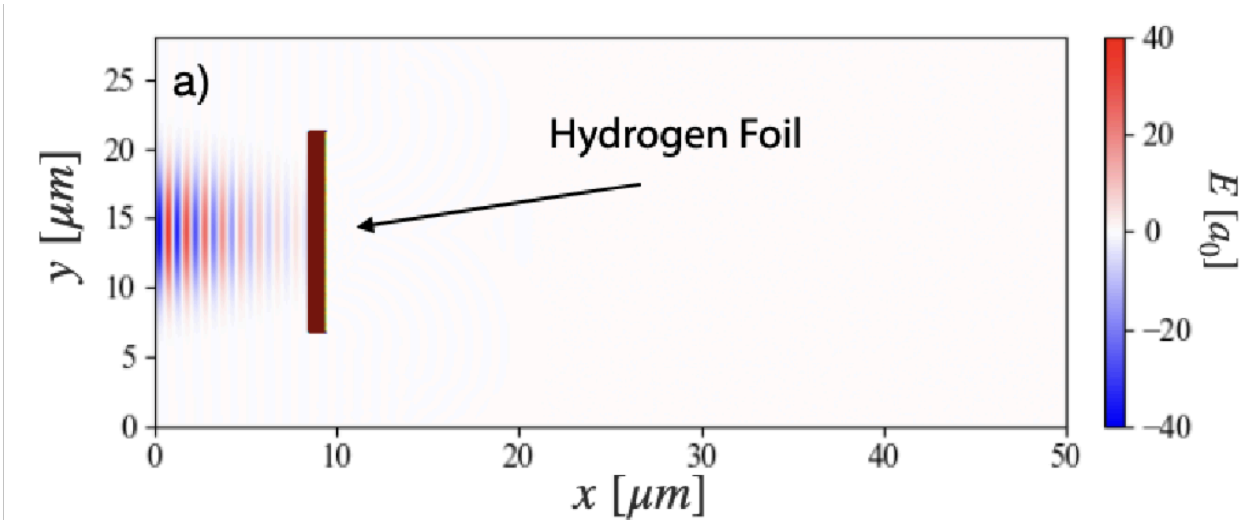

Figure 6.4: The PIC simulation window showing the foil orientation and Gaussian pulse incident from the left window.

simulation, the energy density from both cases is shown in Fig. 6.5. The energy density is taken at $t = 383.64$ fs. The analytic pulse has a peak proton energy of 173.94 MeV and the monochromatic pulse has a peak proton energy of 174.05 MeV, which is a percent error of 0.063% compared to the built-in Gaussian. This again is in quite good agreement, giving

confidence in the Fourier propagation technique accurately modeling the pulse propagation from the lens to the PIC simulation window. From these simulations, the Fourier propagated

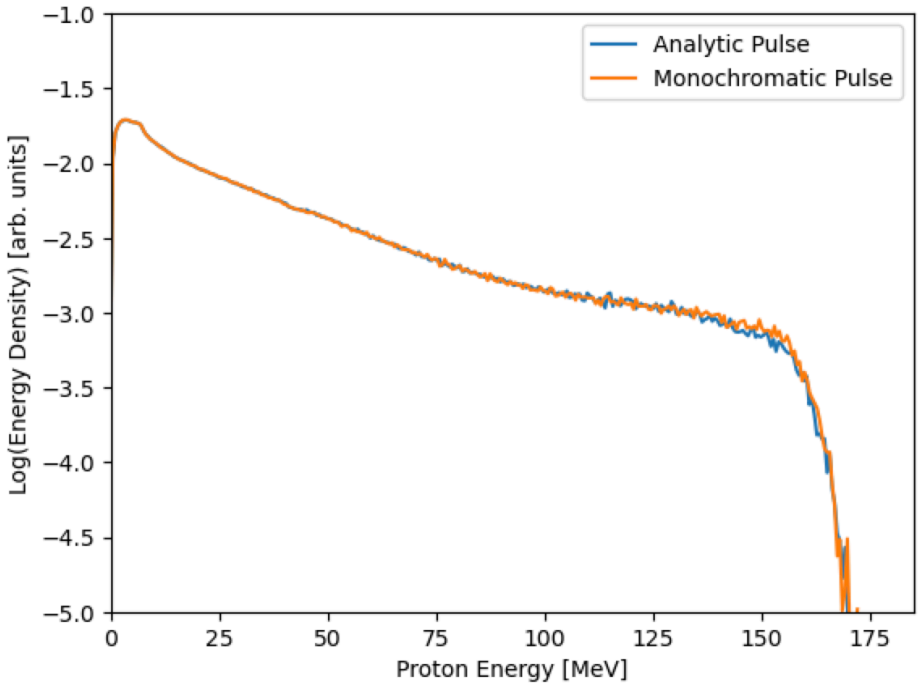

Figure 6.5: The energy spectrum of the Fourier propagated Gaussian with monochromatic approximations compared to the analytic Gaussian pulse. The peak energy for the monochromatic pulse is 174.05 MeV, and 173.94 MeV for the analytic pulse.

pulse matches the built-in analytic Gaussian beam, as long as the same assumptions are made on the field in the Fourier propagation portion. Once those assumptions are taken out, the field starts to diverge from the analytic expression. This is not from any introduced error, but due to being a more accurate model of the diffractive propagation effects of a short pulse. By using this front-end, the laser field evolves differently during propagation, and the field is different than what is normally assumed in Smilei. These properties necessarily change the dynamics of a laser-matter interaction, so having a more accurate description of the field is crucial for modeling.

6.3 PIC simulations

6.3.1 Accurate Modeling of Gaussian Beams

With the ability to accurately model the Gaussian beam in a PIC simulation, the first order-of-matter is to look at how this description of a Gaussian beam changes the laser-matter interaction. To look at this, the same interaction geometry and simulation parameters of Fig. 6.5 are used. The same pulse is modeled, but the monochromatic approximations are removed from the code. The energy density of the full diffractive propagation is compared to the analytic solution in Fig. 6.6. The polychromatic pulse interacting with the foil

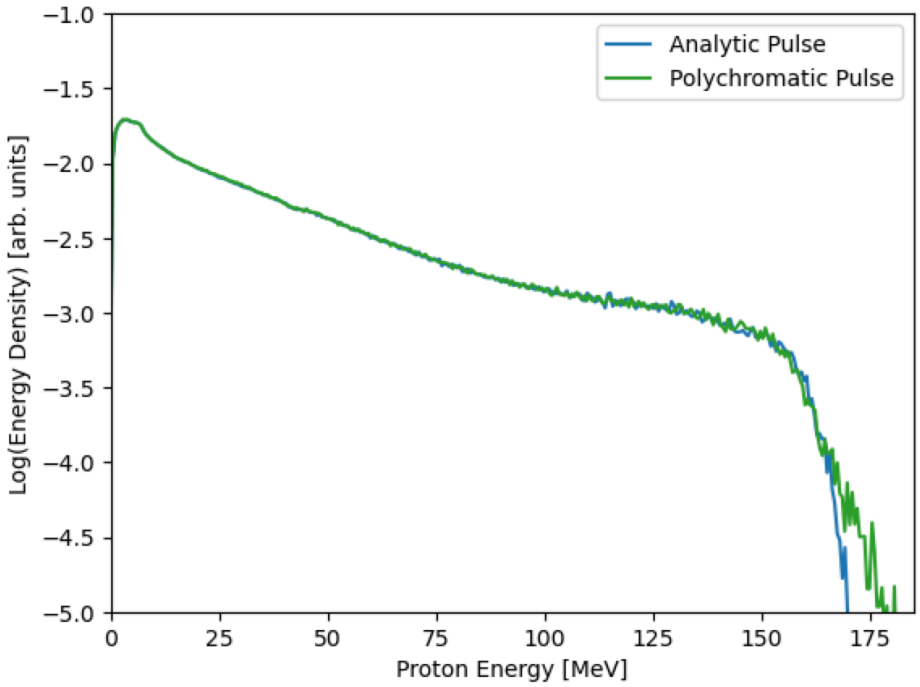

Figure 6.6: The energy spectrum of the Fourier propagated Gaussian with no approximations compared to the analytic Gaussian pulse. The peak energy for the non-approximated pulse is 184.37 MeV, and 173.94 MeV for the analytic pulse.

results in a peak proton energy of 184.37 MeV, a 6% increase over the analytic propagation. This difference, while seemingly small, is indicative that accurate modeling of the laser propagation results in a difference in proton acceleration. Only one particular case is looked

at here, and the effect on different foil thicknesses, varying angles, different foil materials, among other parameters was not studied.

6.3.2 1D Spatially Chirped Beams

Next are simulations detailing how SSTF beams interact with with a foil and how the PFT affects the proton acceleration. To do this, simulations were run with laser parameters summarized in Table 6.2 and PIC simulation parameters summarized in Table 6.3.

Laser Parameters	Values
Energy	50 J
Spot Size	6 μm
Pulse Duration	25 fs
Center Wavelength	1 μm
Polarization	s-polarization

Table 6.2: Laser parameters for the 1D focused spatial chirp simulations.

Simulation Parameters	Values
Foil Thickness	800 nm
Time Duration	700 fs
Simulation Window (x x y)	72 $\mu m \times 56$ μm
Simulation Resolution (dx x dy x dt)	20 $nm \times 20$ $nm \times 0.045$ fs
Particles per Cell (PPC)	128

Table 6.3: PIC parameters for the 1D focused spatial chirp simulations.

2D simulations were carried out, with the polarization of the pulse out of the plane of the simulation (s-polarization). This is done to more accurately model the electron heating with the reduced spatial dimensionality [98]. First simulated was how changing the PFT effects the distribution of accelerated protons. In the following simulations, the PFT is varied through changing the amount of spatial chirp from the modeled grating pair. The interaction geometry for various PFTs is shown in Fig. 6.7a-c for 0^o, 45^o, and 60^o, respectively. The spatial chirp is modified through changing the grating separation, and gratings of 1480 lines/mm at an angle of incidence, $\theta_{AOI} = 52.8^o$ were used to generate the spatial chirp. One

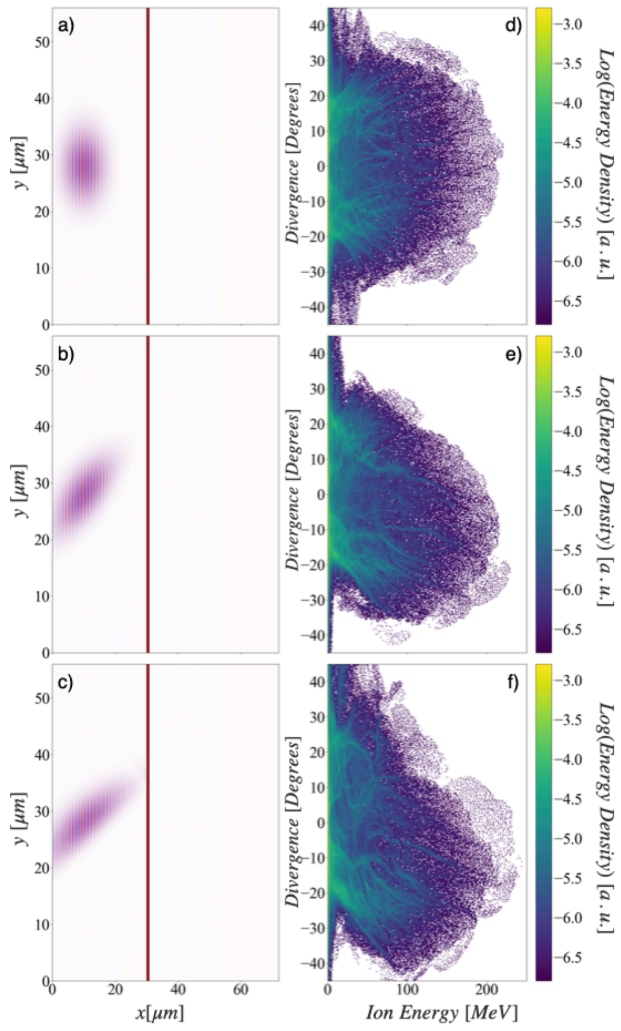

Figure 6.7: PIC simulation results three different values of PFT: 0^o, 45^o, and 60^o. The interaction geometry at $t = 236.8\ fs$ is shown for a)-c) 0^o, 45^o, and 60^o, respectively. The energy divergence plots are shown for d)-f) 0^o, 45^o, and 60^o, respectively

of the properties of the PFT interacting with the hydrogen foil is that there is a steering effect, where the protons get preferentially accelerated towards the perpendicular direction of the PFT. This can be seen in Fig. 6.7 for three different PFT angles of 0^o, 45^o, and 60^o, where 0^o chirp is a regular Gaussian. As the PFT angle increases, the protons get accelerated further away from the propagation axis. An off-axis Gaussian beam also steers protons preferentially towards the normal of the pulse front (which is along the propagation direction, in this case). The main difference is that the off-axis Gaussian has a larger projected spot

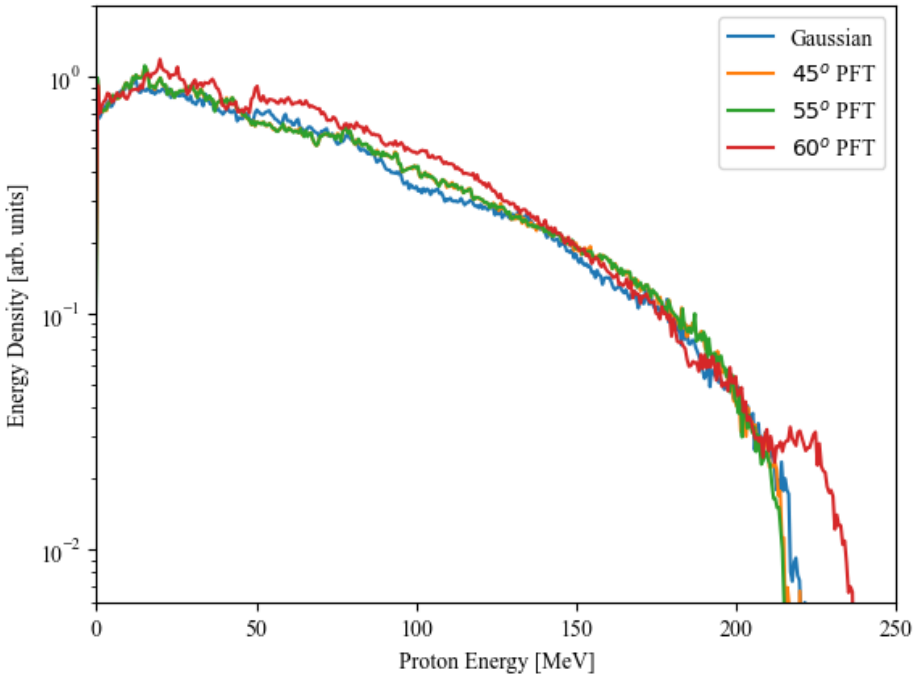

Figure 6.8: The energy density of four different PFT angles: Gaussian (0°), 45°, 55°, 60°.

size that is proportional to $w_0/\cos\theta$, where w_0 is the focused spot size, and θ is the tilt angle of the Gaussian. This projection lowers the peak intensity on the foil, while the SSTF focus maintains its diffraction limited spot size and peak intensity. Another property of the SSTF pulse interacting with a foil, is that the energy density of the accelerated protons can be varied. In Fig. 6.8, the energy spectra for four different values of PFT are shown, 0^o (Gaussian), 45^o, 55^o, and 60^o. The 60° PFT results in a larger peak proton energy than the other PFT angles.

Next, the effects from properly modeling the spatial chirp from the single-pass grating pair geometry are explored through the differences in the energy density of the accelerated protons. It was shown in Chapter 4 that there is a strong relationship between the pulse front curvature and the grating arrangement used to generate the chirp, along with a different trend altogether from the widely used linear approximation of spatial chirp. For the simulations, a linear approximation to the spatial chirp from a grating pair that results in a PFT angle of 60^o is compared to two grating arrangements with different AOIs modeled.

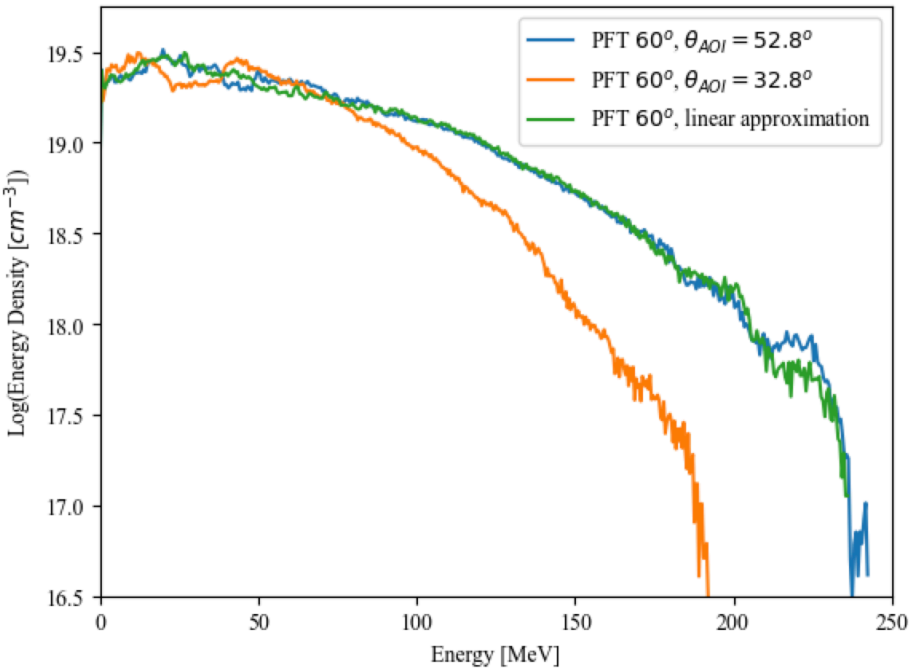

Figure 6.9: The energy density of three focused spatially chirped beams with the same β_{BAR} before focusing. A case of an approximated linear chirp, and spatial chirp generated with a grating pair of $\theta_{AOI} = 52.8^o$ and $\theta_{AOI} = 32.8^o$ are shown.

The same β_{BAR} is generated using a grating pair oriented at 32.8^o and 52.8^o, resulting in different amounts of nonlinearity. These three arrangements are modeled and propagated through the PIC simulation. When considering the accurate spatial chirp distribution from the grating pair, a different proton energy spectrum is observed in Fig. 6.9. The maximum peak energy for the linear chirp approximation was 237.8 MeV. Depending on the AOI used to generate the equivalent chirp, drastically different peak proton energies are observed. The peak proton energies for the $\theta_{AOI} = 52.8^o$ and $\theta_{AOI} = 32.8^o$ are 242.3 MeV and 192.5 MeV, respectively. As a result of properly modeling the spatial chirp from the pulse, there was a significant variation in the peak energy of the accelerated protons depending on grating AOI chosen. The effects of the grating AOI on the divergence of the protons immediately after the foil (at $x = 35\ \mu m$) are shown in Fig. 6.10a. The pulse front curvature from the low AOI grating arrangement deviates the initial distribution of the protons farther from the propagation axis. Additionally, the FWHM of the proton divergence varies depending

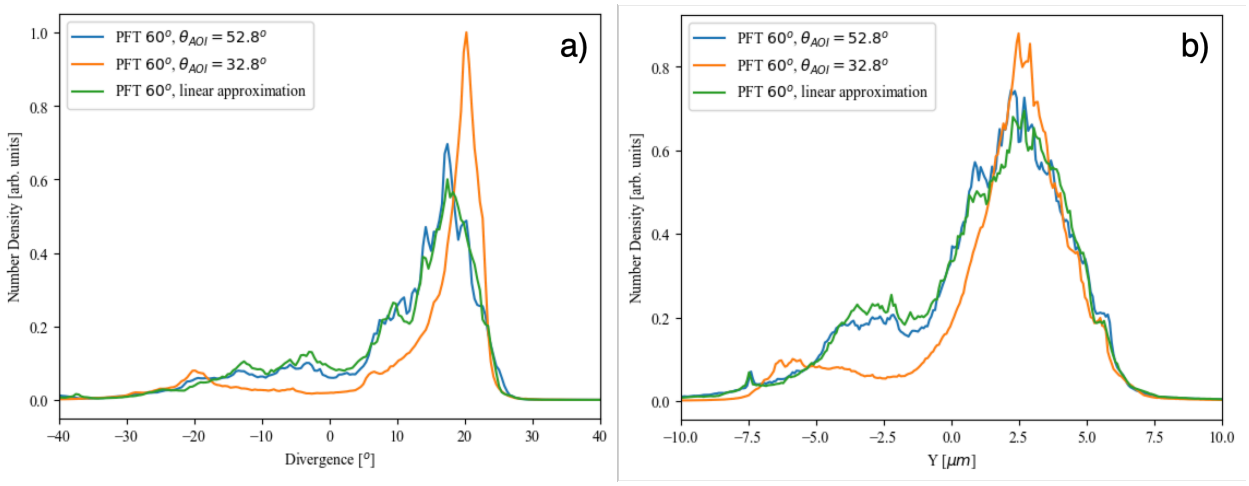

Figure 6.10: The divergence of the $60/circ$ PFT generated with a linear approximation and grating arrangements using $\theta_{AOI} = 32.8°$, and $\theta_{AOI} = 52.8°$. The a) divergence at a screen set at $x = 35\ \mu m$ and b) number density at a screen at $x = 45\ \mu m$ are shown.

on AOI. The high AOI and linear approximations have a divergence that is 1.58 times larger compared to the low AOI grating arrangement. Fig. 6.10b shows the spatial distribution at $x = 45\ \mu m$. The protons accelerated with the PFT generated from the low AOI grating pair manage to propagate to this position while maintaining a more narrow spread compared to the other two cases. These results show that, with careful consideration of the grating orientation used, different properties of the accelerated ions can be tuned. With a lower AOI (more nonlinearity), the protons maintained a lower divergence angle at the cost of a lower peak proton energy.

Other common spatial distributions, such as a super-Gaussian distribution, commonly seen in PW lasers, can also be propagated. These fields are hard to describe analytically, as the Fourier transform does not have an analytic solution. In the case of an ideal flat top beam, the Fourier transform is a Sinc function, but typically, flat top beams follow the form of a high-order super-gaussian distribution. An $8th$ order super-gaussian with the same input spot size and normalized to the same parameters as Table 6.2 is considered. Upon interacting with the foil, the energy density (Fig. 6.11) is quite different than that of a Gaussian pulse (Fig. 6.6), due to a lower intensity and the introduction of side lobes at the focus.

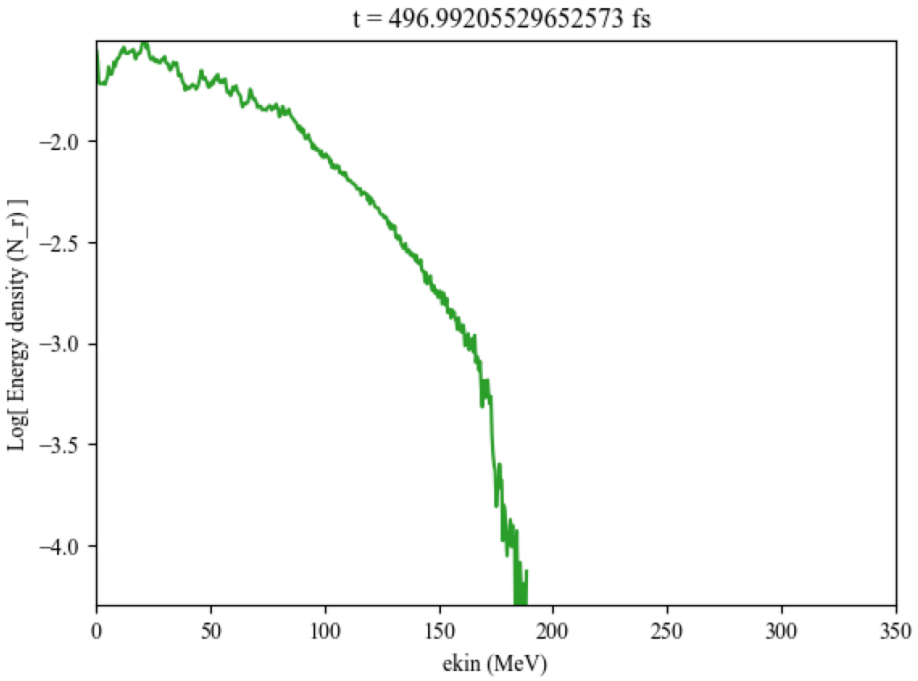

Figure 6.11: The energy density of a Fourier propagated $8th$ order super-gaussian with a 60^o PFT, normalized to the same parameters in Table 6.2. The spatial chirp was generated with a grating AOI of 52.8° and 1480 lines/mm.

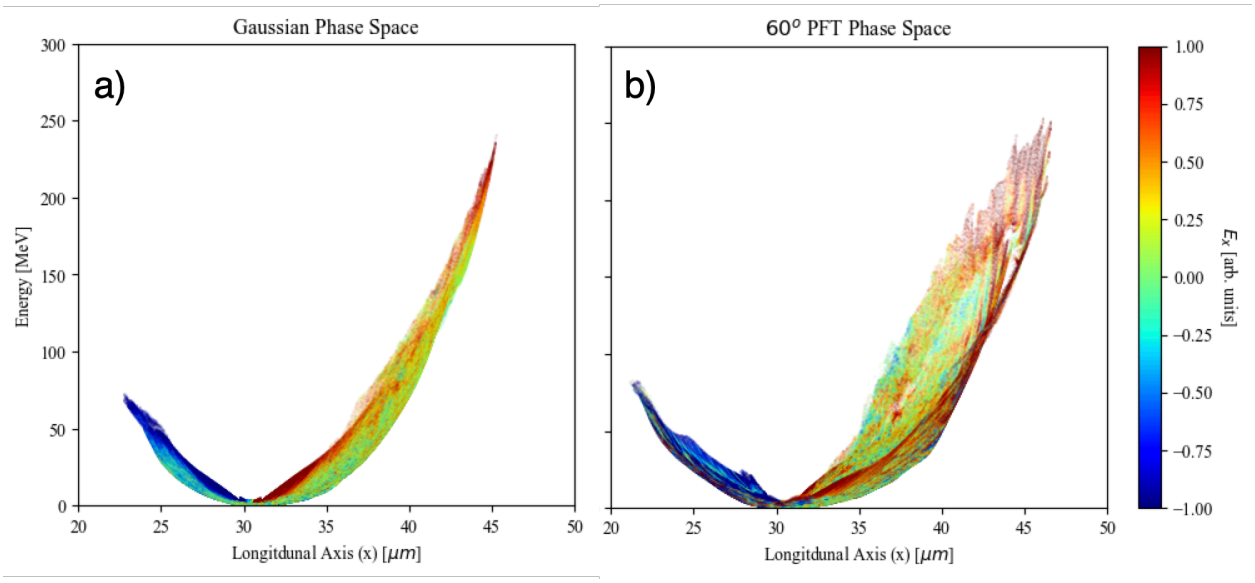

Figure 6.12: The energy-position phase space diagrams for a) a Gaussian pulse and b) a 60^o PFT spatially chirped pulse using parameters from Table 6.2. The color bar scale indicates the normalized longitudinal electric field the macroparticles experience in a particular position in the phase space.

Another way to visualize the difference in proton acceleration for the SSTF beams is with energy-position phase space diagrams. The phase space plots for PFT angles of 0^o and 60^o generated with $\theta_{AOI} = 52.8^o$ are shown in Fig. 6.12. In the 60^o PFT case, the phase space starts to expand upwards, indicating that the protons are reaching higher energies for a given longitudinal position.

6.3.3 2D Spatially Chirped Beams

The ability of the PFT to steer the protons enables the ability to have a symmetric variation that steers the protons towards the propagation axis, enhancing collimation and propagation distance.

6.3.4 Radial Chirp

First, the symmetric, radial chirp generated from the output the the single-pass concentric ring grating pair in Chapter 5 is studied. The case of symmetric chirp of Fig. 5.1c is considered, where the blue portion of the beam is on the outside edge. In this arrangement, the pulse front structure as the beam focuses is an open cone, which gives the proper orientation so that the PFT steers the accelerated protons towards the propagation axis. In the opposite orientation, with red on the outside, the PFT is oriented in such a way that it would force the protons away from the propagation axis. The PFT needs to be correctly chosen so that enough of the protons get propelled on-axis. Too little of a PFT, and they will have too much forward momentum, too much PFT and they will have too much transverse momentum and pass through the propagation axis. Additionally, if the pulse is focused directly on the foil, the pulse front doesn't maintain a large conical structure, and not enough protons will get accelerated. The symmetric chirp has many parameters that tune the effective PFT seen by the foil: δr, β_{BAR}, and the distance from the focus.

A Bayesian optimization routine is used in order to approach a set of parameters that gives a good confinement of protons on axis. 3D PIC simulations are used to capture the full shape of the axisymmetric beam profile. The 3D PIC simulations used are extremely resource hungry and doing a grid search of parameters is a time-consuming endeavor. The Bayesian routine was used as it gives a fairly good result, relatively quickly. The laser parameters used in the Bayesian scan that are held constant are shown in Table 6.4. The parameters that are allowed to vary in the Bayesian scan and example values are shown in Table 6.5.

Parameters	Values
Energy	25 J
Input Beam Size (w_{in})	7.5 cm
Spot Size	4 μm
Pulse Duration	25 fs
Center Wavelength	1 μm
Polarization	Radial

Table 6.4: Laser and simulation parameters for the 3D simulation of radial chirp.

Laser Parameters	Values
δr	$3w_{in}$
Distance from Focus	36 μm
Grating Separation (60° PFT)	42.5 cm

Table 6.5: Laser parameters for the the 3D simulations that are varied during Bayesian optimization and example values.

The interaction geometry for the following simulations is shown in Fig. 6.13, where the beam comes in from the left side of the PIC simulation and interacts with the hydrogen foil placed 8.5 μm from the left side of the simulation. The simulations were initially run at low resolution (dx x dy x dz x dt = 62.5 nm x 62.5 nm x 62.5 nm x 0.045 fs and 16 PPC) to help reduce computational resources while doing the Bayesian scan. The main parameter of interest was minimizing the divergence of protons, which enables a high number of protons to propagate to the edge of the PIC simulation window. To achieve this, the metric that was tracked during the Bayesian scan was the energy density that made it through a probe

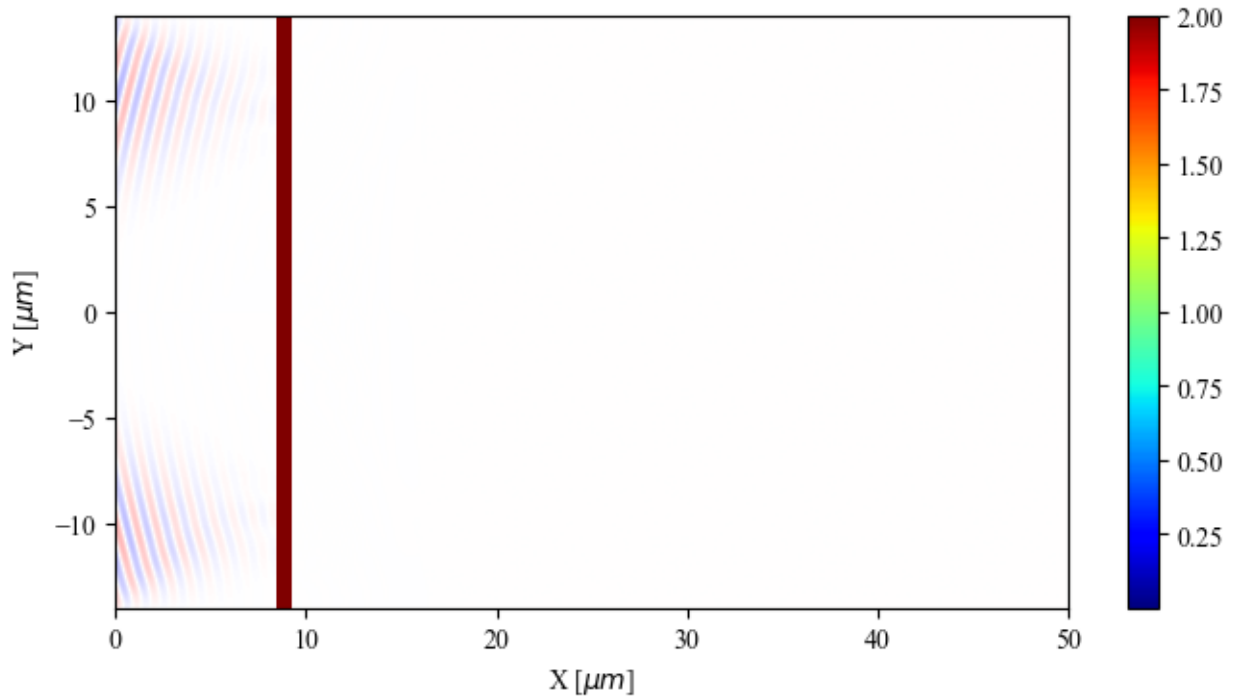

Figure 6.13: The interaction geometry for the 3D radial chirp simulations shown in the y-x plane at z=0. The laser comes in from the left boundary and interacts with a hydrogen foil at 8.5 μm. The color map density corresponds to the density of the protons at a given position.

in the PIC simulation at 40 μm. For the case of comparison, the proton acceleration from a Gaussian beam interacting with the foil in this arrangement is shown in Figs. 6.14 and 6.15. The values of number density that are presented in the following sections are normalized to the values obtained from the Gaussian beam simulation.

The proton jet formation, divergence, and energy density for a variety of varied parameters are shown in shown in Figs. 6.16-6.23. The density plots are shown at $t = 800\ fs$. The side profile of the 3D PIC simulation window at $z = 0$ in the y-x plane, along with a transverse cross-section at $x = 40\ \mu m$ in the y-z plane are depicted for several cases of parameters that were varied. The energy densities are shown at the time that results in the peak recorded proton energy, and the divergence is calculated across the full transverse plane over the entire duration of the simulation. Single parameters were varied while keeping the remaining laser parameters fixed from Table 6.5 to isolate the effect each have on the proton acceleration.

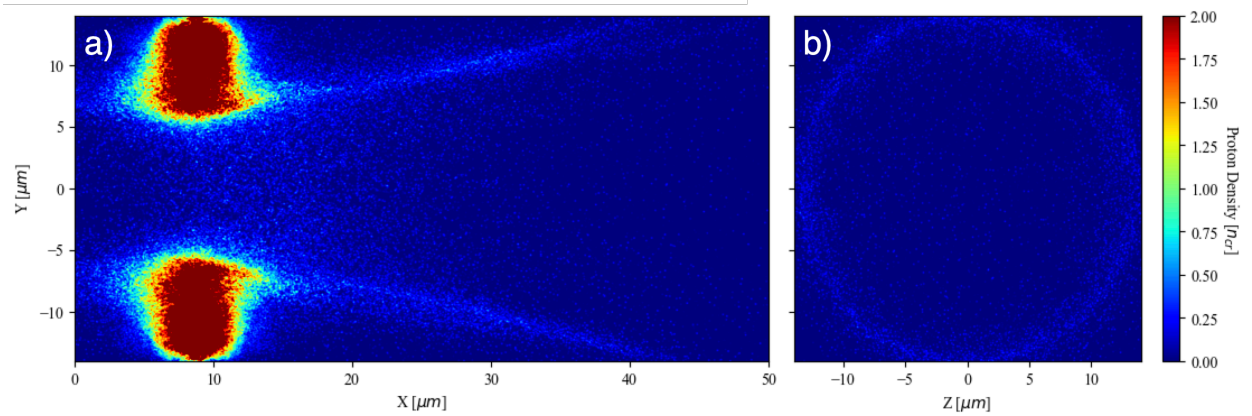

Figure 6.14: The accelerated protons for a Gaussian beam interacting with a hydrogen foil at $t = 800\ fs$. The a) longitudinal profile of the accelerated proton density in the y-x plane at z=0 along with the b) transverse y-z plane at $x = 40\ \mu m$ are visualized.

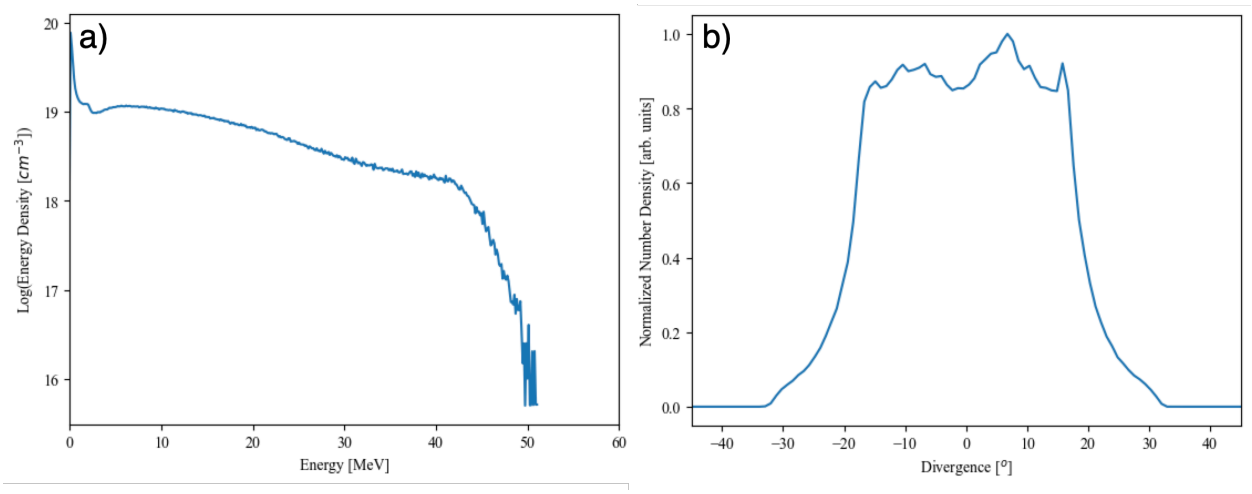

Figure 6.15: The a) maximum energy spectrum at $t = 583.8\ fs$ and the b) divergence angle are shown for the Gaussian beam.

PFT

First, all values in Table 6.5 are kept fixed expect for grating separation which varies the PFT. PFT values of 0^o, 40^o, 60^o, and 70^o were simulated, and the collimated jets are shown in Fig. 6.16. For the case of 70^o PFT, there is an increase in number density along the propagation axis due to the angle of the pulse front maximizing the confinement of particles. The energy density (Fig. 6.17a) did not vary significantly when PFT was changed, in contrast to the results from the previous section where different parameters were used. In this case,

since the pulse hits before the focus, the spot size of the interacting field on the foil is larger and the energy simulated was 25 J. The peak proton energy stays roughly the same across all cases, but the divergence and number density increase with increased PFT. The increasing PFT results in higher density in a smaller transverse spot along the propagation direction, which increases the number density passing 40 μm. The values of collimation and number density that propagates beyond 40 μm is compared in Fig. 6.17c,d. As PFT angle increases the collimation trends towards getting slightly worse while the number density increases.

Foil Thickness

The foil thickness is varied while the rest of the laser parameters from Table 6.5 are kept fixed. Hydrogen foils formed through liquid hydrogen jets have been generated [99, 100] with thicknesses of 1 μm-5 μm, and may be pushed towards smaller thicknesses as the technology develops. The jet formation of the thinnest foil (400 nm) in Fig. 6.18a results in a proton jet that is much faster moving than the other cases. At the same time step, the jet is mostly out of the PIC simulation window and many particles have left the simulation. As the foil thickness is increased, the proton jet slows down. This trend can also be seen in Fig. 6.19a, where the energy density for the thinner foil has a much higher peak energy compared to the thicker foils. The three foil thicknesses all maintain a similar divergence angle. The number density that passes 40 μm varies between the three cases, and is a balance between number of particles in the foil and the speed the protons are accelerated to. The 400 nm foil has half as many particles as the 800 nm foil and so there are less particles to accelerate, lowering the value of the metric shown in Fig. 6.19d. The 800 nm foil has the largest number of protons, but they are accelerated to the slowest speeds. There is a balance between these two competing effects, and the case in between (600 nm) results in the largest number density reaching 40 μm.

Foil Position

Simulations where the foil position is varied are examined, where the varied distance indicates how far the foil is set before the geometric focal length of the lens. All three cases show jet-like structures in Fig. 6.20, with the case of a 31 μm offset (Fig. 6.20c) having a fast moving jet, where a majority of protons have already left the simulation window after 800 fs. Again, this is related to the much higher energy density compared to the other cases in Fig. 6.21a. As the foil gets closer to the focus, the peak intensity that the foil experiences starts to grow, and there is a correlation of higher peak energies for higher a_0 values. Collimation gets slightly better for the foil that is closer to the focus, with the number density metric varying in a similar manner to the previous case of varied foil thickness. The foil distance closer to the focus (31 μm), results in much higher energies, but overall has a lower number of protons that get accelerated. Since it hits closer to the focus, the projected spot size on the foil is smaller, and so a reduced area of protons experience the accelerating effects of the electric field. This can be seen in Fig. 6.20a-c, where Fig. 6.20c has a larger quantity of protons left at the original foil position of 8.5 μm. The foil position set 41 μm away experiences the inverse effect, where the intensity is lower from being farther away from the geometric focus (thus lower peak proton energy) but has a larger spot on the foil. The case in the middle at 31 μm is again a sweet spot, where there is a balance between the two effects of peak a_0 and total number of protons accelerated.

Radius of Radial Chirp (δr)

Varying δr changes the angle of the phase fronts with respect to the propagation axis. Changing this angle changes the size of the radially chirped beam as it propagates towards the focus, and changes the spot size at the focus through increased frequency of interference patterns (see Fig. 5.7). Again, there is a trend that for one particular case, the peak proton

energy is much larger than the others. Fig. 6.22a has much higher energy protons than the other cases simulated, and so the protons have already left the simulation window at this time step. The energy density shown in Fig. 6.23a indicates a drastic increase in proton energy for the $\delta r = 2w_{in}$ case. Since the spacing between the the optical axis and the center wavelength in the radial chirp is smaller, the beam actually propagates with its intensity profile closer to the axis, resulting in a smaller spot and higher intensity as it hits the foil before its focus, leading to higher peak proton energies. The collimation across the cases is relatively constant, with the larger values of δr leading to slightly worse collimation. The number density in Fig. 6.23d shows the highest peak energy resulting in the lowest number density propagating. Again, this is due to the fact that the spot size was smaller on the foil, resulting in a smaller areal density of protons being accelerated, but accelerated more quickly. The other values of δr, $2.75w_{in}$ and $2.9w_{in}$, give similar spot sizes (and intensities), and so do not vary much in energy density or number density.

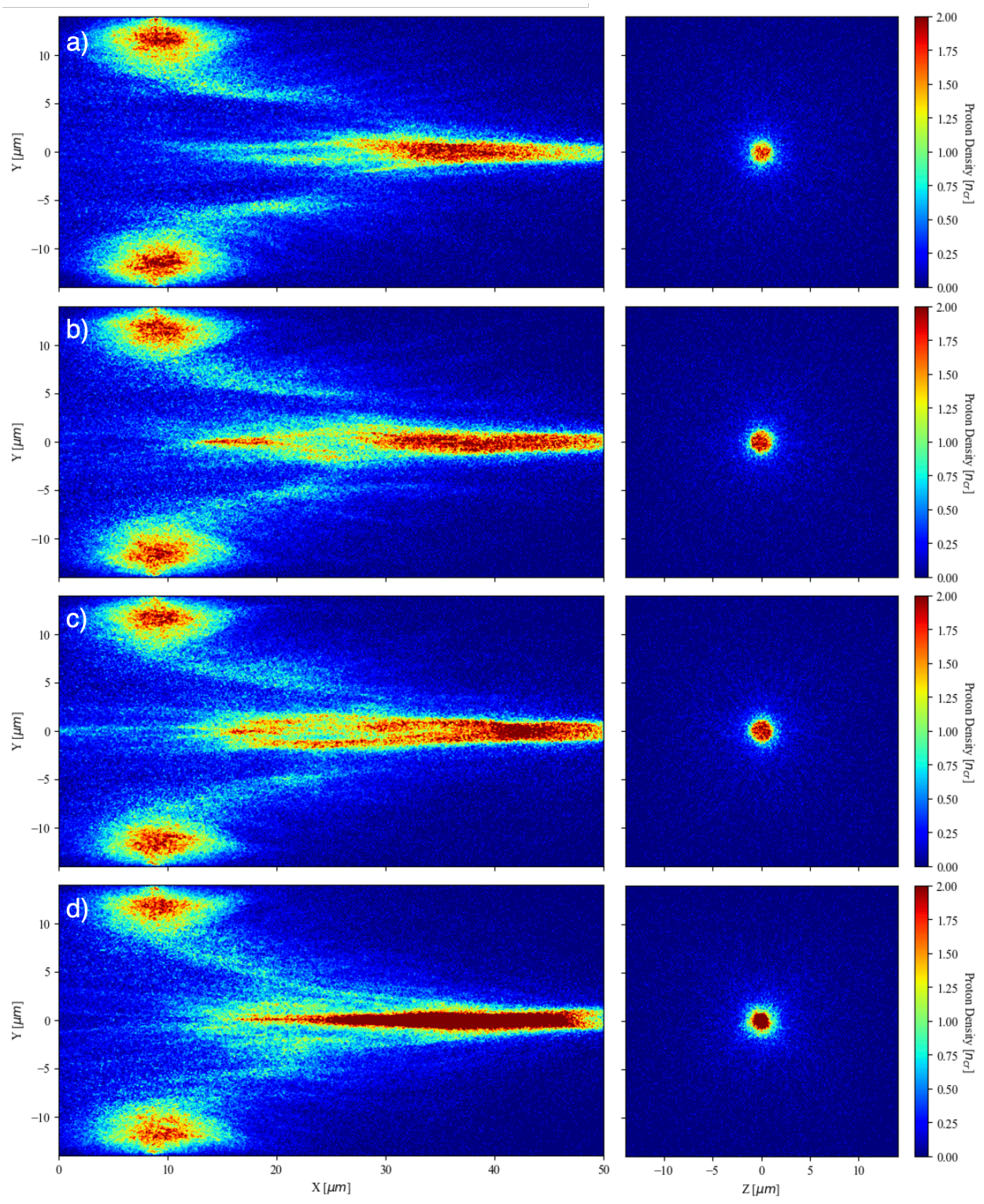

Figure 6.16: The accelerated protons for various radially chirped beams interacting with a hydrogen foil at $t = 800\ fs$. a)-d) are y-x plots at $z = 0$ from PIC simulations where the PFT of the beam is set to 0^o, 40^o, 60^o, and 70^o, respectively. e)-h) are y-z plots of the transverse cross section of the simulation at $x = 40\ \mu m$.

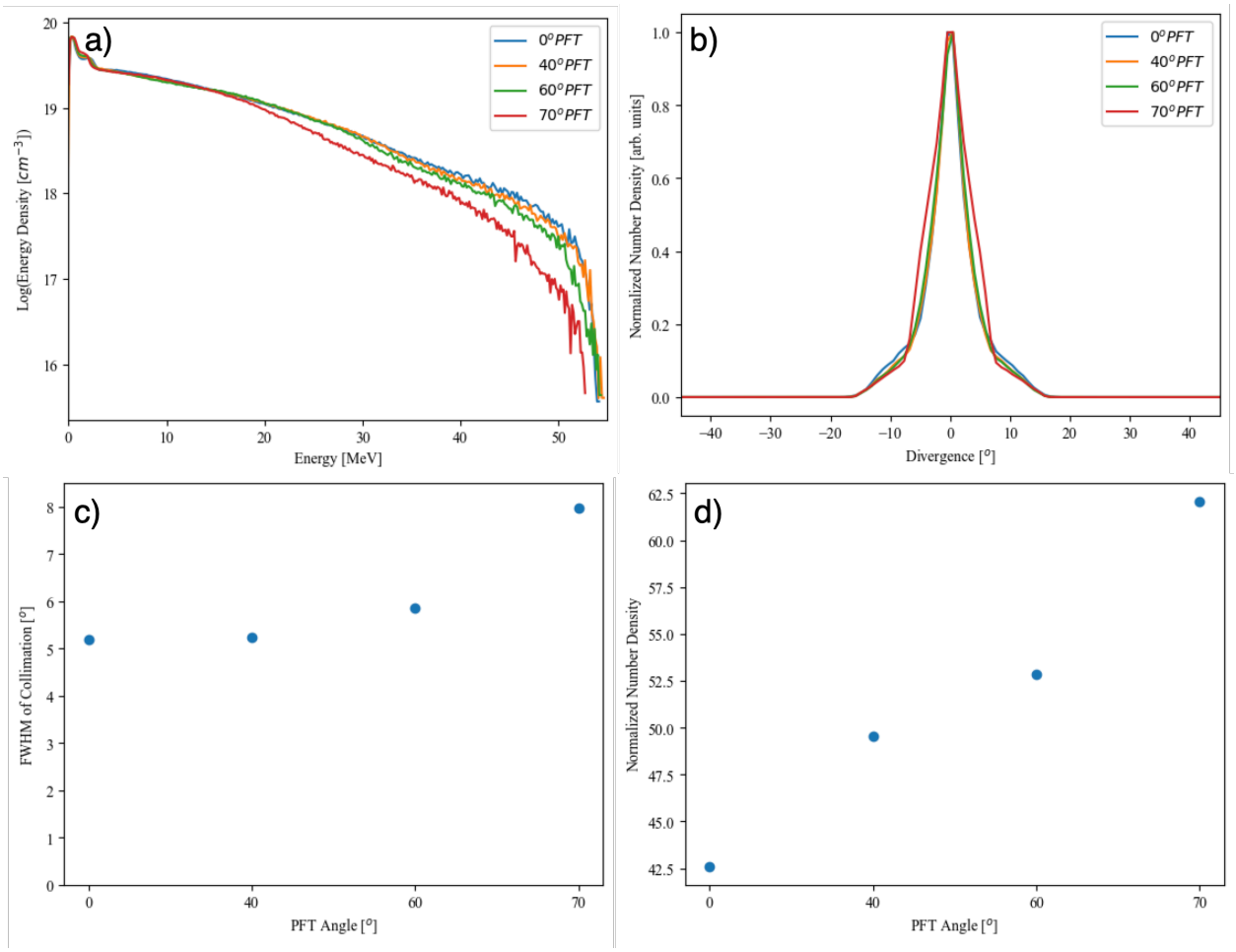

Figure 6.17: The a) energy spectrum at the time of maximum proton energy, b) divergence over the simulation window, c) variation of the FWHM of divergence, and d) total number density of protons at $40\mu m$ is compared for four different angles of PFT: 0^o, 40^o, 60^o, and 70^o.

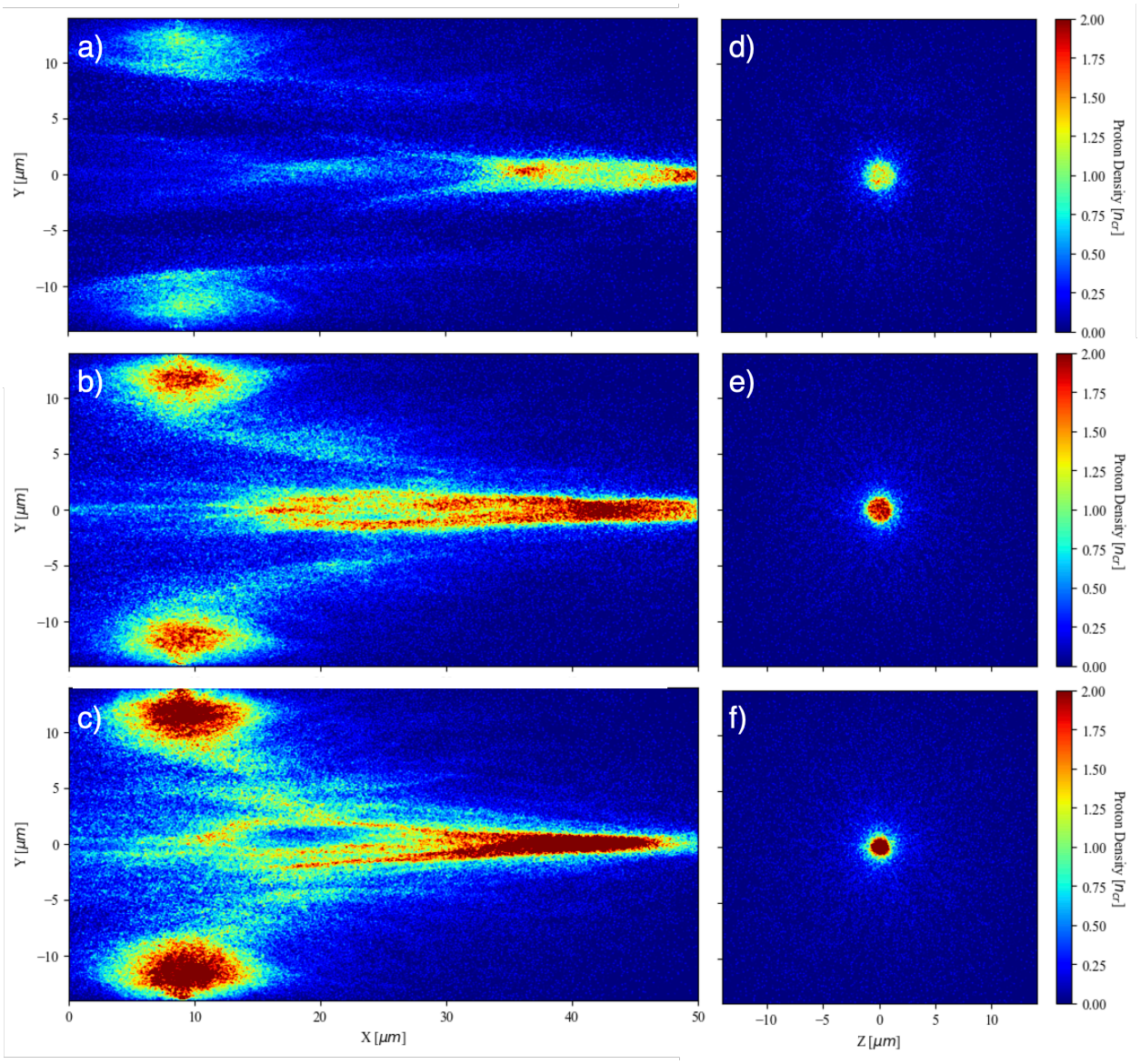

Figure 6.18: The accelerated protons for various radially chirped beams interacting with a hydrogen foil at $t = 800\ fs$. a)-c) are y-x plots at $z = 0$ from PIC simulations where the foil thickness is varied from 400 nm, 600 nm, and 800 nm, respectively. d)-f) are y-z plots of the transverse cross section of the simulation at $x = 40\ \mu m$.

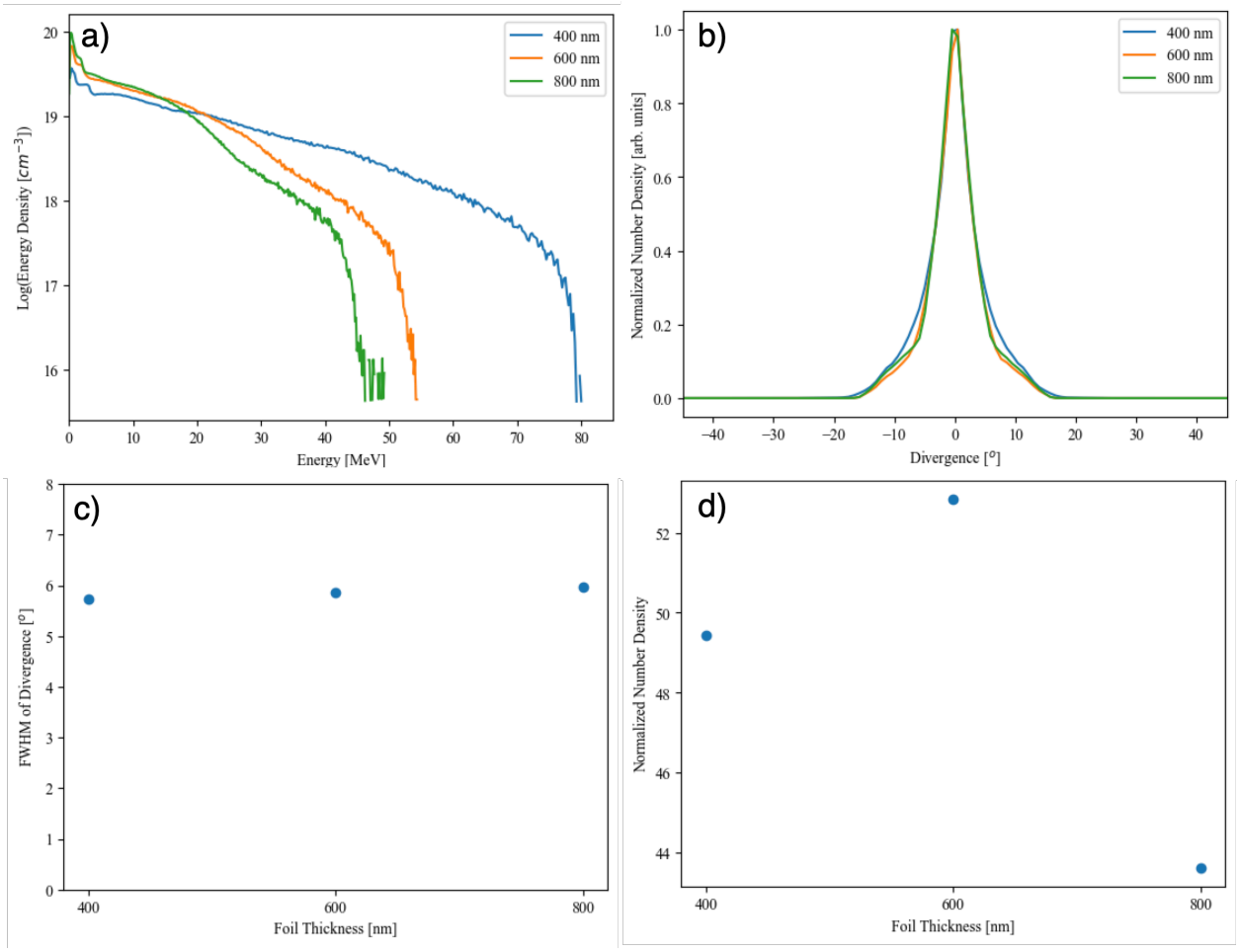

Figure 6.19: The a) energy spectrum at the time of maximum proton energy, b) divergence over the simulation window, c) variation of the FWHM of divergence , and d) total number density of protons at $40\mu m$ is compared for three different foil thicknesses: 400 nm, 600 nm, and 800 nm.

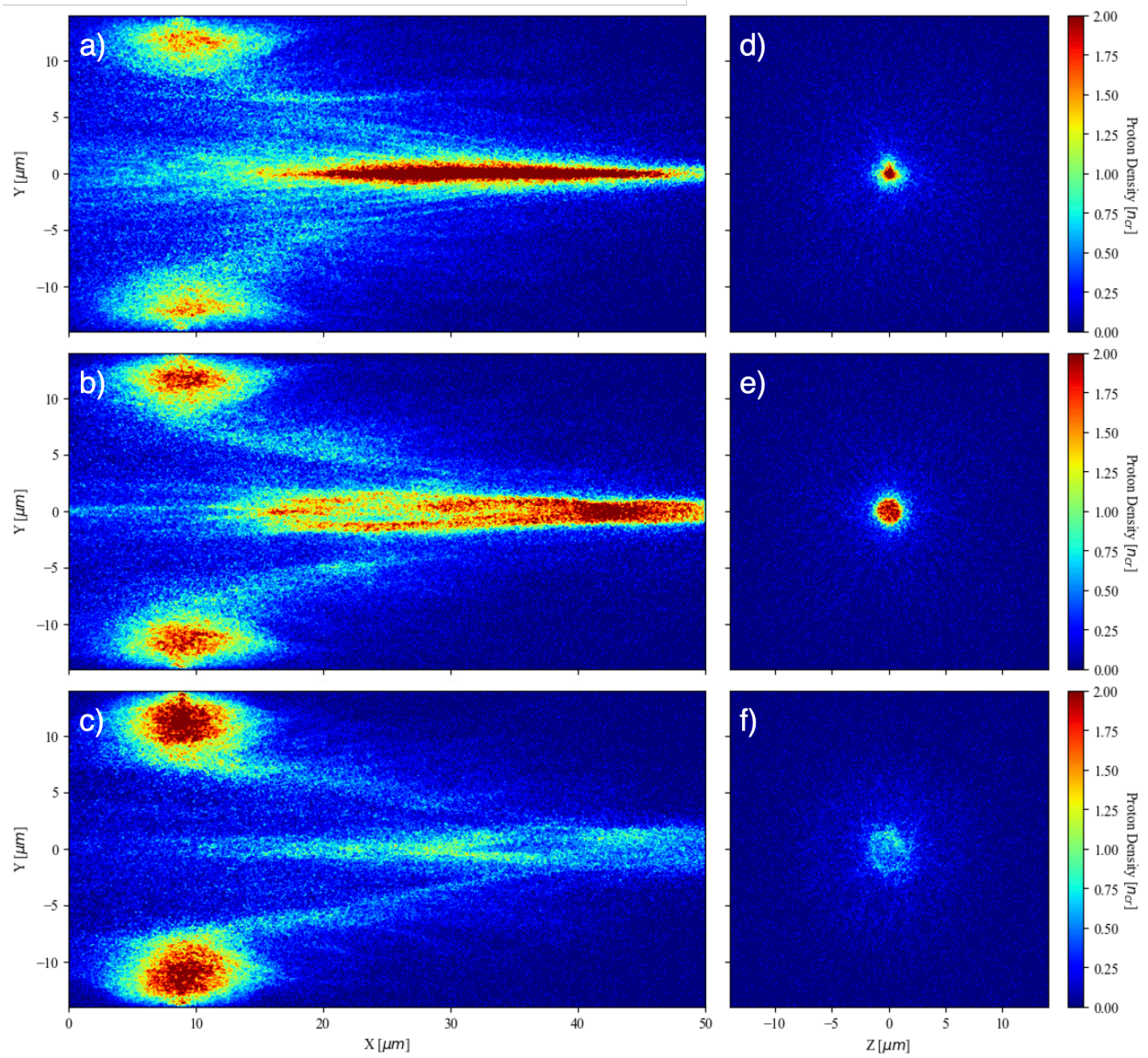

Figure 6.20: The accelerated protons for various radially chirped beams interacting with a hydrogen foil at $t = 800\ fs$. a)-c) are y-x plots at $z = 0$ from PIC simulations where the foil position in front of the focus is varied from 41 μm, 36 μm, and 31 μm, respectively. e)-h) are y-z plots of the transverse cross section of the simulation at $x = 40\ \mu m$.

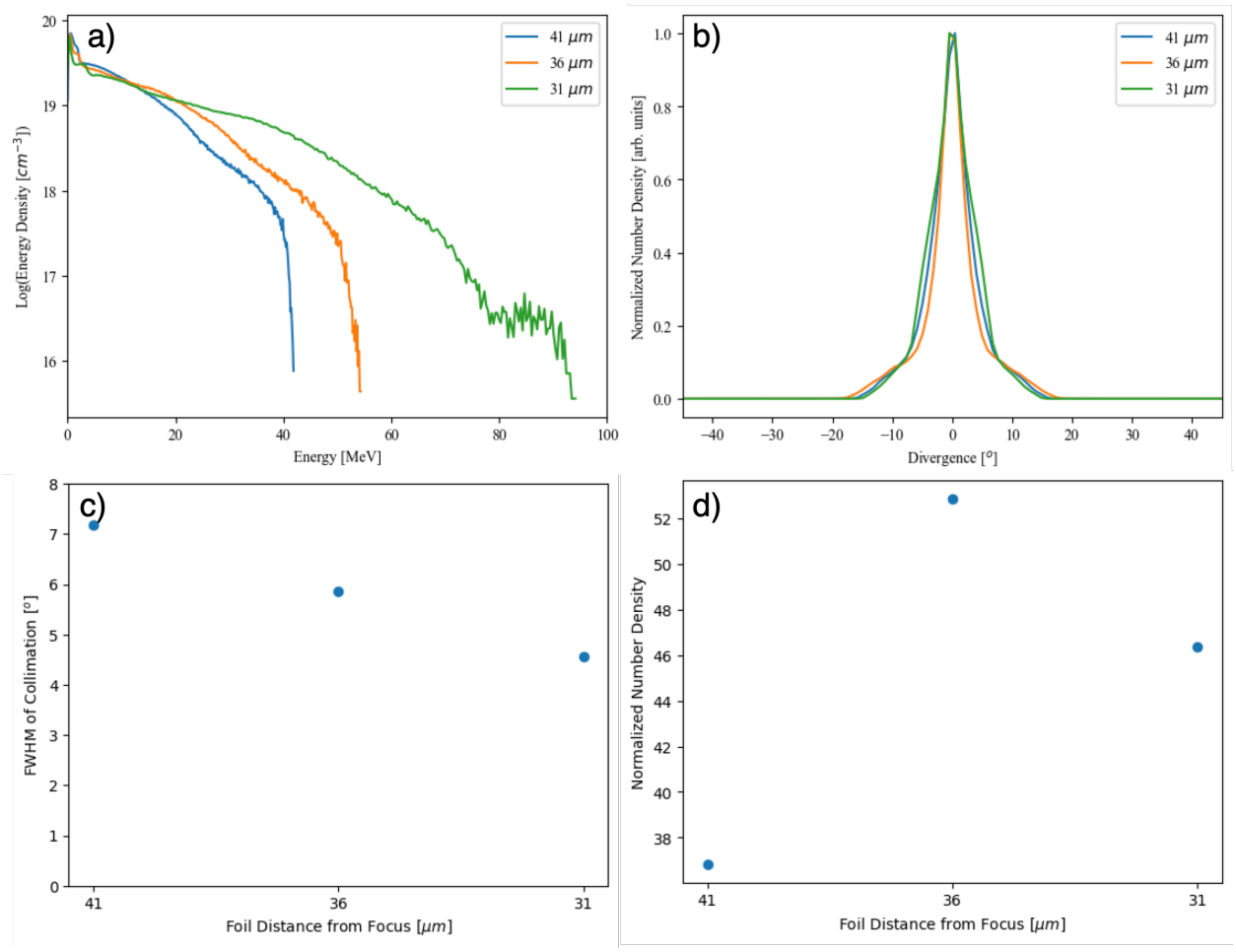

Figure 6.21: The a) energy spectrum at the time of maximum proton energy, b) divergence over the simulation window, c) variation of the FWHM of divergence , and d) total number density of protons at $40\mu m$ is compared for three different foil positions from the focus: 41 μm, 36 μm, and 31 μm.

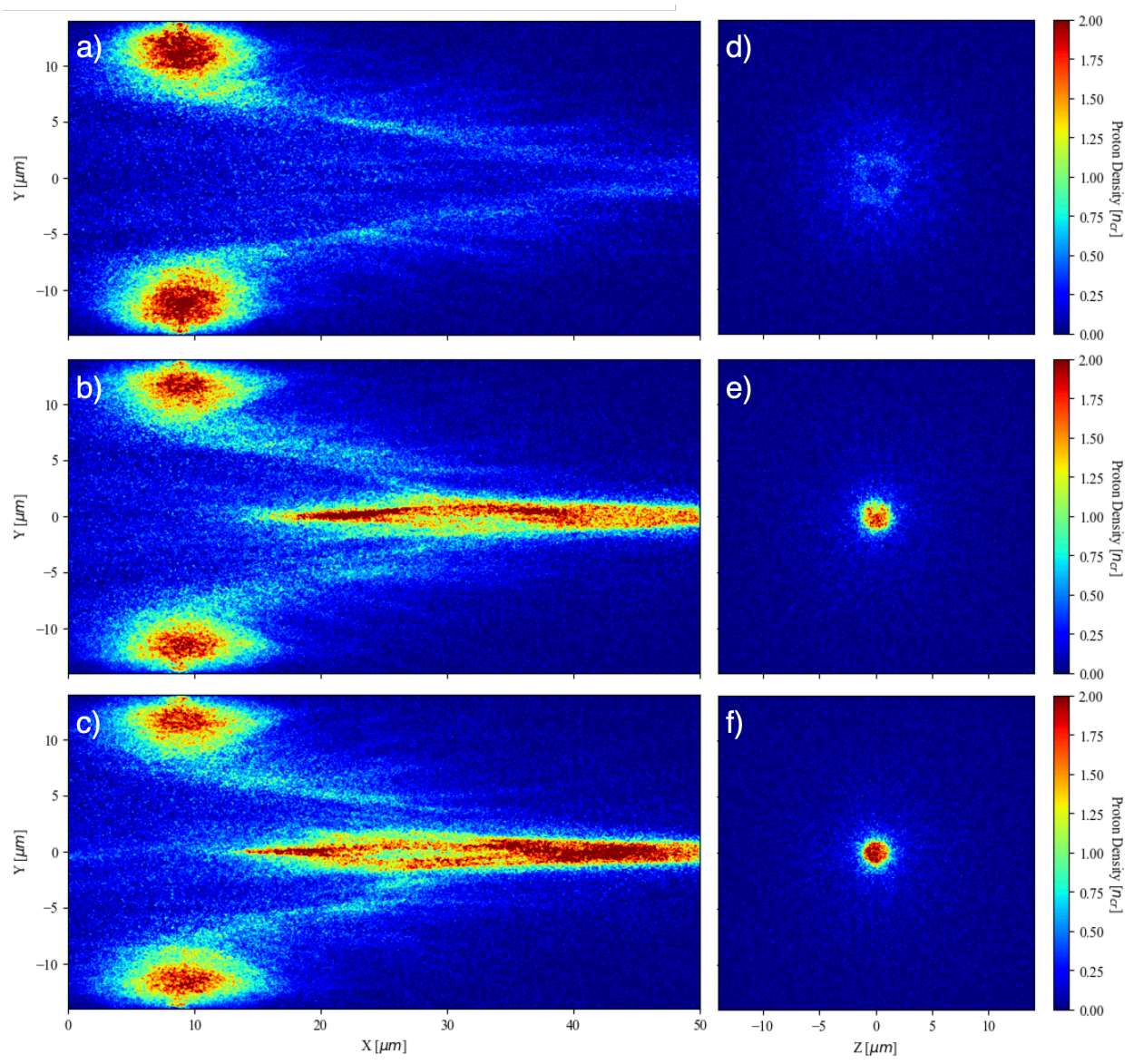

Figure 6.22: The accelerated protons for various radially chirped beams interacting with a hydrogen foil at $t = 800\ fs$. a)-c) are y-x plots at $z = 0$ from PIC simulations where the distance of the center frequency to the propagation axis, δr, is varied from $2w_{in}$, $2.75w_{in}$, and $2.9w_{in}$, respectively. e)-h) are y-z plots of the transverse cross section of the simulation at $x = 40\ \mu m$.

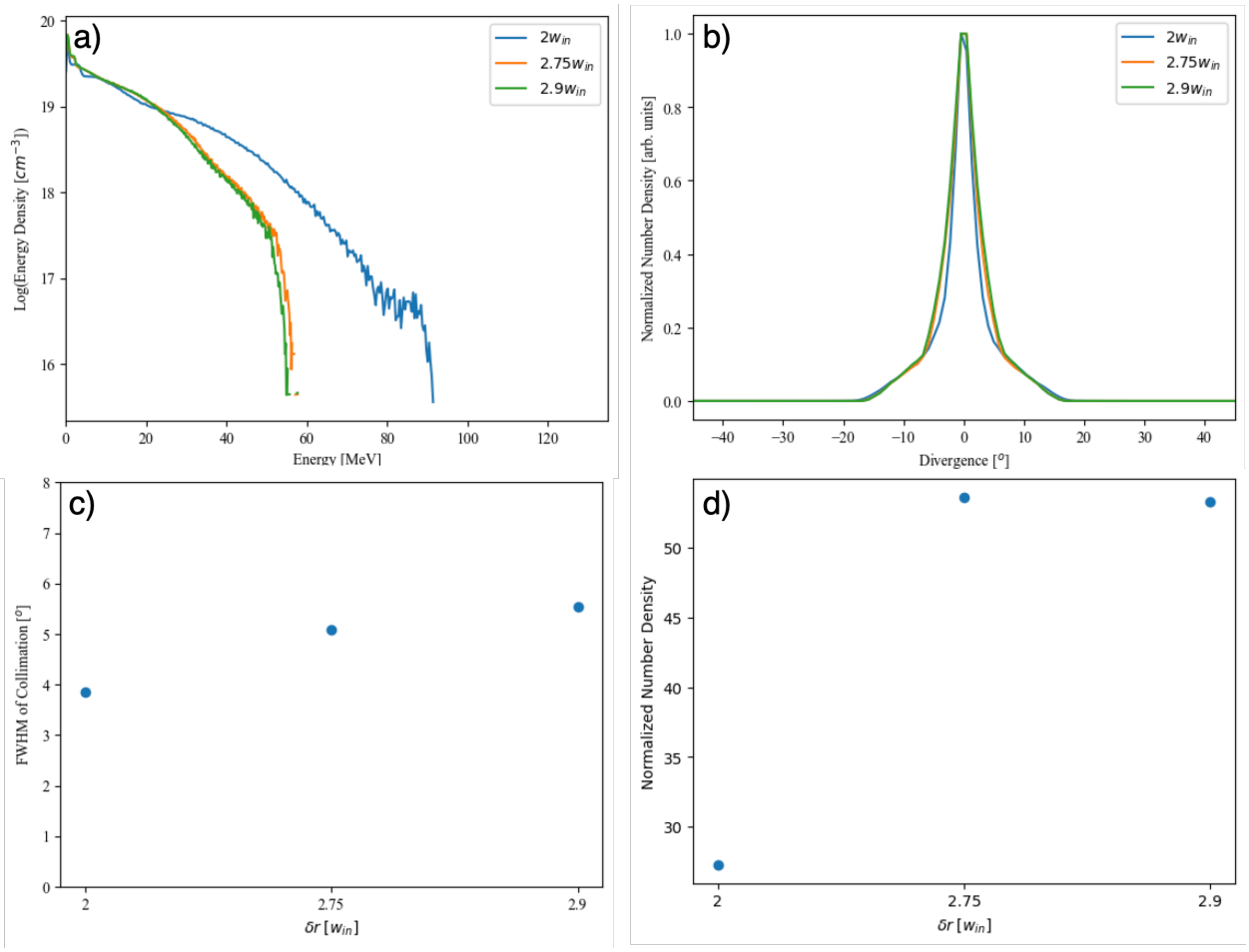

Figure 6.23: The a) energy spectrum at the time of maximum proton energy, b) divergence over the simulation window, c) variation of the FWHM of divergence , and d) total number density of protons at $40\mu m$ is compared for three different values of δr: $2w_{in}$, $2.75w_{in}$, and $2.9w_{in}$.

The collimating effect originates from the initial acceleration of the protons from the beam steering effects of the PFT when interacting with the foil. At a later time, once a sufficient number density of electrons and protons are along the axis, a collimating magnetic field forms. This field originates from a slight charge separation along the jet, where electrons lead in time after accelerating first from the foil due to their much smaller mass compared to the protons. The magnetic field at $t = 800\ fs$ is shown in Fig. 6.24a. This creates a force

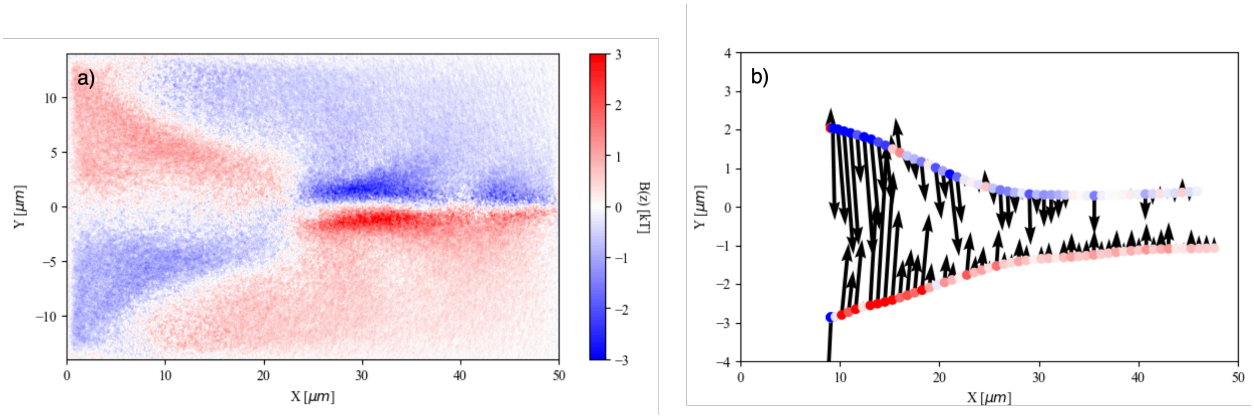

Figure 6.24: The a) collimating magnetic field shown at $t = 800\ fs$. The trajectory for two protons at multiple time steps is shown in b), with arrows showing the direction and magnitude of the $v \times B$ force they experience.

on the protons, which is plotted in Fig. 6.24b for two proton macroparticles that are tracked through the simulation at various time steps. The force is calculated as $v \times B$ to highlight the inward force the magnetic field has on the protons, directing them towards the axis. The length of arrow correlates to the magnitude of the force, and a longer arrow corresponds to a larger force. Once they are on axis, the amplitude of the transverse magnetic field diminishes. Additionally, the jet consists of a quasi-neutral collection of protons and electrons, which helps reduce any repulsive coulomb forces, enabling the jet to stay collimated for longer.

6.3.5 Radial Chirp Approximations

The radial chirp is the most straight-forward version of symmetric chirp, but has limitations in practice. Petawatt lasers reach large intensities, even when not focused, and special care must be taken in order to not damage optics. If concentric ring gratings are to be considered, it must be mentioned that there are several practical limitations that result in the scheme not being currently achievable in practice. First, the natural output of the grating pair results in the low frequency being diffracted at larger angles, resulting in the redder portion of the beam on the outside, and blue on the inside. To have the proper orientation of PFT that was simulated in the previous section, it would require the orientation of the spatial chirp to be inverted. This could be achieved with a pair of reflective axicons with high damage thresholds and large enough apertures to fully reflect the unfocused PW beam, which currently have never been manufactured. The pair of reflective axicons would also be needed to tune δr. Additionally, the concentric ring gratings that are manufactured currently are meant for low intensity applications and, as a result, are transmission gratings and small aperture. PW beamlines require reflective optics which have high damage thresholds and do not have B-integral accumulation issues like transmissive optics. Finally, there are polarization inefficiencies from the concentric ring structure that would require radial or azimuthal polarizations as input to the compressor. To avoid all of these issues and also reduce the complexity of the system needed for tuning parameters and inefficiencies, the radial chirp can be approximated as a superposition of properly arranged 1D spatially chirped beams as discussed in Section 5.3.6.

Simulations were run using 2, 4, 6, and 8 beam approximations of the 60^o PFT radially chirped case and oriented to have a radial polarization. Each beam is modeled as the output of a cascading beam splitter arrangement, with a schematic similar to that shown in Fig. 6.25. In this type of system, the goal is to split the original beam into N identical copies, each with 1/N the total energy of the original pulse. To achieve this, the beam splitters must

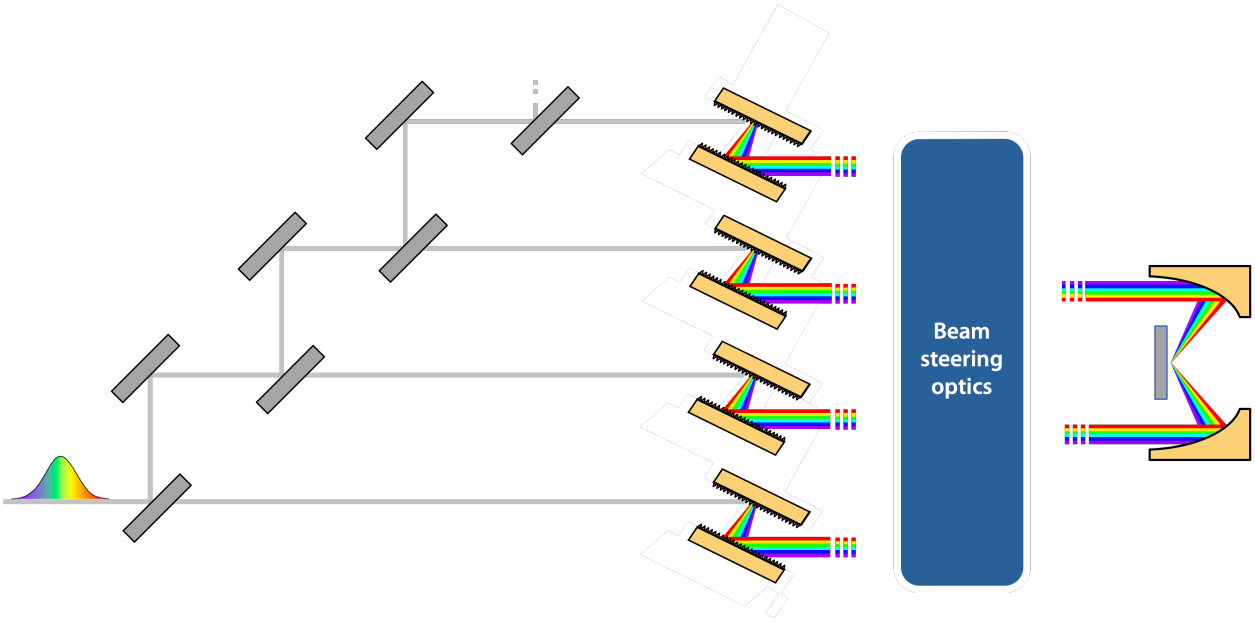

Figure 6.25: An example of a cascading beam splitter arrangement that could be used to generate identical copies of a pulse.

have a beam splitting ratio appropriately set. To make four copies, the first beam splitter needs a beam splitting ratio of reflection to transmission of 3:1. This causes 75% of the energy to reflect, and 25% to transmit. The next encountered beam splitter needs a ratio of 1:2, where 33% of the new beam is reflected (which is 25% of the original beam energy) and 66% transmitted. The last split requires a 1:1 beam splitter, resulting in 50% of the beam being transmitted and reflected (or 25% each of the original beam energy). This creates four beam copies, each with 1/4 of the original beam energy. This similar procedure would need to be followed for any arbitrary number of copies. The beam steering optics needed for this would require reflective optics to properly orient the spatially chirped beam (from Fig. 5.15, for example). Half-waveplates would also be needed to achieve proper orientation of the polarization.

The simulation results for the various beam approximations are visualized in Fig. 6.26 using the parameters from Table 6.5. As the number of beams increases, the axial confinement of the proton jet increases. For the 2 beam arrangement in Fig. 6.26a,e, there is very little

jet formation. As the number of beams increases to 4, a jet starts to appear. In Fig. 6.26f, there is an apparent leakage of protons along the axis where there is no beam on the foil. This leakage diminishes as the number of beams increases in Figs. 6.26e-h, and explains the decreasing divergence angle of Figs. 6.27b,c and the increasing number density of Fig. 6.27d. The more leakage of protons due to worse confinement, the worse the collimation and number density. The central core of the 4, 6, and 8 beam remains relatively confined and low divergence, but the metric for collimation is over the entire simulation window to account for the stray protons that diverge. The decrease in energy density as more beam copies are focused on the foil originates from the energy per beam. In the 2 beam case, each beam has half the initial energy from an even 50:50 beam split (12.5 J each) and so has a larger intensity and, as a result, higher peak proton energies. As the beam number increases, the energy per beam decreases, and so does peak proton energy.

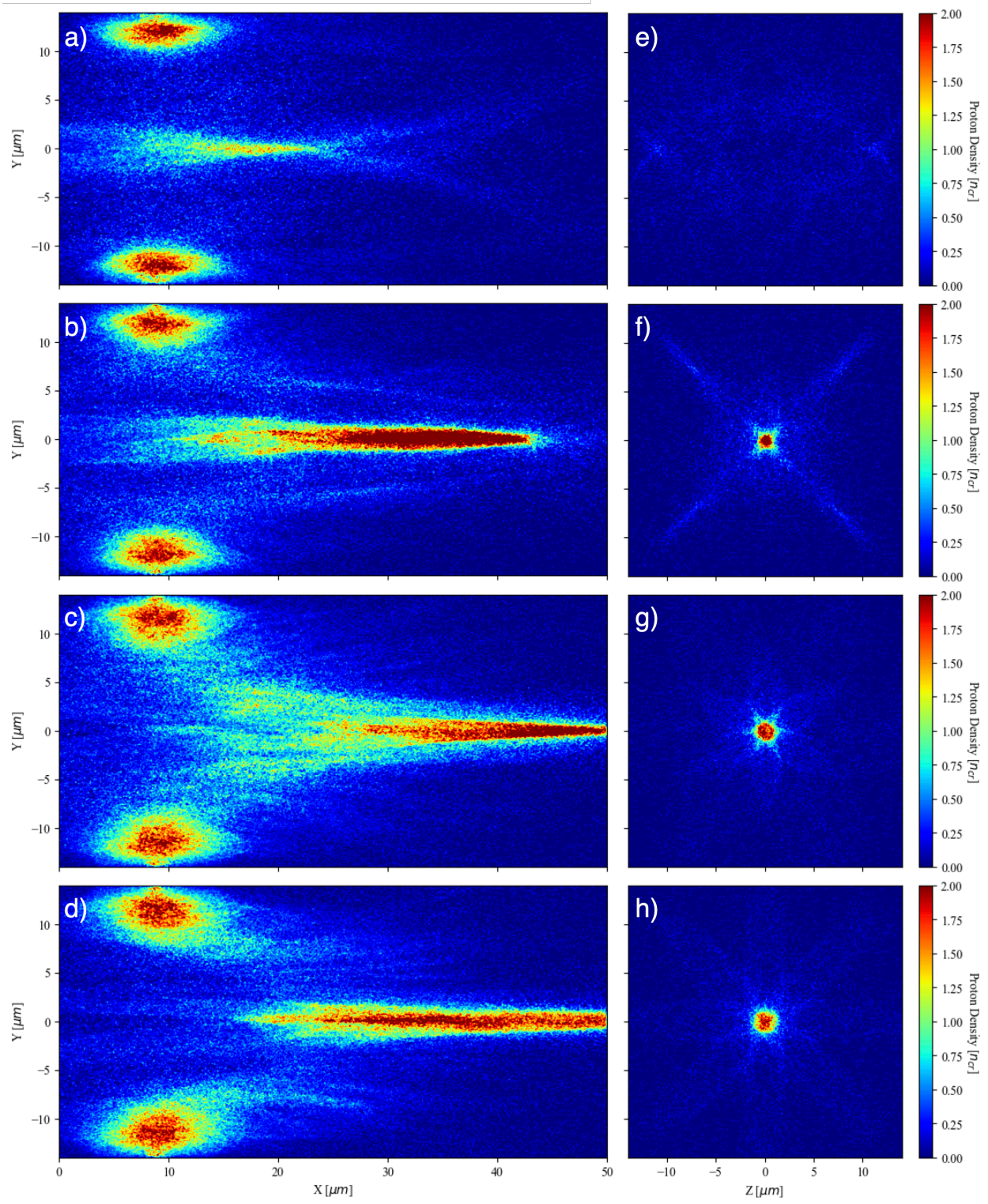

Figure 6.26: The accelerated protons for various radially chirped beams interacting with a hydrogen foil at $t = 800\ fs$. a)-d) are y-x plots at $z = 0$ from PIC simulations where the PFT of the beam is set to 60^o, and 2, 4, 6, and 8 beam approximations of the radial chirp are modeled, respectively. e)-h) are y-z plots of the transverse cross section of the simulation at $x = 40\ \mu m$.

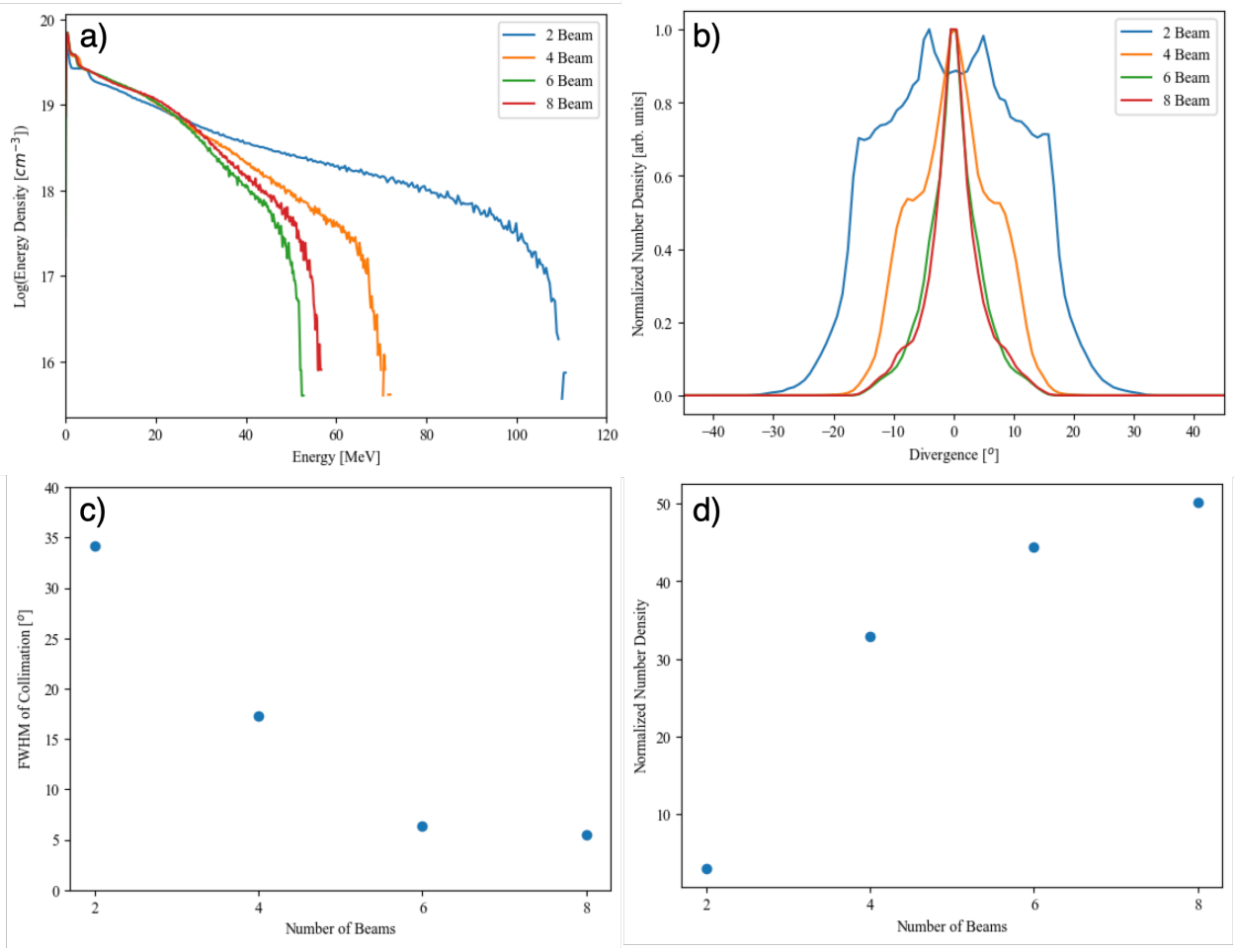

Figure 6.27: The a) energy spectrum at the time of maximum proton energy, b) divergence over the simulation window, c) variation of the FWHM of divergence , and d) total number density of protons at 40 μm is compared for four different beam numbers: 2, 4, 6, and 8.

6.3.6 Comments on Resolution and Assumptions

Throughout the presented work, several assumptions have been made. First, a perfect temporal and spatial Gaussian distribution for the laser pulse was assumed. The temporal profile of a realistic PW laser pulse typically has a temporal pedestal that leads and trails the primary peak. The leading edge will interact with the foil first, causing an expansion of the foil with an exponential profile. This preplasma was not modeled, and the hydrogen foil considered was treated as a step function in its spatial distribution. A preplasma is expected to change the interaction dynamics of the pulse interacting with the foil. The goal of the presented work was to preliminarily study the potential efficacy of the proposed space-time coupled laser interactions, and show the potential benefit on the accelerated protons in an idealistic setting. The hydrogen foil was also treated as an initially fully ionized species, which, for the intensities considered, is a good approximation. Hydrogen requires around $10^{16}\ W/cm^2$ to become fully ionized, and the intensities considered were in excess of $10^{21}\ W/cm^2$.

Additionally, the groove densities of the gratings are not the most efficient selection for the laser light simulated. For Ti:Sapphire centered at a wavelength $\lambda_0 = 800\ nm$, groove densities of 1480 lines/mm are optimal. For large aperture Nd:glass systems, the wavelength is centered near $\lambda_0 = 1057\ nm$ and utilize gratings around 1700 lines/mm. The gratings used change the spatio-temporal profile of the focused beam, and so different parameters would need to be varied and simulations conducted for a given arrangement to optimize the accelerated protons.

All of the 3D simulations shown were at very coarse resolution. This was necessary, as the computational resources needed to run every case at a sufficiently high resolution were beyond what was available for the duration of this work. Three cases were looked at with an improved grid resolution, $dx \times dy \times dz$, of $20\ nm \times 41.67\ nm \times 41.6\ nm$. Fig. 6.28a,b

show the low resolution results for a 0^o and 60^o PFT radial chirp. Fig. 6.28c,d show the high resolution results for the same cases. A collimated proton jet still forms in the high resolution simulations, with a different density profile compared to the low resolution counterparts. The energy densities vary slightly (Fig. 6.29a), achieving slightly higher peak proton energies in the high resolution simulations. Figs. 6.29b,c show that both simulations maintain low divergence, with a slight increase in collimation seen for the higher resolution. A similar increase in proton number density is observed from 0^o to 60^o in both resolution cases, with there being a more significant difference between PFT angles when using a smaller spatial step size, where the 0^o case is worse overall, and the 60^o chirp is better.

It was also validated that doing a multi-beam approximation holds when using a finer grid mesh. Fig. 6.30 shows the low resolution, 4 beam jet compared to the high resolution 4 beam jet. As the resolution was increased, a jet was still formed but with more spatial inhomogeneities. The high resolution simulation had a similar peak energy as the low resolution (Fig. 6.31(a)) and had a similar trend in collimation. The number densities were also quite similar in the 4 beams in Fig. 6.31(d). The overall trend between the radial simulation and the 4 beam approximation varied slightly with the increase in resolution, but the primary result of interest is that the proton jet still forms when considering a finer spatial resolution.

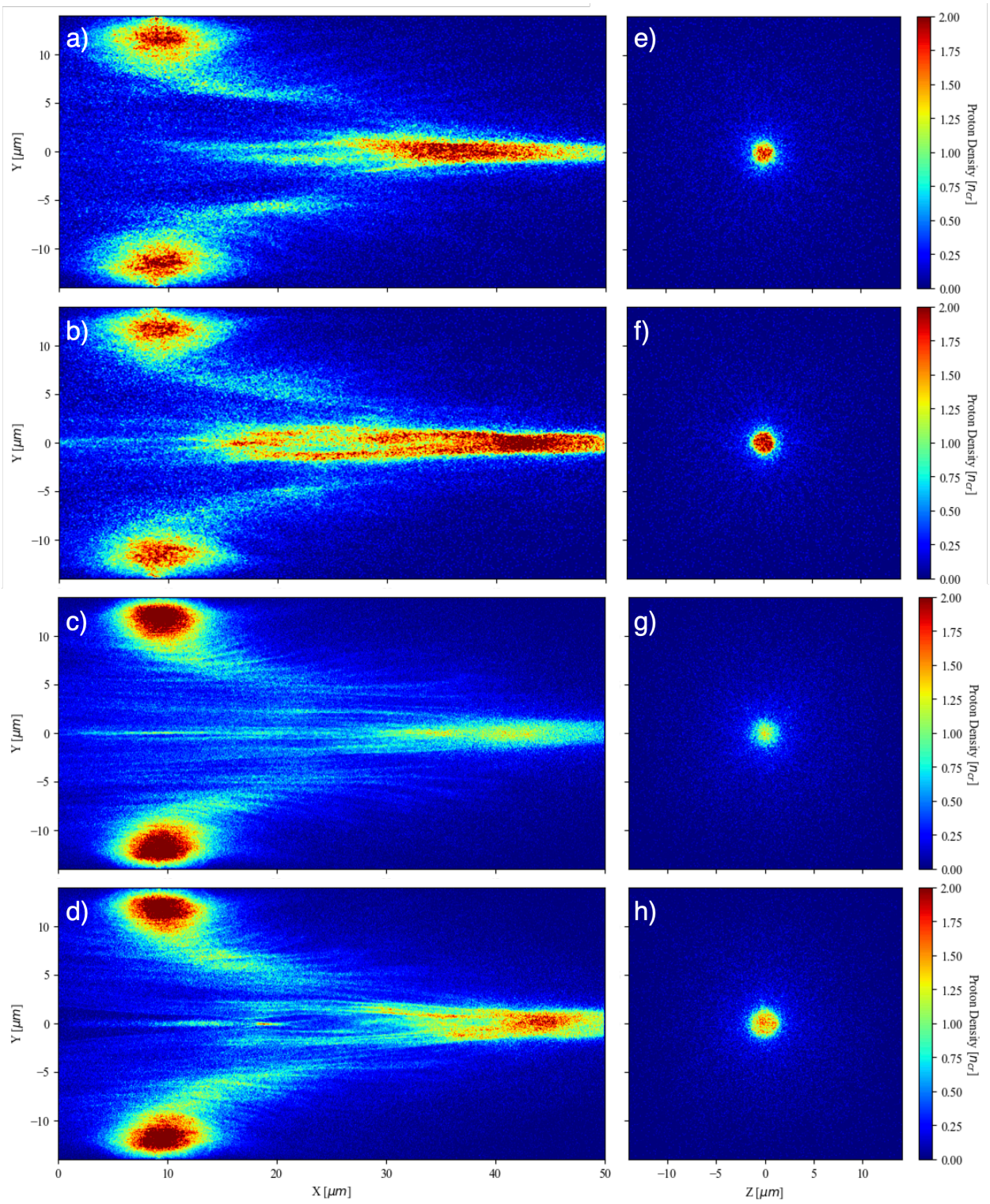

Figure 6.28: The accelerated protons for various radially chirped beams interacting with a hydrogen foil at $t = 800\ fs$. a),b) are y-x plots at $z = 0$ from PIC simulations where the PFT of the beam is set to 0° and 60°, respectively, for the low resolution 3D simulation parameters. c),d) are the same parameters for the high resolution simulations. e)-h) are y-z plots of the transverse cross section of the simulations at $x = 40\ \mu m$

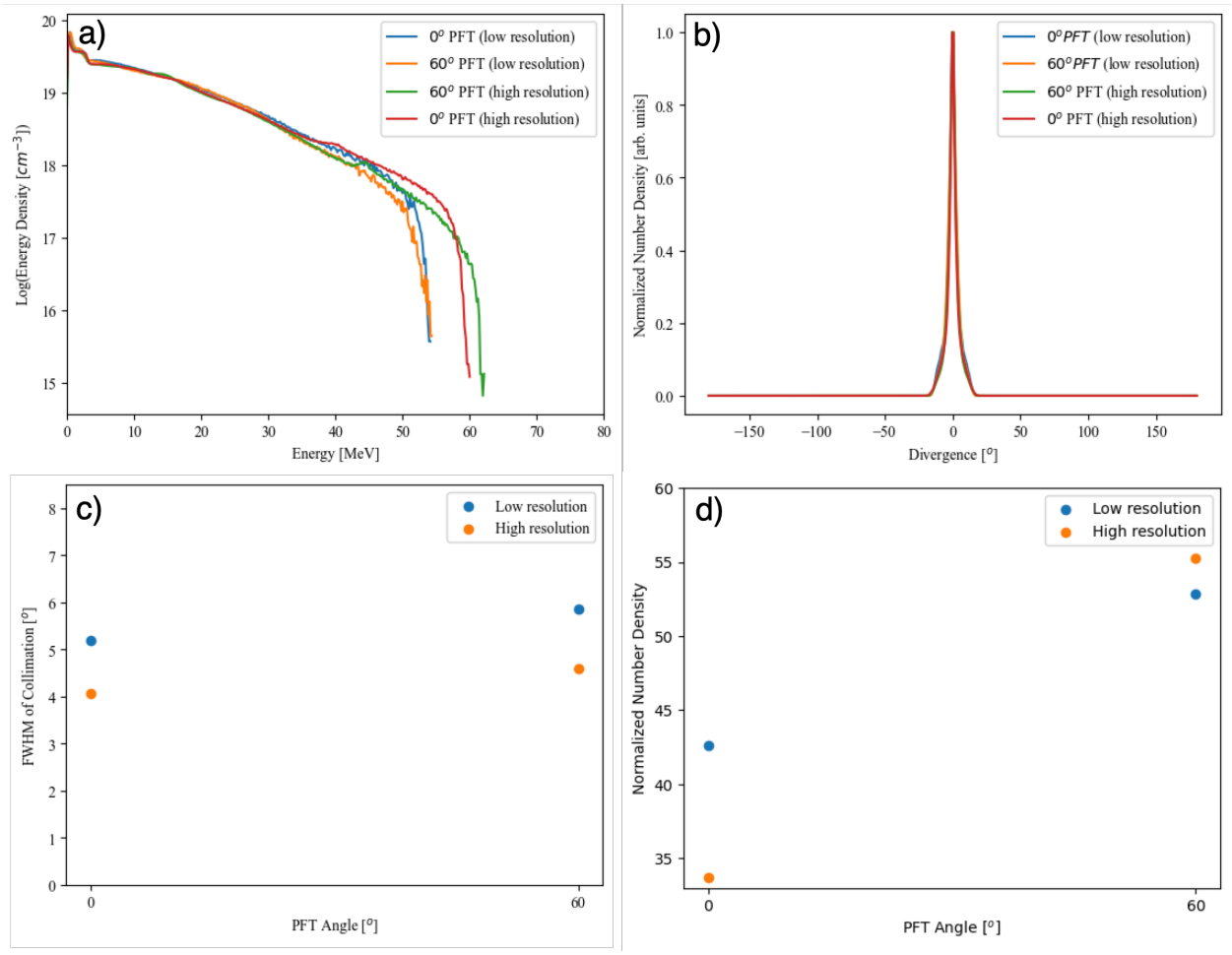

Figure 6.29: The a) energy density at the time of maximum proton energy, b) divergence over the simulation window, c) variation of the FWHM of divergence , and d) total number density of protons at 40 μm is compared for two different PFT angles (0° and 60° for both low and high resolution simulations.

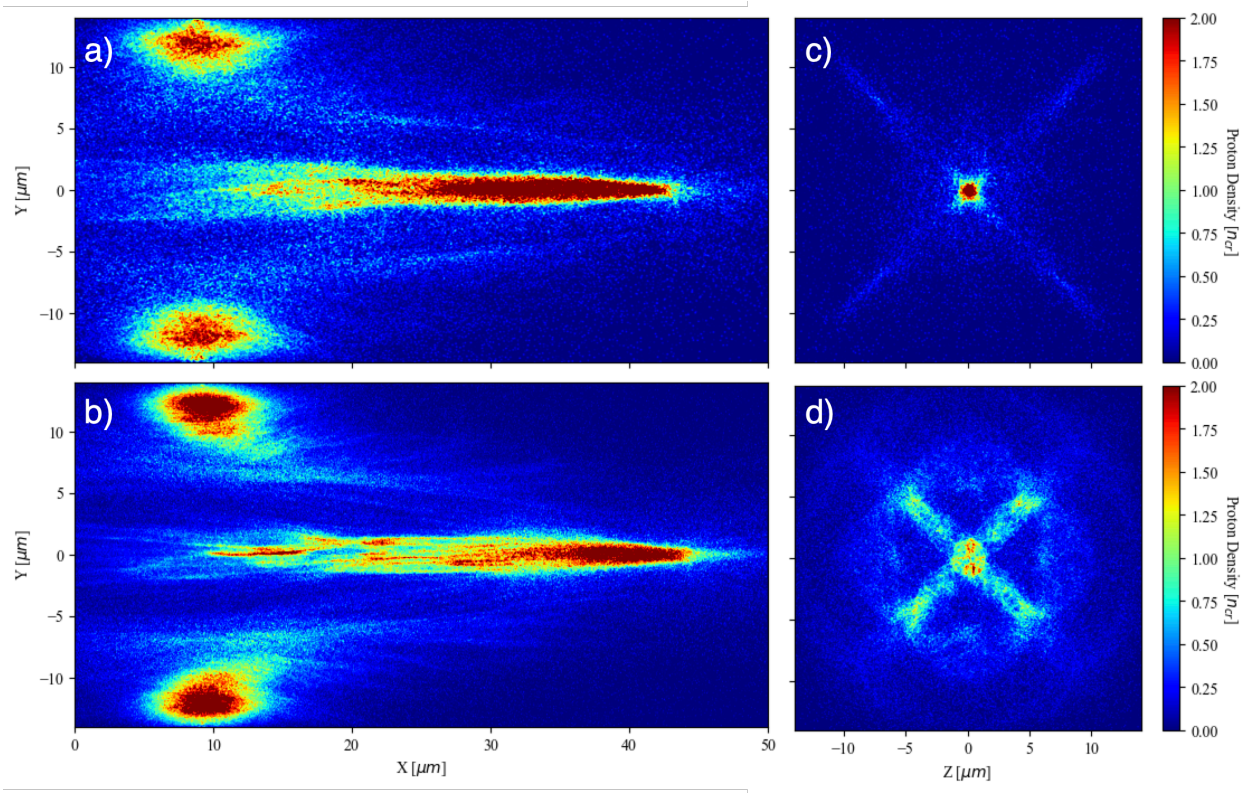

Figure 6.30: The accelerated protons for various radially chirped beams interacting with a hydrogen foil at $t = 800\ fs$. (a),(b) are y-x plots at $z = 0$ from PIC simulations of a 4 beam approximation of the radial chirp with parameters defined in Table 6.4 for the low and high resolution simulations, respectively. (c),(d) are y-z plots of the transverse cross section of the simulations at $x = 40\ \mu m$

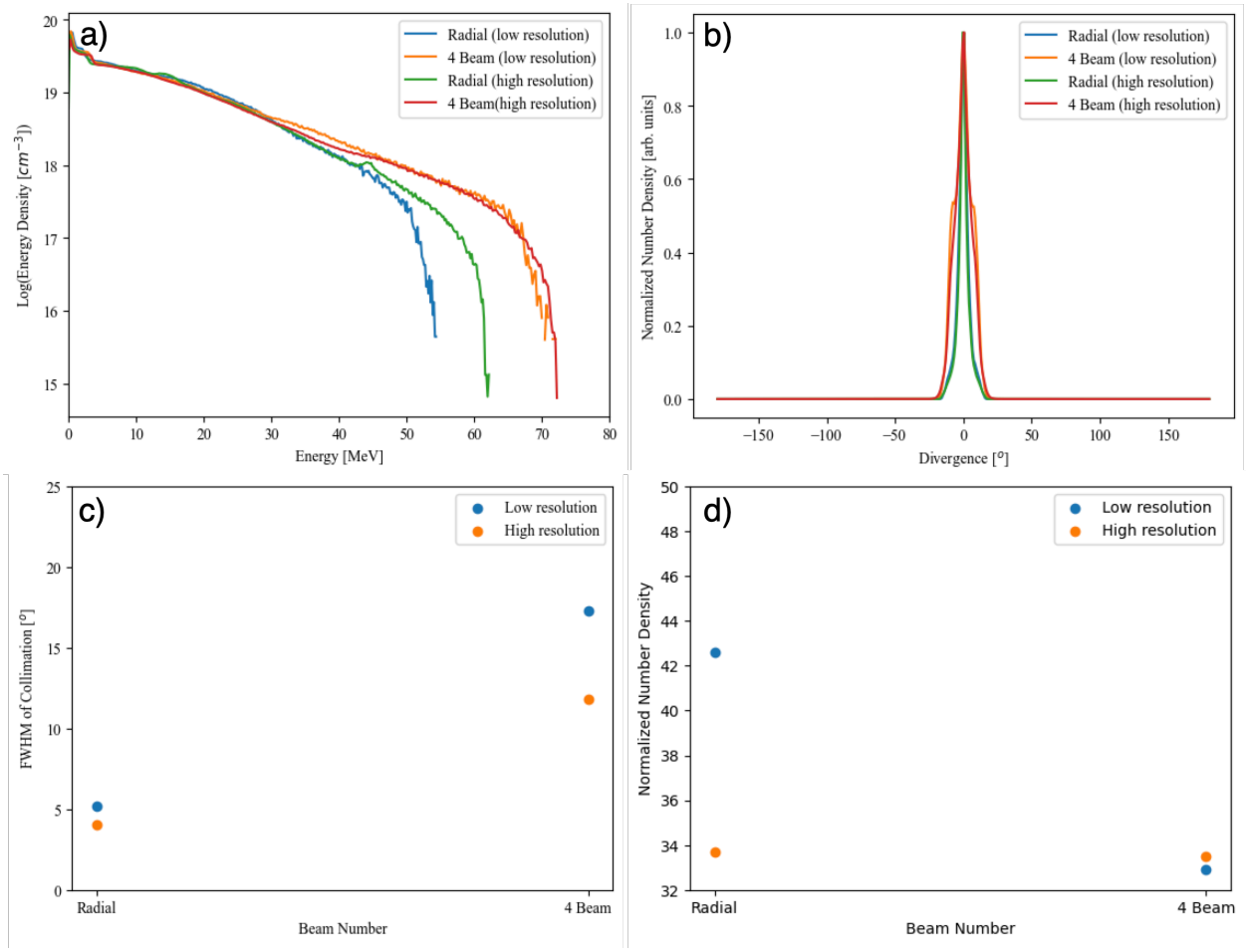

Figure 6.31: The a) energy density at the time of maximum proton energy, b) divergence over the simulation window, c) variation of the FWHM of divergence , and d) total number density of protons at 40 μm is compared for the radial chirp and the 4 beam approximation, for both low and high resolution simulations.

6.3.7 Conclusion

There are many ion acceleration schemes that rely on shaped targets to increase the maximum energy and enhance the axial confinement of accelerated protons. Specially tailored targets are difficult to manufacture and require shot-to-shot alignment. As petawatt lasers push towards multi-hertz operation, flat targets and hydrogen targets enable ion acceleration schemes operating at multiple shots per second. Instead of tailoring the target geometry, shaping of the laser pulse is an alternative method for increasing collimation of laser accelerated protons from a target. Focusing a spatially chirped beam, whether is a 1D chirp or 2D axisymmetric chirp, results in enhancements to accelerated protons from a hydrogen foil. The focal volume structures generated from a 1D spatial chirp results in proton beam steering and different maximum proton energies. Variation in the spatial distribution and collimation of accelerated protons was observed depending on the grating pair used to generate the spatial chirp, indicating the need for accurate modeling of the spatial chirp from a grating pair.

Axisymmetric spatial chirp utilizes the beam steering effects from the PFT to accelerate protons on-axis to generate a jet of protons. The accelerated protons and electrons introduce a self-generated magnetic field that creates an additional source of collimation through a $J \times B$ force that points toward the propagation axis. Varying any of the many parameters of the 2D chirp results in a tuning of the energy density, divergence angle, and number density, but in all cases a jet was still formed. A highly collimated jet of protons may be generated with only four 1D spatially chirped beams with proper orientation. Once the laser parameters are within a regime where collimation occurs, it is a relatively robust method for generating a proton jet.

Chapter 7

Conclusions and Future Outlook

In this thesis, it was shown that pulse front tilt, a simple space-time coupling generated from a focused spatially chirped beam, resulted in favorable and tunable characteristics of accelerated protons. The PFT generated from this focused pulse structure enabled proton beam steering and improved collimation. Highly collimated proton jets were formed that were able to propagate and maintain densities above n_c by arranging just four 1D spatially chirped beams in a particular orientation. Only one spatio-temporal coupling was studied and was shown to have significant effects on the proton beam structure. The study of other space-time couplings, such as spatial chirp and angular dispersion, and beam profiles beyond that of an ordinary Gaussian beam may lead to interesting laser-matter interactions. More complex beam shapes, higher order spatial modes, complicated phase profiles, and different polarization states could result in different interaction dynamics that may lead to useful ion beam properties.

Additionally, the thesis maintained an emphasis on accurate descriptions of laser pulse propagation. Assuming a particular analytic beam profile, which is a common assumption when modeling a laser-plasma interaction, leads to an idealized interaction geometry. The resulting

accelerated ions from such an interaction may not align with observations from experiments. In reality, the spatial and temporal distributions of a PW laser pulse are not described by simple analytic expressions, and making approximations on these profiles could influence accelerated ion characteristics. The code developed provides the capability of modeling any arbitrary beam and pulse profile, whether it is described analytically or with measured values, and propagates the pulse throughout a system with a high degree of accuracy. Through improved models of the propagation, more realistic profiles may be used in PIC simulations to enable a closer match of simulation to experiment.

Bibliography

[1] E. C. Nelson, K. D. Chesnut, T. Reutershan, H. H. Effarah, K. J. Charbonnet, and C. P. J. Barty. Pulse front distortions in focused spatially chirped beams. *Optics Continuum*, 3(7):1051–1060, 2024.

[2] Donna Strickland and Gerard Mourou. Compression of amplified chirped optical pulses. *Optics Communications*, 55(6):447–449, 1985.

[3] Stephen P. Hatchett, Curtis G. Brown, Thomas E. Cowan, Eugene A. Henry, Joy S. Johnson, Michael H. Key, Jeffrey A. Koch, A. Bruce Langdon, Barbara F. Lasinski, Richard W. Lee, Andrew J. Mackinnon, Deanna M. Pennington, Michael D. Perry, Thomas W. Phillips, Markus Roth, T. Craig Sangster, Mike S. Singh, Richard A. Snavely, Mark A. Stoyer, Scott C. Wilks, and Kazuhito Yasuike. Electron, photon, and ion beams from the relativistic interaction of petawatt laser pulses with solid targets. *Physics of Plasmas*, 7(5):2076–2082, 2000.

[4] Agnese Lagzda. *VHEE Radiotherapy Studies at CLARA and CLEAR facilities*. PhD thesis, 2019. Copyright - Database copyright ProQuest LLC; ProQuest does not claim copyright in the individual underlying works; Last updated - 2024-01-29.

[5] H. Abu-Shawareb, R. Acree, P. Adams, J. Adams, B. Addis, R. Aden, P. Adrian, B. B. Afeyan, M. Aggleton, L. Aghaian, A. Aguirre, D. Aikens, J. Akre, F. Albert, M. Albrecht, B. J. Albright, J. Albritton, J. Alcala, C. Alday, D. A. Alessi, N. Alexander, J. Alfonso, N. Alfonso, E. Alger, S. J. Ali, Z. A. Ali, A. Allen, W. E. Alley, P. Amala, P. A. Amendt, P. Amick, S. Ammula, C. Amorin, D. J. Ampleford, R. W. Anderson, T. Anklam, N. Antipa, B. Appelbe, C. Aracne-Ruddle, E. Araya, T. N. Archuleta, M. Arend, P. Arnold, T. Arnold, A. Arsenlis, J. Asay, L. J. Atherton, D. Atkinson, R. Atkinson, J. M. Auerbach, B. Austin, L. Auyang, A. A. S. Awwal, N. Aybar, J. Ayers, S. Ayers, T. Ayers, S. Azevedo, B. Bachmann, C. A. Back, J. Bae, D. S. Bailey, J. Bailey, T. Baisden, K. L. Baker, H. Baldis, D. Barber, M. Barberis, D. Barker, A. Barnes, C. W. Barnes, M. A. Barrios, C. Barty, I. Bass, S. H. Batha, S. H. Baxamusa, G. Bazan, J. K. Beagle, R. Beale, B. R. Beck, J. B. Beck, M. Bedzyk, R. G. Beeler, R. G. Beeler, W. Behrendt, L. Belk, P. Bell, M. Belyaev, J. F. Benage, G. Bennett, L. R. Benedetti, L. X. Benedict, R. L. Berger, T. Bernat, L. A. Bernstein, B. Berry, L. Bertolini, G. Besenbruch, J. Betcher, R. Bettenhausen, R. Betti, B. Bezzerides, S. D. Bhandarkar, R. Bickel, J. Biener, T. Biesiada, K. Bigelow, J. Bigelow-Granillo, V. Bigman, R. M. Bionta, N. W. Birge, M. Bitter, A. C. Black, R. Bleile, D. L.

Bleuel, E. Bliss, E. Bliss, B. Blue, T. Boehly, K. Boehm, C. D. Boley, R. Bonanno, E. J. Bond, T. Bond, M. J. Bonino, M. Borden, J.-L. Bourgade, J. Bousquet, J. Bowers, M. Bowers, R. Boyd, D. Boyle, A. Bozek, D. K. Bradley, K. S. Bradley, P. A. Bradley, L. Bradley, L. Brannon, P. S. Brantley, D. Braun, T. Braun, K. Brienza-Larsen, R. Briggs, T. M. Briggs, J. Britten, E. D. Brooks, D. Browning, M. W. Bruhn, T. A. Brunner, H. Bruns, G. Brunton, B. Bryant, T. Buczek, J. Bude, L. Buitano, S. Burkhart, J. Burmark, A. Burnham, R. Burr, L. E. Busby, B. Butlin, R. Cabeltis, M. Cable, W. H. Cabot, B. Cagadas, J. Caggiano, R. Cahayag, S. E. Caldwell, S. Calkins, D. A. Callahan, J. Calleja-Aguirre, L. Camara, D. Camp, E. M. Campbell, J. H. Campbell, B. Carey, R. Carey, K. Carlisle, L. Carlson, L. Carman, J. Carmichael, A. Carpenter, C. Carr, J. A. Carrera, D. Casavant, A. Casey, D. T. Casey, A. Castillo, E. Castillo, J. I. Castor, C. Castro, W. Caughey, R. Cavitt, J. Celeste, P. M. Celliers, C. Cerjan, G. Chandler, B. Chang, C. Chang, J. Chang, L. Chang, R. Chapman, T. D. Chapman, L. Chase, H. Chen, H. Chen, K. Chen, L.-Y. Chen, B. Cheng, J. Chittenden, C. Choate, J. Chou, R. E. Chrien, M. Chrisp, K. Christensen, M. Christensen, N. S. Christiansen, A. R. Christopherson, M. Chung, J. A. Church, A. Clark, D. S. Clark, K. Clark, R. Clark, L. Claus, B. Cline, J. A. Cline, J. A. Cobble, K. Cochrane, B. Cohen, S. Cohen, M. R. Collette, G. W. Collins, L. A. Collins, T. J. B. Collins, A. Conder, B. Conrad, M. Conyers, A. W. Cook, D. Cook, R. Cook, J. C. Cooley, G. Cooper, T. Cope, S. R. Copeland, F. Coppari, J. Cortez, J. Cox, D. H. Crandall, J. Crane, R. S. Craxton, M. Cray, A. Crilly, J. W. Crippen, D. Cross, M. Cuneo, G. Cuotts, C. E. Czajka, D. Czechowicz, T. Daly, P. Danforth, C. Danly, R. Darbee, B. Darlington, P. Datte, L. Dauffy, G. Davalos, S. Davidovits, P. Davis, J. Davis, S. Dawson, R. D. Day, T. H. Day, M. Dayton, C. Deck, C. Decker, C. Deeney, K. A. DeFriend, G. Deis, N. D. Delamater, J. A. Delettrez, R. Demaret, S. Demos, S. M. Dempsey, R. Desjardin, T. Desjardins, M. P. Desjarlais, E. L. Dewald, J. DeYoreo, S. Diaz, G. Dimonte, T. R. Dittrich, L. Divol, S. N. Dixit, J. Dixon, A. Do, E. S. Dodd, D. Dolan, A. Donovan, M. Donovan, T. Döppner, C. Dorrer, N. Dorsano, M. R. Douglas, D. Dow, J. Downie, E. Downing, M. Dozieres, V. Draggoo, D. Drake, R. P. Drake, T. Drake, G. Dreifuerst, O. Drury, D. F. DuBois, P. F. DuBois, G. Dunham, M. Durocher, R. Dylla-Spears, A. K. L. Dymoke-Bradshaw, B. Dzenitis, C. Ebbers, M. Eckart, S. Eddinger, D. Eder, D. Edgell, M. J. Edwards, P. Efthimion, J. H. Eggert, B. Ehrlich, P. Ehrmann, S. Elhadj, C. Ellerbee, N. S. Elliott, C. L. Ellison, F. Elsner, M. Emerich, K. Engelhorn, T. England, E. English, P. Epperson, R. Epstein, G. Erbert, M. A. Erickson, D. J. Erskine, A. Erlandson, R. J. Espinosa, C. Estes, K. G. Estabrook, S. Evans, A. Fabyan, J. Fair, R. Fallejo, N. Farmer, W. A. Farmer, M. Farrell, V. E. Fatherley, M. Fedorov, E. Feigenbaum, T. Fehrenbach, M. Feit, B. Felker, W. Ferguson, J. C. Fernandez, A. Fernandez-Panella, S. Fess, J. E. Field, C. V. Filip, J. R. Fincke, T. Finn, S. M. Finnegan, R. G. Finucane, M. Fischer, A. Fisher, J. Fisher, B. Fishler, D. Fittinghoff, P. Fitzsimmons, M. Flegel, K. A. Flippo, J. Florio, J. Folta, P. Folta, L. R. Foreman, C. Forrest, A. Forsman, J. Fooks, M. Foord, R. Fortner, K. Fournier, D. E. Fratanduono, N. Frazier, T. Frazier, C. Frederick, M. S. Freeman, J. Frenje, D. Frey, G. Frieders, S. Friedrich, D. H. Froula, J. Fry, T. Fuller, J. Gaffney, S. Gales, B. Le Galloudec, K. K. Le Galloudec, A. Gambhir, L. Gao, W. J. Garbett, A. Garcia, C. Gates, E. Gaut, P. Gauthier, Z. Gavin, J. Gay-

lord, C. G. R. Geddes, M. Geissel, F. Génin, J. Georgeson, H. Geppert-Kleinrath, V. Geppert-Kleinrath, N. Gharibyan, J. Gibson, C. Gibson, E. Giraldez, V. Glebov, S. G. Glendinning, S. Glenn, S. H. Glenzer, S. Goade, P. L. Gobby, S. R. Goldman, B. Golick, M. Gomez, V. Goncharov, D. Goodin, P. Grabowski, E. Grafil, P. Graham, J. Grandy, E. Grasz, F. R. Graziani, G. Greenman, J. A. Greenough, A. Greenwood, G. Gregori, T. Green, J. R. Griego, G. P. Grim, J. Grondalski, S. Gross, J. Guckian, N. Guler, B. Gunney, G. Guss, S. Haan, J. Hackbarth, L. Hackel, R. Hackel, C. Haefner, C. Hagmann, K. D. Hahn, S. Hahn, B. J. Haid, B. M. Haines, B. M. Hall, C. Hall, G. N. Hall, M. Hamamoto, S. Hamel, C. E. Hamilton, B. A. Hammel, J. H. Hammer, G. Hampton, A. Hamza, A. Handler, S. Hansen, D. Hanson, R. Haque, D. Harding, E. Harding, J. D. Hares, D. B. Harris, J. A. Harte, E. P. Hartouni, R. Hatarik, S. Hatchett, A. A. Hauer, M. Havre, R. Hawley, J. Hayes, J. Hayes, S. Hayes, A. Hayes-Sterbenz, C. A. Haynam, D. A. Haynes, D. Headley, A. Heal, J. E. Heebner, S. Heerey, G. M. Heestand, R. Heeter, N. Hein, C. Heinbockel, C. Hendricks, M. Henesian, J. Heninger, J. Henrikson, E. A. Henry, E. B. Herbold, M. R. Hermann, G. Hermes, J. E. Hernandez, V. J. Hernandez, M. C. Herrmann, H. W. Herrmann, O. D. Herrera, D. Hewett, R. Hibbard, D. G. Hicks, D. P. Higginson, D. Hill, K. Hill, T. Hilsabeck, D. E. Hinkel, D. D. Ho, V. K. Ho, J. K. Hoffer, N. M. Hoffman, M. Hohenberger, M. Hohensee, W. Hoke, D. Holdener, F. Holdener, J. P. Holder, B. Holko, D. Holunga, J. F. Holzrichter, J. Honig, D. Hoover, D. Hopkins, L. F. Berzak Hopkins, M. Hoppe, M. L. Hoppe, J. Horner, R. Hornung, C. J. Horsfield, J. Horvath, D. Hotaling, R. House, L. Howell, W. W. Hsing, S. X. Hu, H. Huang, J. Huckins, H. Hui, K. D. Humbird, J. Hund, J. Hunt, O. A. Hurricane, M. Hutton, K. H.-K. Huynh, L. Inandan, C. Iglesias, I. V. Igumenshchev, I. Ivanovich, N. Izumi, M. Jackson, J. Jackson, S. D. Jacobs, G. James, K. Jancaitis, J. Jarboe, L. C. Jarrott, D. Jasion, J. Jaquez, J. Jeet, A. E. Jenei, J. Jensen, J. Jimenez, R. Jimenez, D. Jobe, Z. Johal, H. M. Johns, D. Johnson, M. A. Johnson, M. Gatu Johnson, R. J. Johnson, S. Johnson, S. A. Johnson, T. Johnson, K. Jones, O. Jones, M. Jones, R. Jorge, H. J. Jorgenson, M. Julian, B. I. Jun, R. Jungquist, J. Kaae, N. Kabadi, D. Kaczala, D. Kalantar, K. Kangas, V. V. Karasiev, M. Karasik, V. Karpenko, A. Kasarky, K. Kasper, R. Kauffman, M. I. Kaufman, C. Keane, L. Keaty, L. Kegelmeyer, P. A. Keiter, P. A. Kellett, J. Kellogg, J. H. Kelly, S. Kemic, A. J. Kemp, G. E. Kemp, G. D. Kerbel, D. Kershaw, S. M. Kerr, T. J. Kessler, M. H. Key, S. F. Khan, H. Khater, C. Kiikka, J. Kilkenny, Y. Kim, Y.-J. Kim, J. Kimko, M. Kimmel, J. M. Kindel, J. King, R. K. Kirkwood, L. Klaus, D. Klem, J. L. Kline, J. Klingmann, G. Kluth, P. Knapp, J. Knauer, J. Knipping, M. Knudson, D. Kobs, J. Koch, T. Kohut, C. Kong, J. M. Koning, P. Koning, S. Konior, H. Kornblum, L. B. Kot, B. Kozioziemski, M. Kozlowski, P. M. Kozlowski, J. Krammen, N. S. Krasheninnikova, C. M. Krauland, B. Kraus, W. Krauser, J. D. Kress, A. L. Kritcher, E. Krieger, J. J. Kroll, W. L. Kruer, M. K. G. Kruse, S. Kucheyev, M. Kumbera, S. Kumpan, J. Kunimune, E. Kur, B. Kustowski, T. J. T. Kwan, G. A. Kyrala, S. Laffite, M. Lafon, K. LaFortune, L. Lagin, B. Lahmann, B. Lairson, O. L. Landen, T. Land, M. Lane, D. Laney, A. B. Langdon, J. Langenbrunner, S. H. Langer, A. Langro, N. E. Lanier, T. E. Lanier, D. Larson, B. F. Lasinski, D. Lassle, D. LaTray, G. Lau, N. Lau, C. Laumann, A. Laurence, T. A. Laurence, J. Lawson, H. P. Le, R. R. Leach, L. Leal, A. Leatherland, K. LeChien, B. Lechleiter, A. Lee, M. Lee,

T. Lee, R. J. Leeper, E. Lefebvre, J.-P. Leidinger, B. LeMire, R. W. Lemke, N. C. Lemos, S. Le Pape, R. Lerche, S. Lerner, S. Letts, K. Levedahl, T. Lewis, C. K. Li, H. Li, J. Li, W. Liao, Z. M. Liao, D. Liedahl, J. Liebman, G. Lindford, E. L. Lindman, J. D. Lindl, H. Loey, R. A. London, F. Long, E. N. Loomis, F. E. Lopez, H. Lopez, E. Losbanos, S. Loucks, R. Lowe-Webb, E. Lundgren, A. P. Ludwigsen, R. Luo, J. Lusk, R. Lyons, T. Ma, Y. Macallop, M. J. MacDonald, B. J. MacGowan, J. M. Mack, A. J. Mackinnon, S. A. MacLaren, A. G. MacPhee, G. R. Magelssen, J. Magoon, R. M. Malone, T. Malsbury, R. Managan, R. Mancini, K. Manes, D. Maney, D. Manha, O. M. Mannion, A. M. Manuel, M. J.-E. Manuel, E. Mapoles, G. Mara, T. Marcotte, E. Marin, M. M. Marinak, D. A. Mariscal, E. F. Mariscal, E. V. Marley, J. A. Marozas, R. Marquez, C. D. Marshall, F. J. Marshall, M. Marshall, S. Marshall, J. Marticorena, J. I. Martinez, D. Martinez, I. Maslennikov, D. Mason, R. J. Mason, L. Masse, W. Massey, P.-E. Masson-Laborde, N. D. Masters, D. Mathisen, E. Mathison, J. Matone, M. J. Matthews, C. Mattoon, T. R. Mattsson, K. Matzen, C. W. Mauche, M. Mauldin, T. McAbee, M. McBurney, T. Mccarville, R. L. McCrory, A. M. McEvoy, C. McGuffey, M. Mcinnis, P. McKenty, M. S. McKinley, J. B. McLeod, A. McPherson, B. Mcquillan, M. Meamber, K. D. Meaney, N. B. Meezan, R. Meissner, T. A. Mehlhorn, N. C. Mehta, J. Menapace, F. E. Merrill, B. T. Merritt, E. C. Merritt, D. D. Meyerhofer, S. Mezyk, R. J. Mich, P. A. Michel, D. Milam, C. Miller, D. Miller, D. S. Miller, E. Miller, E. K. Miller, J. Miller, M. Miller, P. E. Miller, T. Miller, W. Miller, V. Miller-Kamm, M. Millot, J. L. Milovich, P. Minner, J.-L. Miquel, S. Mitchell, K. Molvig, R. C. Montesanti, D. S. Montgomery, M. Monticelli, A. Montoya, J. D. Moody, A. S. Moore, E. Moore, M. Moran, J. C. Moreno, K. Moreno, B. E. Morgan, T. Morrow, J. W. Morton, E. Moses, K. Moy, R. Muir, M. S. Murillo, J. E. Murray, J. R. Murray, D. H. Munro, T. J. Murphy, F. M. Munteanu, J. Nafziger, T. Nagayama, S. R. Nagel, R. Nast, R. A. Negres, A. Nelson, D. Nelson, J. Nelson, S. Nelson, S. Nemethy, P. Neumayer, K. Newman, M. Newton, H. Nguyen, J.-M. G. Di Nicola, P. Di Nicola, C. Niemann, A. Nikroo, P. M. Nilson, A. Nobile, V. Noorai, R. C. Nora, M. Norton, M. Nostrand, V. Note, S. Novell, P. F. Nowak, A. Nunez, R. A. Nyholm, M. O'Brien, A. Oceguera, J. A. Oertel, A. L. Oesterle, J. Okui, B. Olejniczak, J. Oliveira, P. Olsen, B. Olson, K. Olson, R. E. Olson, Y. P. Opachich, N. Orsi, C. D. Orth, M. Owen, S. Padalino, E. Padilla, R. Paguio, S. Paguio, J. Paisner, S. Pajoom, A. Pak, S. Palaniyappan, K. Palma, T. Pannell, F. Papp, D. Paras, T. Parham, H.-S. Park, A. Pasternak, S. Patankar, M. V. Patel, P. K. Patel, R. Patterson, S. Patterson, B. Paul, M. Paul, E. Pauli, O. T. Pearce, J. Pearcy, A. Pedretti, B. Pedrotti, A. Peer, L. J. Pelz, B. Penetrante, J. Penner, A. Perez, L. J. Perkins, E. Pernice, T. S. Perry, S. Person, D. Petersen, T. Petersen, D. L. Peterson, E. B. Peterson, J. E. Peterson, J. L. Peterson, K. Peterson, R. R. Peterson, R. D. Petrasso, F. Philippe, D. Phillion, T. J. Phipps, E. Piceno, L. Pickworth, Y. Ping, J. Pino, K. Piston, R. Plummer, G. D. Pollack, S. M. Pollaine, B. B. Pollock, D. Ponce, J. Ponce, J. Pontelandolfo, J. L. Porter, J. Post, O. Poujade, C. Powell, H. Powell, G. Power, M. Pozulp, M. Prantil, M. Prasad, S. Pratuch, S. Price, K. Primdahl, S. Prisbrey, R. Procassini, A. Pruyne, B. Pudliner, S. R. Qiu, K. Quan, M. Quinn, J. Quintenz, P. B. Radha, F. Rainer, J. E. Ralph, K. S. Raman, R. Raman, P. W. Rambo, S. Rana, A. Randewich, D. Rardin, M. Ratledge, N. Ravelo, F. Ravizza, M. Rayce, A. Raymond, B. Raymond, B. Reed, C. Reed,

S. Regan, B. Reichelt, V. Reis, S. Reisdorf, V. Rekow, B. A. Remington, A. Rendon, W. Requieron, M. Rever, H. Reynolds, J. Reynolds, J. Rhodes, M. Rhodes, M. C. Richardson, B. Rice, N. G. Rice, R. Rieben, A. Rigatti, S. Riggs, H. G. Rinderknecht, K. Ring, B. Riordan, R. Riquier, C. Rivers, D. Roberts, V. Roberts, G. Robertson, H. F. Robey, J. Robles, P. Rocha, G. Rochau, J. Rodriguez, S. Rodriguez, M. D. Rosen, M. Rosenberg, G. Ross, J. S. Ross, P. Ross, J. Rouse, D. Rovang, A. M. Rubenchik, M. S. Rubery, C. L. Ruiz, M. Rushford, B. Russ, J. R. Rygg, B. S. Ryujin, R. A. Sacks, R. F. Sacks, K. Saito, T. Salmon, J. D. Salmonson, J. Sanchez, S. Samuelson, M. Sanchez, C. Sangster, A. Saroyan, J. Sater, A. Satsangi, S. Sauers, R. Saunders, J. P. Sauppe, R. Sawicki, D. Sayre, M. Scanlan, K. Schaffers, G. T. Schappert, S. Schiaffino, D. J. Schlossberg, D. W. Schmidt, P. F. Schmit, J. M. Smidt, D. H. G. Schneider, M. B. Schneider, R. Schneider, M. Schoff, M. Schollmeier, C. R. Schroeder, S. E. Schrauth, H. A. Scott, I. Scott, J. M. Scott, R. H. H. Scott, C. R. Scullard, T. Sedillo, F. H. Seguin, W. Seka, J. Senecal, S. M. Sepke, L. Seppala, K. Sequoia, J. Severyn, J. M. Sevier, N. Sewell, S. Seznec, R. C. Shah, J. Shamlian, D. Shaughnessy, M. Shaw, R. Shaw, C. Shearer, R. Shelton, N. Shen, M. W. Sherlock, A. I. Shestakov, E. L. Shi, S. J. Shin, N. Shingleton, W. Shmayda, M. Shor, M. Shoup, C. Shuldberg, L. Siegel, F. J. Silva, A. N. Simakov, B. T. Sims, D. Sinars, P. Singh, H. Sio, K. Skulina, S. Skupsky, S. Slutz, M. Sluyter, V. A. Smalyuk, D. Smauley, R. M. Smeltser, C. Smith, I. Smith, J. Smith, L. Smith, R. Smith, R. Smith, M. Schölmerich, R. Sohn, S. Sommer, C. Sorce, M. Sorem, J. M. Soures, M. L. Spaeth, B. K. Spears, S. Speas, D. Speck, R. Speck, J. Spears, T. Spinka, P. T. Springer, M. Stadermann, B. Stahl, J. Stahoviak, J. Stanley, L. G. Stanton, R. Steele, W. Steele, D. Steinman, R. Stemke, R. Stephens, S. Sterbenz, P. Sterne, D. Stevens, J. Stevers, C. H. Still, C. Stoeckl, W. Stoeffl, J. S. Stolken, C. Stolz, E. Storm, G. Stone, S. Stoupin, E. Stout, I. Stowers, R. Strauser, H. Streckart, J. Streit, D. J. Strozzi, J. Stutz, L. Summers, T. Suratwala, G. Sutcliffe, L. J. Suter, S. B. Sutton, V. Svidzinski, G. Swadling, W. Sweet, A. Szoke, M. Tabak, M. Takagi, A. Tambazidis, V. Tang, M. Taranowski, L. A. Taylor, S. Telford, W. Theobald, M. Thi, A. Thomas, C. A. Thomas, I. Thomas, R. Thomas, I. J. Thompson, A. Thongstisubskul, C. B. Thorsness, G. Tietbohl, R. E. Tipton, M. Tobin, N. Tomlin, R. Tommasini, A. J. Toreja, J. Torres, R. P. J. Town, S. Townsend, J. Trenholme, A. Trivelpiece, C. Trosseille, H. Truax, D. Trummer, S. Trummer, T. Truong, D. Tubbs, E. R. Tubman, T. Tunnell, D. Turnbull, R. E. Turner, M. Ulitsky, R. Upadhye, J. L. Vaher, P. VanArsdall, D. VanBlarcom, M. Vandenboomgaerde, R. VanQuinlan, B. M. Van Wonterghem, W. S. Varnum, A. L. Velikovich, A. Vella, C. P. Verdon, B. Vermillion, S. Vernon, R. Vesey, J. Vickers, R. M. Vignes, M. Visosky, J. Vocke, P. L. Volegov, S. Vonhof, R. Von Rotz, H. X. Vu, M. Vu, D. Wall, J. Wall, R. Wallace, B. Wallin, D. Walmer, C. A. Walsh, C. F. Walters, C. Waltz, A. Wan, A. Wang, Y. Wang, J. S. Wark, B. E. Warner, J. Watson, R. G. Watt, P. Watts, J. Weaver, R. P. Weaver, S. Weaver, C. R. Weber, P. Weber, S. V. Weber, P. Wegner, B. Welday, L. Welser-Sherrill, K. Weiss, K. B. Wharton, G. F. Wheeler, W. Whistler, R. K. White, H. D. Whitley, P. Whitman, M. E. Wickett, K. Widmann, C. Widmayer, J. Wiedwald, R. Wilcox, S. Wilcox, C. Wild, B. H. Wilde, C. H. Wilde, K. Wilhelmsen, M. D. Wilke, H. Wilkens, P. Wilkins, S. C. Wilks, E. A. Williams, G. J. Williams, W. Williams, W. H. Williams, D. C. Wilson, B. Wilson, E. Wilson, R. Wil-

son, S. Winters, P. J. Wisoff, M. Wittman, J. Wolfe, A. Wong, K. W. Wong, L. Wong, N. Wong, R. Wood, D. Woodhouse, J. Woodruff, D. T. Woods, S. Woods, B. N. Woodworth, E. Wooten, A. Wootton, K. Work, J. B. Workman, J. Wright, M. Wu, C. Wuest, F. J. Wysocki, H. Xu, M. Yamaguchi, B. Yang, S. T. Yang, J. Yatabe, C. B. Yeamans, B. C. Yee, S. A. Yi, L. Yin, B. Young, C. S. Young, C. V. Young, P. Young, K. Youngblood, J. Yu, R. Zacharias, G. Zagaris, N. Zaitseva, F. Zaka, F. Ze, B. Zeiger, M. Zika, G. B. Zimmerman, T. Zobrist, J. D. Zuegel, and A. B. Zylstra. Achievement of target gain larger than unity in an inertial fusion experiment. *Phys. Rev. Lett.*, 132:065102, Feb 2024.

[6] T. Ditmire, M. Roth, P. K. Patel, D. Callahan, G. Cheriaux, P. Gibbon, D. Hammond, A. Hannasch, L. C. Jarrott, G. Schaumann, W. Theobald, C. Therrot, O. Turianska, X. Vaisseau, F. Wasser, S. Zähter, M. Zimmer, and W. Goldstein. Focused energy, a new approach towards inertial fusion energy. *Journal of Fusion Energy*, 42(2):27, 2023.

[7] Max Tabak, James Hammer, Michael E. Glinsky, William L. Kruer, Scott C. Wilks, John Woodworth, E. Michael Campbell, Michael D. Perry, and Rodney J. Mason. Ignition and high gain with ultrapowerful lasers*. *Physics of Plasmas*, 1(5):1626–1634, 1994.

[8] V. Yu Bychenkov, W. Rozmus, A. Maksimchuk, D. Umstadter, and C. E. Capjack. Fast ignitor concept with light ions. *Plasma Physics Reports*, 27(12):1017–1020, 2001.

[9] J. J. Honrubia, J. C. Fernández, M. Temporal, B. M. Hegelich, and J. Meyer-ter Vehn. Fast ignition of inertial fusion targets by laser-driven carbon beams. *Physics of Plasmas*, 16(10), 2009.

[10] J. J. Honrubia and M. Murakami. Ion beam requirements for fast ignition of inertial fusion targets. *Physics of Plasmas*, 22(1), 2015.

[11] J. J. Honrubia, J. C. Fernández, B. M. Hegelich, M. Murakami, and C. D. Enriquez. Fast ignition driven by quasi-monoenergetic ions: Optimal ion type and reduction of ignition energies with an ion beam array. *Laser and Particle Beams*, 32(3):419–427, 2014.

[12] J. C. Fernández, B. J. Albright, F. N. Beg, M. E. Foord, B. M. Hegelich, J. J. Honrubia, M. Roth, R. B. Stephens, and L. Yin. Fast ignition with laser-driven proton and ion beams. *Nuclear Fusion*, 54(5), 2014.

[13] M. Roth, T. E. Cowan, M. H. Key, S. P. Hatchett, C. Brown, W. Fountain, J. Johnson, D. M. Pennington, R. A. Snavely, S. C. Wilks, K. Yasuike, H. Ruhl, F. Pegoraro, S. V. Bulanov, E. M. Campbell, M. D. Perry, and H. Powell. Fast ignition by intense laser-accelerated proton beams. *Physical Review Letters*, 86(3):436–439, 2001.

[14] M. Chen, A. Pukhov, T. P. Yu, and Z. M. Sheng. Enhanced collimated gev monoenergetic ion acceleration from a shaped foil target irradiated by a circularly polarized laser pulse. *Phys Rev Lett*, 103(2):024801, 2009.

[15] D. Khaghani, M. Lobet, B. Borm, L. Burr, F. Gartner, L. Gremillet, L. Movsesyan, O. Rosmej, M. E. Toimil-Molares, F. Wagner, and P. Neumayer. Enhancing laser-driven proton acceleration by using micro-pillar arrays at high drive energy. *Sci Rep*, 7(1):11366, 2017.

[16] G. Cantono, A. Permogorov, J. Ferri, E. Smetanina, A. Dmitriev, A. Persson, T. Fulop, and C. G. Wahlstrom. Laser-driven proton acceleration from ultrathin foils with nanoholes. *Sci Rep*, 11(1):5006, 2021.

[17] T. Wang, V. Khudik, and G. Shvets. Laser-ion lens and accelerator. *Phys Rev Lett*, 126(2):024801, 2021.

[18] Jubaraj Choudhury, Ankita Bhagawati, Jyotirup Sarma, and Nilakshi Das. Ion acceleration from a multispecies nanostructured target using a high-intensity laser: a simulation study. *Plasma Physics and Controlled Fusion*, 65(8), 2023.

[19] Imran Khan and Vikrant Saxena. Enhanced target normal sheath acceleration with a grooved hydrocarbon target. *Physics of Plasmas*, 30(6), 2023.

[20] Xiaofei Shen, Zheng Gong, Karen Z. Hatsagortsyan, and Christoph H. Keitel. Highly polarized energetic electrons via intense laser-irradiated tailored targets. *Physical Review Research*, 6(3), 2024.

[21] M. Tosca, A. Morace, M. Schollmeier, S. Steinke, V. Shirvanyan, Y. Arikawa, L. Giuffrida, D. Margarone, P. Pleskunov, A. Choukourov, R. R. Whitney, L. R. Scammell, and G. Korn. Enhanced laser absorption and ion acceleration by boron nitride nanotube targets and high-energy pw laser pulses. *Physical Review Research*, 6(2), 2024.

[22] Ursula Keller and R Paschotta. *Ultrafast lasers*. Springer, 2021.

[23] *Dispersion and Dispersion Compensation*, chapter 4, pages 147–197. John Wiley & Sons, Ltd, 2009.

[24] O. Martinez. 3000 times grating compressor with positive group velocity dispersion: Application to fiber compensation in 1.3-1.6 µm region. *IEEE Journal of Quantum Electronics*, 23(1):59–64, 1987.

[25] E. Treacy. Optical pulse compression with diffraction gratings. *IEEE Journal of Quantum Electronics*, 5(9):454–458, 1969.

[26] Joseph W. Goodman. *Introduction to Fourier Optics*. McGraw-Hill Book Company, Inc., 1988.

[27] David G. Voelz. *Computational Fourier Optics: A MATLAB Tutorial*. SPIE, January 2011.

[28] L. Bluestein. A linear filtering approach to the computation of discrete fourier transform. *IEEE Transactions on Audio and Electroacoustics*, 18(4):451–455, 1970.

[29] L Rabiner, R W Schafer, and C Rader. The chirp z-transform algorithm. *IEEE transactions on audio and electroacoustics*, 17(2):86–92, 1969.

[30] Y. Hu, Z. Wang, X. Wang, S. Ji, C. Zhang, J. Li, W. Zhu, D. Wu, and J. Chu. Efficient full-path optical calculation of scalar and vector diffraction using the bluestein method. *Light Sci Appl*, 9:119, 2020.

[31] J. Derouillat, A. Beck, F. Pérez, T. Vinci, M. Chiaramello, A. Grassi, M. Flé, G. Bouchard, I. Plotnikov, N. Aunai, J. Dargent, C. Riconda, and M. Grech. Smilei : A collaborative, open-source, multi-purpose particle-in-cell code for plasma simulation. *Computer Physics Communications*, 222:351–373, 2018.

[32] Allen Taflove, Susan C. Hagness, and Melinda Piket-May. 9 - computational electromagnetics: The finite-difference time-domain method. In WAI-KAI CHEN, editor, *The Electrical Engineering Handbook*, pages 629–670. Academic Press, Burlington, 2005.

[33] Kane Yee. Numerical solution of initial boundary value problems involving maxwell's equations in isotropic media. *IEEE Transactions on Antennas and Propagation*, 14(3):302–307, 1966.

[34] P. Mora. Plasma expansion into a vacuum. *Phys. Rev. Lett.*, 90:185002, May 2003.

[35] S. C. Wilks, A. B. Langdon, T. E. Cowan, M. Roth, M. Singh, S. Hatchett, M. H. Key, D. Pennington, A. MacKinnon, and R. A. Snavely. Energetic proton generation in ultra-intense laser–solid interactions. *Physics of Plasmas*, 8(2):542–549, 2001.

[36] K. Nishihara, H. Amitani, M. Murakami, S. V. Bulanov, and T. Zh Esirkepov. High energy ions generated by laser driven coulomb explosion of cluster. *Nuclear Instruments and Methods in Physics Research Section A: Accelerators, Spectrometers, Detectors and Associated Equipment*, 464(1):98–102, 2001.

[37] Andrea Macchi and Carlo Benedetti. Ion acceleration by radiation pressure in thin and thick targets. *Nuclear Instruments and Methods in Physics Research Section A: Accelerators, Spectrometers, Detectors and Associated Equipment*, 620(1):41–45, 2010.

[38] A. Macchi, F. Cattani, T. V. Liseykina, and F. Cornolti. Laser acceleration of ion bunches at the front surface of overdense plasmas. *Phys Rev Lett*, 94(16):165003, 2005.

[39] Andrea Macchi, Silvia Veghini, Tatyana V. Liseykina, and Francesco Pegoraro. Radiation pressure acceleration of ultrathin foils. *New Journal of Physics*, 12(4), 2010.

[40] A. Macchi, S. Veghini, and F. Pegoraro. "light sail" acceleration reexamined. *Phys Rev Lett*, 103(8):085003, 2009.

[41] L. Yin, B. J. Albright, B. M. Hegelich, K. J. Bowers, K. A. Flippo, T. J. T. Kwan, and J. C. Fernández. Monoenergetic and gev ion acceleration from the laser breakout afterburner using ultrathin targets. *Physics of Plasmas*, 14(5), 2007.

[42] S. Guérin, P. Mora, J. C. Adam, A. Héron, and G. Laval. Propagation of ultraintense laser pulses through overdense plasma layers. *Physics of Plasmas*, 3(7):2693–2701, 1996.

[43] L. Willingale, S. R. Nagel, A. G. Thomas, C. Bellei, R. J. Clarke, A. E. Dangor, R. Heathcote, M. C. Kaluza, C. Kamperidis, S. Kneip, K. Krushelnick, N. Lopes, S. P. Mangles, W. Nazarov, P. M. Nilson, and Z. Najmudin. Characterization of high-intensity laser propagation in the relativistic transparent regime through measurements of energetic proton beams. *Phys Rev Lett*, 102(12):125002, 2009.

[44] Anthony E. Siegman. *Lasers*. University Science Books, 1986.

[45] Christopher P. J. Barty. Optical chirped beam amplification and propagation. *U.S. patent 6,804,045B2*, (6,804,045), October 12, 2004.

[46] C. P. J. Barty. The nexawatt: A strategy for exawatt peak power lasers based on NIF and NIF-like beam lines. *Journal of Physics: Conference Series*, 717(1):012086, 2016.

[47] K. D. Chesnut and C. P. J. Barty. Ideal spatio-temporal pulse distribution for exawatt-scale lasers based on simultaneous chirped beam and chirped pulse amplification. *Optics Express*, 31(4):5687–5698, 2023.

[48] Guanghao Zhu, James van Howe, Michael Durst, Warren Zipfel, and Chris Xu. Simultaneous spatial and temporal focusing of femtosecond pulses. *Optics Express*, 13(6):2153–2159, 2005.

[49] Charles G. Durfee, Michael Greco, Erica Block, Dawn Vitek, and Jeff A. Squier. Intuitive analysis of space-time focusing with double-ABCD calculation. *Optics Express*, 20(13):14244–14259, 2012.

[50] Dan Oron, Eran Tal, and Yaron Silberberg. Scanningless depth-resolved microscopy. *Optics Express*, 13(5):1468–1476, 2005.

[51] Michael E. Durst, Guanghao Zhu, and Chris Xu. Simultaneous spatial and temporal focusing for axial scanning. *Optics Express*, 14(25):12243–12254, 2006.

[52] Eirini Papagiakoumou, Emiliano Ronzitti, and Valentina Emiliani. Scanless two-photon excitation with temporal focusing. *Nature Methods*, 17(6):571–581, 2020.

[53] Dawn N. Vitek, Erica Block, Yves Bellouard, Daniel E. Adams, Sterling Backus, David Kleinfeld, Charles G. Durfee, and Jeffrey A. Squier. Spatio-temporally focused femtosecond laser pulses for nonreciprocal writing in optically transparent materials. *Optics Express*, 18(24):24673–24678, 2010.

[54] Robert Kammel, Roland Ackermann, Jens Thomas, Jörg Götte, Stefan Skupin, Andreas Tünnermann, and Stefan Nolte. Enhancing precision in fs-laser material processing by simultaneous spatial and temporal focusing. *Light: Science & Applications*, 3(5):e169–e169, 2014.

[55] Aabid Patel, Yuri Svirko, Charles Durfee, and Peter G. Kazansky. Direct writing with tilted-front femtosecond pulses. *Scientific Reports*, 7(1):12928, 2017.

[56] Yuanxin Tan, Wei Chu, Peng Wang, Wenbo Li, Jia Qi, Jian Xu, Zhanshan Wang, and Ya Cheng. High-throughput multi-resolution three dimensional laser printing. *Physica Scripta*, 94(1):015501, 2018.

[57] Alex M. Wilhelm and Charles G. Durfee. Tilted snowplow ponderomotive electron acceleration with spatio-temporally shaped ultrafast laser pulses. *Frontiers in Physics*, 7(66), 2019.

[58] Patrick Hunt, Alex Wilhelm, Daniel Adams, Shoujun Wang, Reed Hollinger, Ze'ev Shpilman, Sina Anaraki, Nathaniel Westlake, David Schmidt, Jorge Rocca, and Charles Durfee. Ponderomotive snowplow electron acceleration with high energy tilted ultrafast laser pulses (preprint). *Research Square*, 2024.

[59] E. S. Grace, B. Z. Djordjevic, Z. Guang, D. Mariscal, G. G. Scott, R. A. Simpson, K. K. Swanson, G. Zeraouli, B. Stuart, R. Trebino, and T. Ma. Single-shot measurements of pulse-front tilt in intense ps laser pulses and its effect on accelerated electron and ion beam characteristics (invited). *Rev Sci Instrum*, 93(12):123508, 2022.

[60] Z. Li, Y. Kato, and J. Kawanaka. Simulating an ultra-broadband concept for exawatt-class lasers. *Sci Rep*, 11(1):151, 2021.

[61] Wenhai Liang, Shuman Du, Renjing Chen, Xinliang Wang, Xingyan Liu, Xun Chen, Xiong Shen, Jun Liu, and Ruxin Li. Viability verification of asymmetric four-grating compressor in sel-100 PW frontend. *Optics Communications*, 557, 2024.

[62] M. Aléonard, M. Altarelli, Patrizio Antici, Alexander Apolonskiy, Patrick Audebert, Andrzej Bartnik, C. Barty, A. Bernstein, Jens Biegert, P. Böni, Nicola Booth, D. Bote, Sergei Bulanov, Rytis Butkus, Luis Cardoso, J. P. Chambaret, D. Charambilidis, G. Cheriaux, R. Clarke, and Matt Zepf. *WHITEBOOK ELI – Extreme Light Infrastructure; Science and Technology with Ultra-Intense Lasers*. Andreas Thoss, 2011.

[63] A. Jeandet, S. W. Jolly, A. Borot, B. Bussiere, P. Dumont, J. Gautier, O. Gobert, J. P. Goddet, A. Gonsalves, A. Irman, W. P. Leemans, R. Lopez-Martens, G. Mennerat, K. Nakamura, M. Ouille, G. Pariente, M. Pittman, T. Puschel, F. Sanson, F. Sylla, C. Thaury, K. Zeil, and F. Quere. Survey of spatio-temporal couplings throughout high-power ultrashort lasers. *Opt Express*, 30(3):3262–3288, 2022.

[64] Zs Bor, S. Szatmári, and Alexander Müller. Picosecond pulse shortening by travelling wave amplified spontaneous emission. *Applied Physics B*, 32(3):101–104, 1983.

[65] C. P. J. Barty, D. A. King, G. Y. Yin, K. H. Hahn, J. E. Field, J. F. Young, and S. E. Harris. 12.8-ev laser in neutral cesium. *Physical Review Letters*, 61(19):2201–2204, 1988.

[66] Jun Liu, Xiong Shen, Shuman Du, and Ruxin Li. Multistep pulse compressor for 10s to 100s PW lasers. *Optics Express*, 29(11):17140–17158, 2021.

[67] M. Pessot, P. Maine, and G. Mourou. 1000 times expansion/compression of optical pulses for chirped pulse amplification. *Optics Communications*, 62(6):419–421, 1987.

[68] Tae Jun Yu, Seong Ku Lee, Jae Hee Sung, Jin Woo Yoon, Tae Moon Jeong, and Jongmin Lee. Generation of high-contrast, 30 fs, 1.5 PW laser pulses from chirped-pulse amplification ti:sapphire laser. *Optics Express*, 20(10):10807–10815, 2012.

[69] V. Aleksandrov, G. Bleotu, L. Caratas, Razvan Dabu, Ioan Dancus, Riccardo Fabbri, Vicentiu Iancu, Miklos Kiss, A. Lachapelle, Lazar Alexandru, Masruri Masruri, D. Matei, M. Merisanu, Vinod Mohanan, A. Naziru, D. Nistor, Radu Secareanu, Anda-Maria Talposi, A. Toader, and Bogdan-Constantin Ispas. Upgrading design of a multi-tw femtosecond laser. *Romanian Reports in Physics*, 72, 2020.

[70] Y. Chu, Z. Gan, X. Liang, L. Yu, X. Lu, C. Wang, X. Wang, L. Xu, H. Lu, D. Yin, Y. Leng, R. Li, and Z. Xu. High-energy large-aperture ti:sapphire amplifier for 5 PW laser pulses. *Opt Lett*, 40(21):5011–4, 2015.

[71] C. M. Werle, C. Braun, T. Eichner, T. Hulsenbusch, G. Palmer, and A. R. Maier. Out-of-plane multilayer-dielectric-grating compressor for ultrafast ti:sapphire pulses. *Opt Express*, 31(23):37437–37451, 2023.

[72] François Lureau, Guillaume Matras, Olivier Chalus, Christophe Derycke, Thomas Morbieu, Christophe Radier, Olivier Casagrande, Sébastien Laux, Sandrine Ricaud, Gilles Rey, Alain Pellegrina, Caroline Richard, Laurent Boudjemaa, Christophe Simon-Boisson, Andrei Baleanu, Romeo Banici, Andrei Gradinariu, Constantin Caldararu, Bertrand De Boisdeffre, Petru Ghenuche, Andrei Naziru, Georgios Kolliopoulos, Liviu Neagu, Razvan Dabu, Ioan Dancus, and Daniel Ursescu. High-energy hybrid femtosecond laser system demonstrating 2×10 pw capability. *High Power Laser Science and Engineering*, 8, 2020.

[73] Robert Kammel, Klaus Bergner, Jens Thomas, Roland Ackermann, Stefan Skupin, and Stefan Nolte. *Simultaneous spatial and temporal focusing: a route towards confined nonlinear materials processing*, volume 9736 of *SPIE LASE*. SPIE, 2016.

[74] Fei He, Ya Cheng, Jintian Lin, Jielei Ni, Zhizhan Xu, Koji Sugioka, and Katsumi Midorikawa. Independent control of aspect ratios in the axial and lateral cross sections of a focal spot for three-dimensional femtosecond laser micromachining. *New Journal of Physics*, 13(8), 2011.

[75] Site Zhang, Daniel Asoubar, Robert Kammel, Stefan Nolte, and Frank Wyrowski. Analysis of pulse front tilt in simultaneous spatial and temporal focusing. *Journal of the Optical Society of America A*, 31(11):2437–2446, 2014.

[76] Alex Matthew Wilhelm. *Tilted Snowplow Electron Acceleration with Simultaneously Spatially and Temporally Focused Laser Pulses*. Ph.d., Colorado School of Mines, 2021.

[77] Y. Han, Z. Li, Y. Zhang, F. Kong, H. Cao, Y. Jin, Y. Leng, R. Li, and J. Shao. 400nm ultra-broadband gratings for near-single-cycle 100 petawatt lasers. *Nat Commun*, 14(1):3632, 2023.

[78] Jacob R. Pierce, John P. Palastro, Fei Li, Bernardo Malaca, Dillon Ramsey, Jorge Vieira, Kathleen Weichman, and Warren B. Mori. Arbitrarily structured laser pulses. *Physical Review Research*, 5(1), 2023.

[79] Z. Che, W. Liu, J. Ye, L. Shi, C. T. Chan, and J. Zi. Generation of spatiotemporal vortex pulses by resonant diffractive grating. *Phys Rev Lett*, 132(4):044001, 2024.

[80] Qiwen Zhan. Spatiotemporal sculpturing of light: a tutorial. *Advances in Optics and Photonics*, 16(2), 2024.

[81] Bangshan Sun, Patrick S. Salter, Clemens Roider, Alexander Jesacher, Johannes Strauss, Johannes Heberle, Michael Schmidt, and Martin J. Booth. Four-dimensional light shaping: manipulating ultrafast spatiotemporal foci in space and time. *Light: Science & Applications*, 7(1):17117–17117, 2018.

[82] Murat Yessenov, Justin Free, Zhaozhong Chen, Eric G. Johnson, Martin P. J. Lavery, Miguel A. Alonso, and Ayman F. Abouraddy. Space-time wave packets localized in all dimensions. *Nature Communications*, 13(1):4573, 2022.

[83] Selcuk Akturk, Xun Gu, Pamela Bowlan, and Rick Trebino. Spatio-temporal couplings in ultrashort laser pulses. *Journal of Optics*, 12(9):093001, 2010.

[84] Qiyuan Song, Aoi Nakamura, Kenichi Hirosawa, Keisuke Isobe, Katsumi Midorikawa, and Fumihiko Kannari. Two-dimensional spatiotemporal focusing of femtosecond pulses and its applications in microscopy. *Review of Scientific Instruments*, 86(8):083701, 2015.

[85] M. Clerici, D. Faccio, E. Rubino, A. Lotti, A. Couairon, and P. Di Trapani. Space–time focusing of bessel-like pulses. *Optics Letters*, 35(19):3267–3269, 2010.

[86] Dustin H. Froula, David Turnbull, Andrew S. Davies, Terrance J. Kessler, Dan Haberberger, John P. Palastro, Seung-Whan Bahk, Ildar A. Begishev, Robert Boni, Sara Bucht, Joseph Katz, and Jessica L. Shaw. Spatiotemporal control of laser intensity. *Nature Photonics*, 12(5):262–265, 2018.

[87] A. Liberman, R. Lahaye, S. Smartsev, S. Tata, S. Benracassa, A. Golovanov, E. Levine, C. Thaury, and V. Malka. Use of spatiotemporal couplings and an axiparabola to control the velocity of peak intensity. *Opt Lett*, 49(4):814–817, 2024.

[88] Thomas E. Lanier and Jeremy R. Gulley. Nonlinear space-time focusing and filamentation of annular femtosecond pulses in dielectrics. *Journal of the Optical Society of America B*, 33(2):292–301, 2016.

[89] Spencer Jolly and Miguel Porras. Analytical fields of an ultrashort, radially polarized laser with spatial chirp. *Journal of the Optical Society of America B*, 2024.

[90] James Dyson. Circular and spiral diffraction gratings. *Proceedings of the Royal Society of London. Series A. Mathematical and Physical Sciences*, 248(1252):93–106, 1958.

[91] Christian Vetter, Ralf Steinkopf, Klaus Bergner, Marco Ornigotti, Stefan Nolte, Herbert Gross, and Alexander Szameit. Realization of free-space long-distance self-healing bessel beams. *Laser & Photonics Reviews*, 13(10), 2019.

[92] Erica Block, Michael Greco, Dawn Vitek, Omid Masihzadeh, David A. Ammar, Malik Y. Kahook, Naresh Mandava, Charles Durfee, and Jeff Squier. Simultaneous spatial and temporal focusing for tissue ablation. *Biomedical optics express*, 4(6):831–841, 2013.

[93] Kyoko Kitamura, Kyosuke Sakai, and Susumu Noda. Sub-wavelength focal spot with long depth of focus generated by radially polarized, narrow-width annular beam. *Optics Express*, 18(5):4518–4525, 2010.

[94] Liangxin Yang, Xiangsheng Xie, Sicong Wang, and Jianying Zhou. Minimized spot of annular radially polarized focusing beam. *Optics Letters*, 38(8):1331–1333, 2013.

[95] Jeffrey Powell, Spencer W. Jolly, Simon Vallières, François Fillion-Gourdeau, Stéphane Payeur, Sylvain Fourmaux, Michel Piché, Heide Ibrahim, Steve MacLean, and François Légaré. Relativistic electrons from vacuum laser acceleration using tightly focused radially polarized beams, 2024.

[96] W. L. Kruer and Kent Estabrook. J×b heating by very intense laser light. *The Physics of Fluids*, 28(1):430–432, 1985.

[97] A. Couairon, D. Faccio, and P. Di Trapani. *Conical Waves, Filaments and Nonlinear Filamentation Optics*. Aracne, 2007.

[98] D. J. Stark, L. Yin, B. J. Albright, and F. Guo. Effects of dimensionality on kinetic simulations of laser-ion acceleration in the transparency regime. *Physics of Plasmas*, 24(5), 2017.

[99] J. B. Kim, S. Göde, and S. H. Glenzer. Development of a cryogenic hydrogen microjet for high-intensity, high-repetition rate experiments. *Review of Scientific Instruments*, 87(11), 2016.

[100] Martin Rehwald, Stefan Assenbaum, Constantin Bernert, Florian-Emanuel Brack, Michael Bussmann, Thomas E. Cowan, Chandra B. Curry, Frederico Fiuza, Marco Garten, Lennart Gaus, Maxence Gauthier, Sebastian Göde, Ilja Göthel, Siegfried H. Glenzer, Lingen Huang, Axel Huebl, Jongjin B. Kim, Thomas Kluge, Stephan Kraft, Florian Kroll, Josefine Metzkes-Ng, Thomas Miethlinger, Markus Loeser, Lieselotte Obst-Huebl, Marvin Reimold, Hans-Peter Schlenvoigt, Christopher Schoenwaelder, Ulrich Schramm, Mathias Siebold, Franziska Treffert, Long Yang, Tim Ziegler, and Karl Zeil. Ultra-short pulse laser acceleration of protons to 80 mev from cryogenic hydrogen jets tailored to near-critical density. *Nature Communications*, 14(1):4009, 2023.

Appendix A

Time Evolution of Proton Jets

The proton jets for all cases shown are displayed at various time slices ($t = 350.2\ fs$, $t = 500.4\ fs$, and $t = 650.4\ fs$) to present the evolution of the jet.

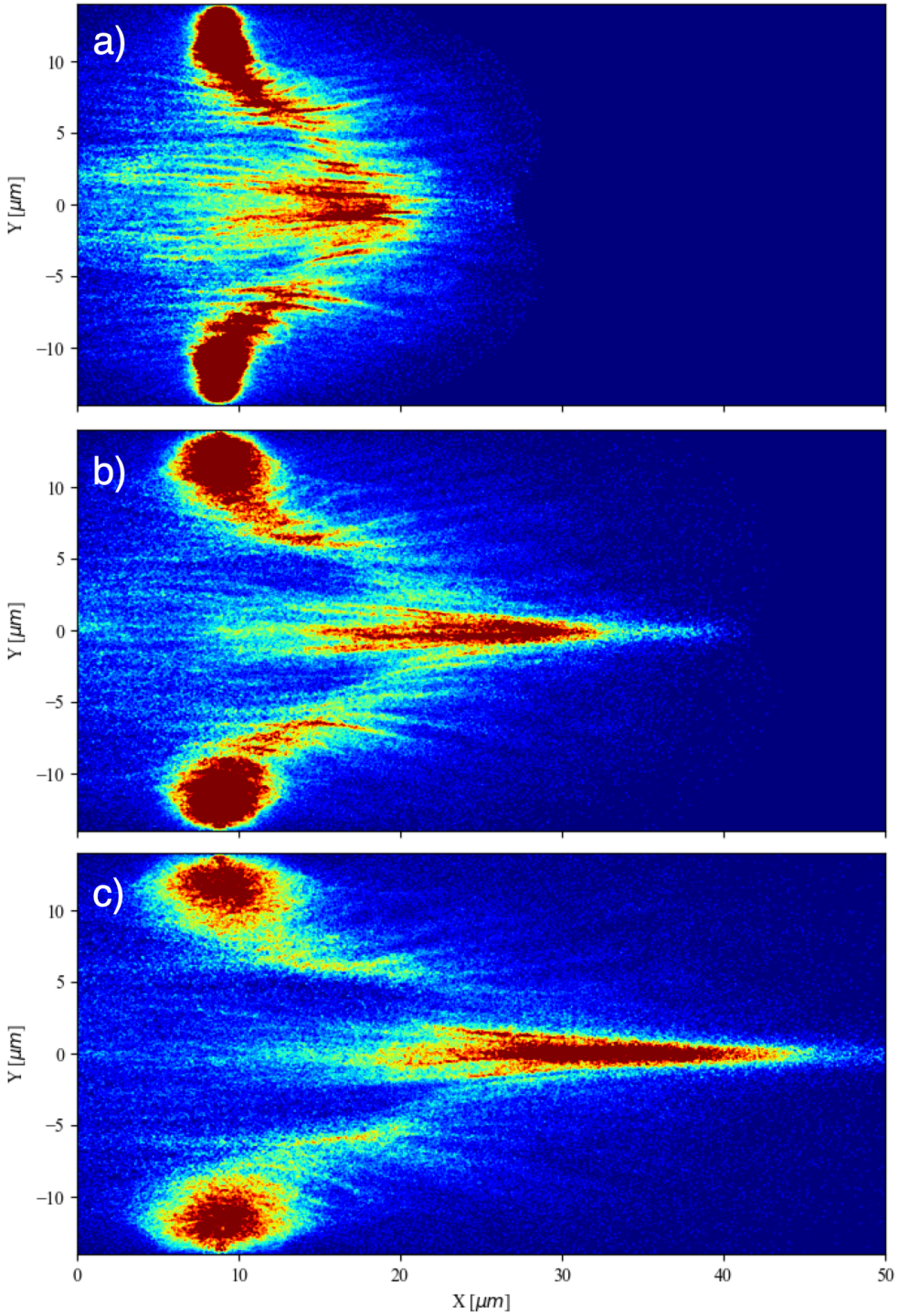

Figure A.1: The accelerated protons for a PFT of 0° shown at a) $t = 350.2\ fs$, b) $t = 500.4\ fs$, and c) $t = 650.4\ fs$

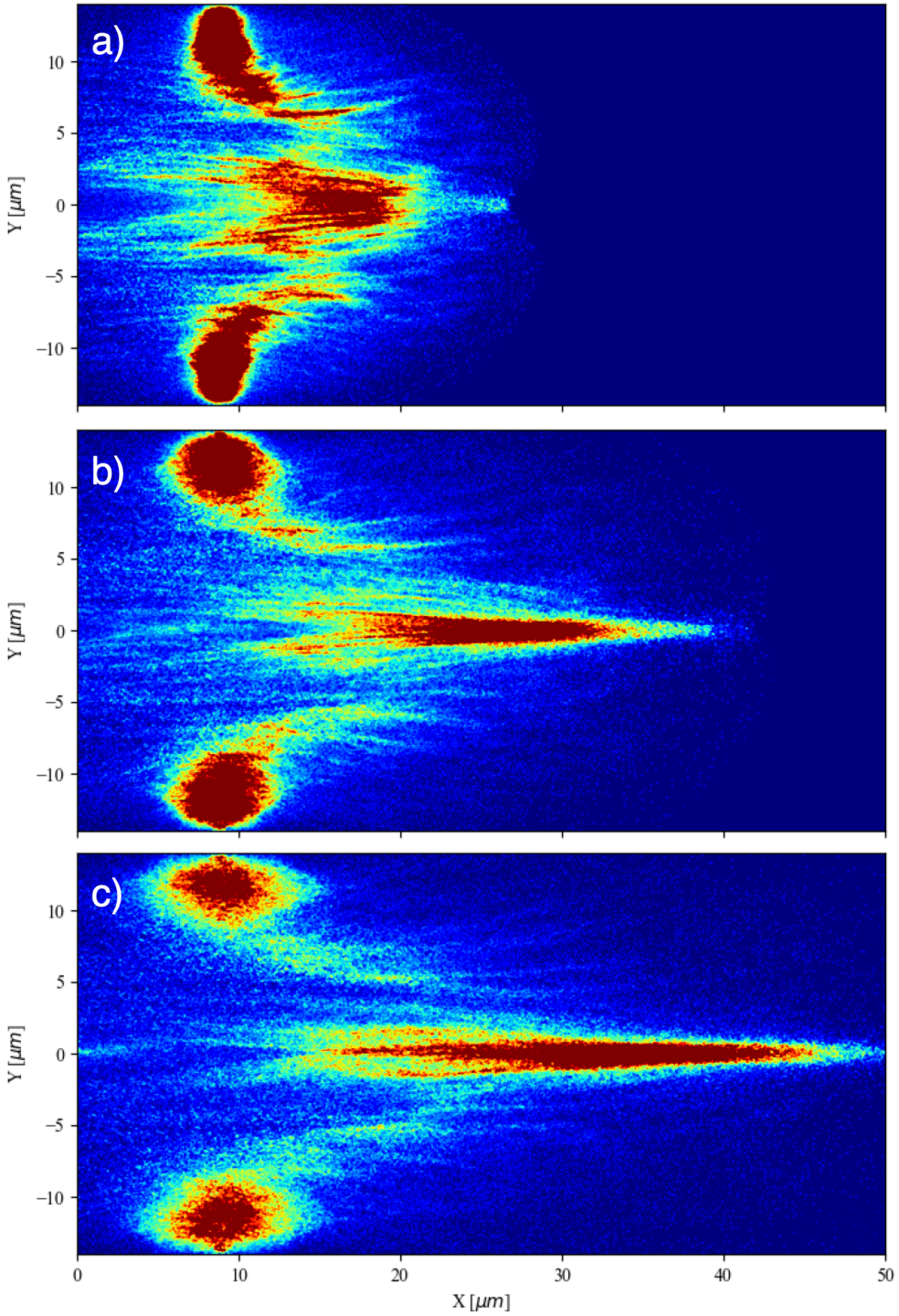

Figure A.2: The accelerated protons for a PFT of 40° shown at a) $t = 350.2\ fs$, b) $t = 500.4\ fs$, and c) $t = 650.4\ fs$

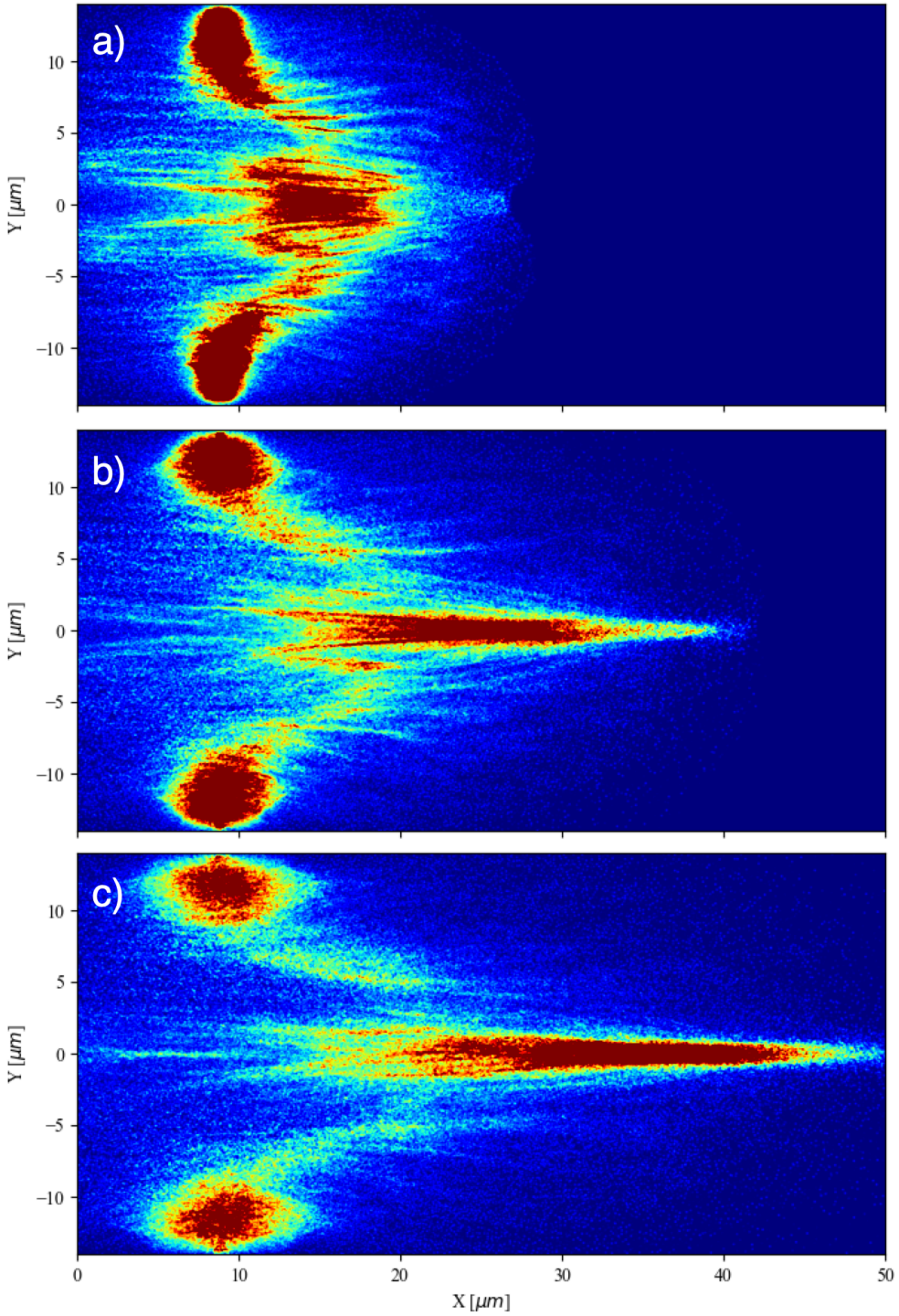

Figure A.3: The accelerated protons for a PFT of 60° shown at a) $t = 350.2\ fs$, b) $t = 500.4\ fs$, and c) $t = 650.4\ fs$

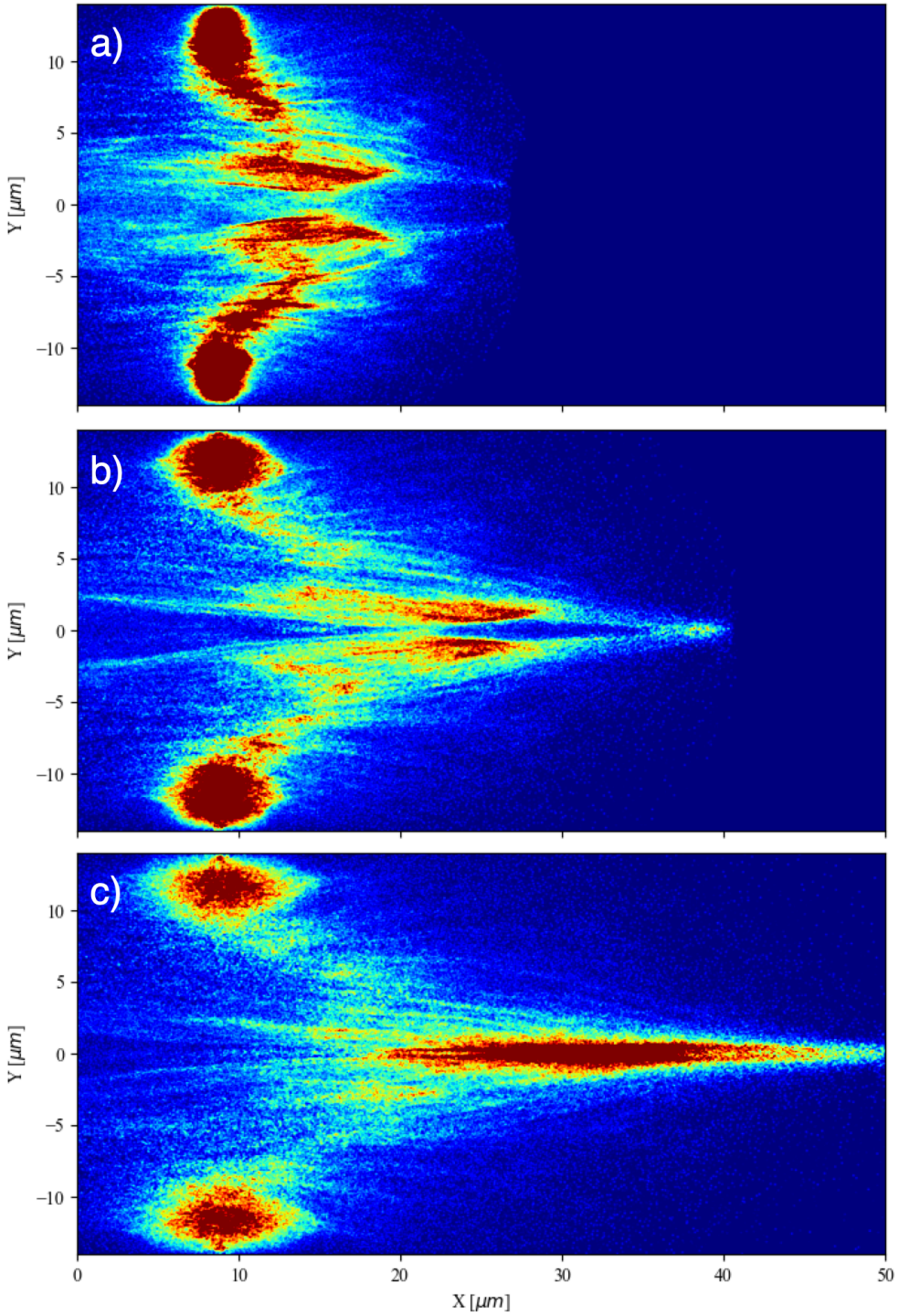

Figure A.4: The accelerated protons for a PFT of 70° shown at a) $t = 350.2\ fs$, b) $t = 500.4\ fs$, and c) $t = 650.4\ fs$

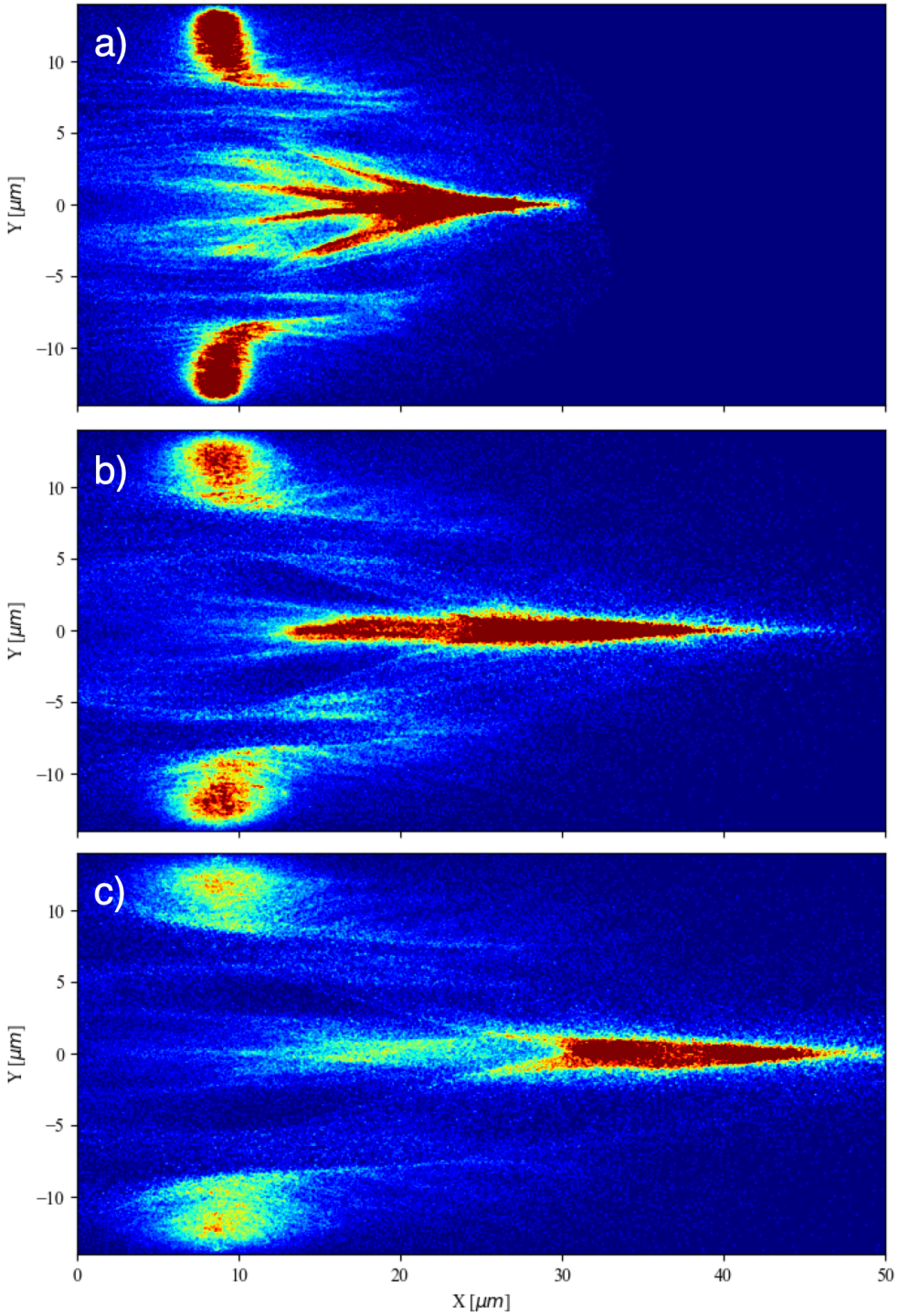

Figure A.5: The accelerated protons for a foil thickness of 400 nm shown at a) $t = 350.2\ fs$, b) $t = 500.4\ fs$, and c) $t = 650.4\ fs$

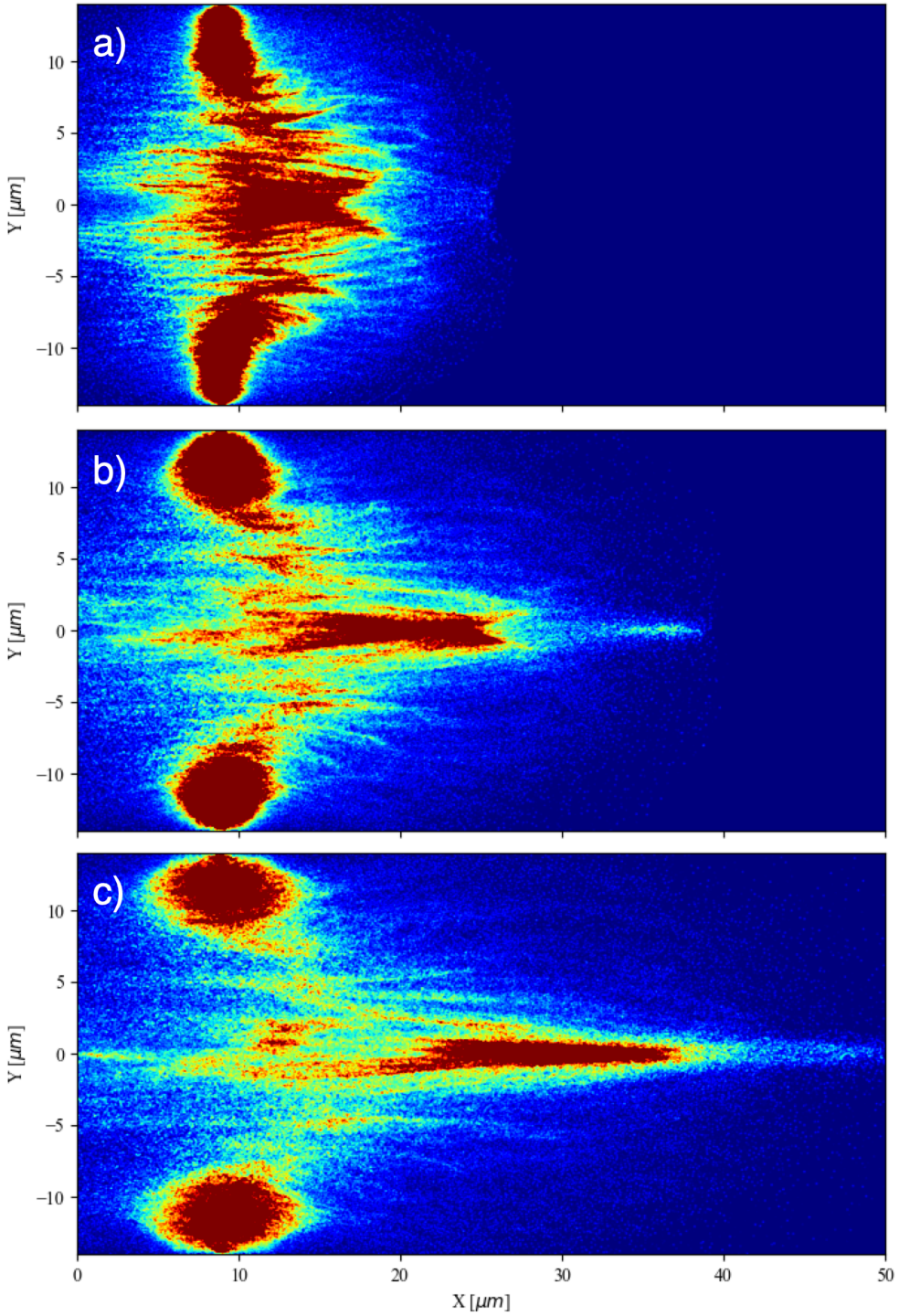

Figure A.6: The accelerated protons for a foil thickness of 800 nm shown at a) $t = 350.2\ fs$, b) $t = 500.4\ fs$, and c) $t = 650.4\ fs$

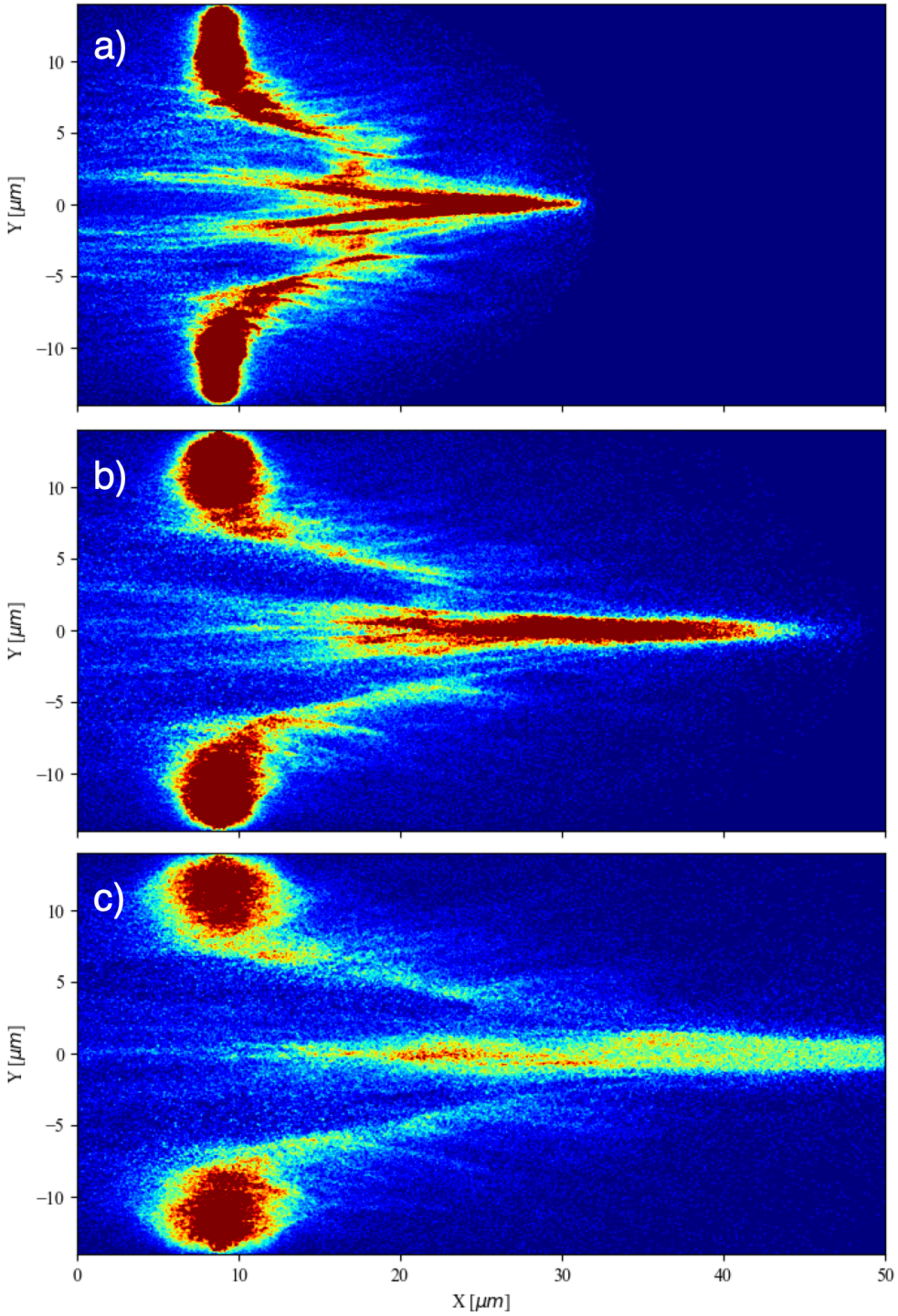

Figure A.7: The accelerated protons for a foil position of 31 μm before the laser focus shown at a) $t = 350.2\ fs$, b) $t = 500.4\ fs$, and c) $t = 650.4\ fs$

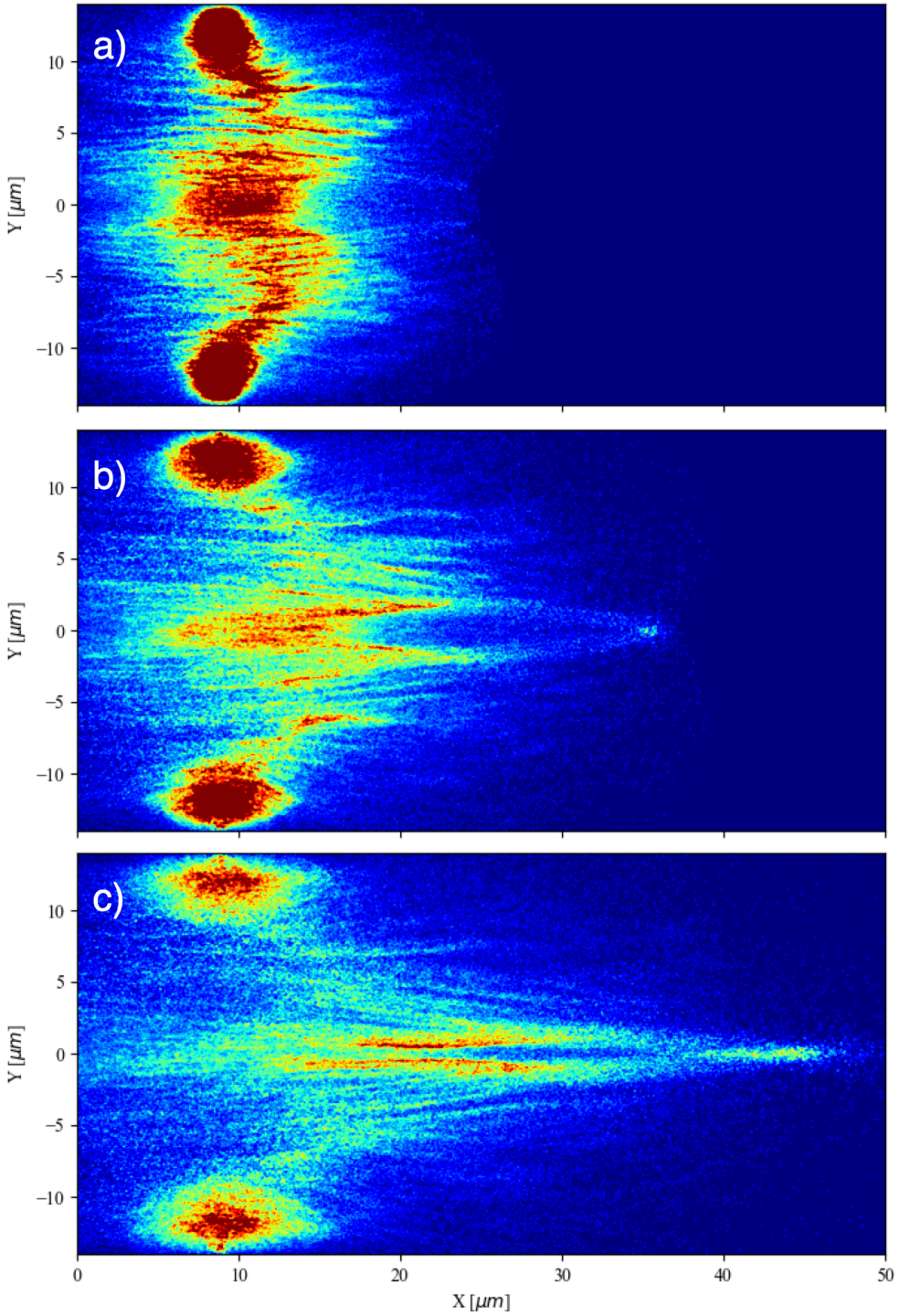

Figure A.8: The accelerated protons for a foil position of 41 μm before the laser focus shown at a) $t = 350.2\ fs$, b) $t = 500.4\ fs$, and c) $t = 650.4\ fs$

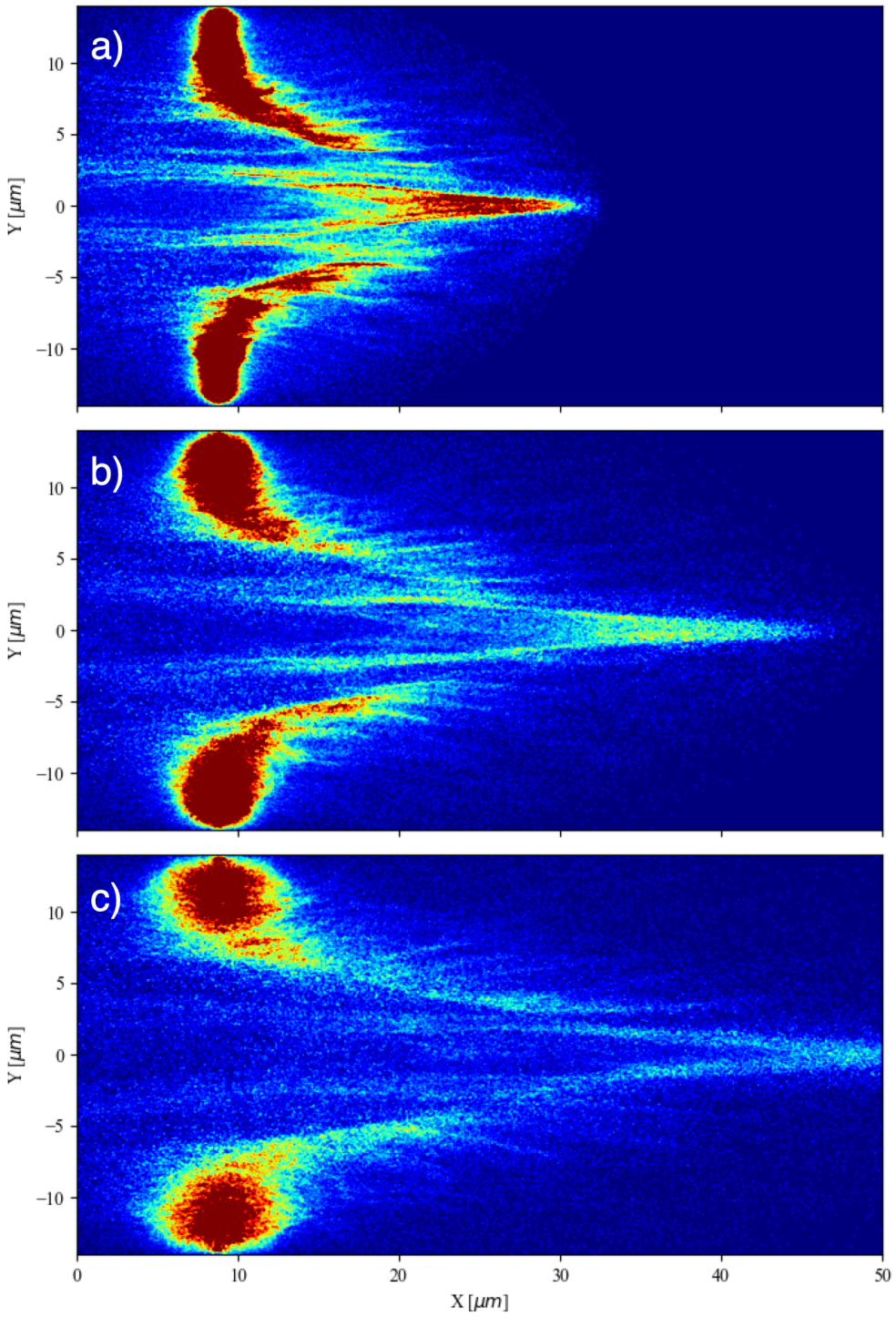

Figure A.9: The accelerated protons for a $\delta r = 2w_{in}$ shown at a) $t = 350.2\ fs$, b) $t = 500.4\ fs$, and c) $t = 650.4\ fs$

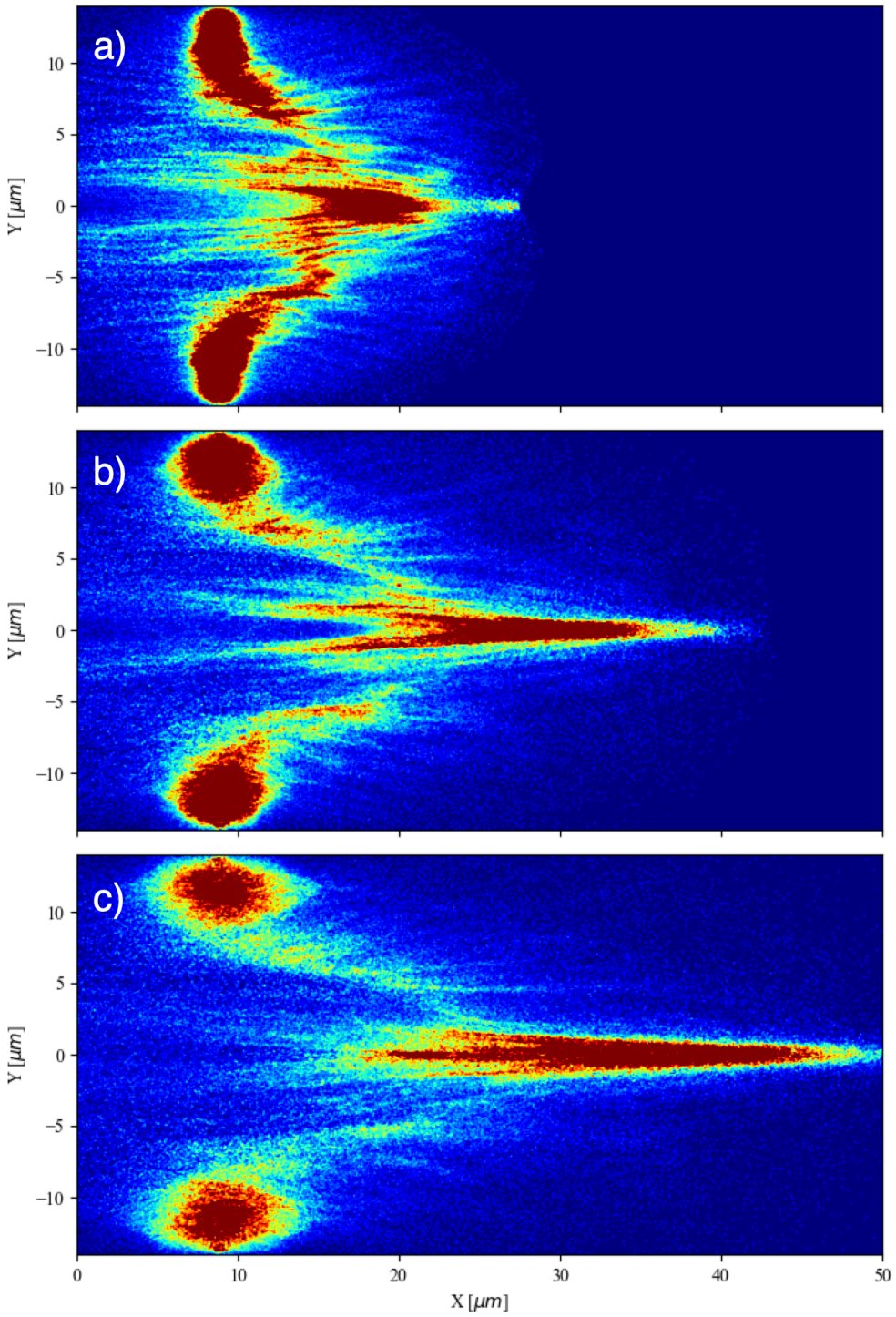

Figure A.10: The accelerated protons for a $\delta r = 2.75 w_{in}$ shown at a) $t = 350.2\ fs$, b) $t = 500.4\ fs$, and c) $t = 650.4\ fs$

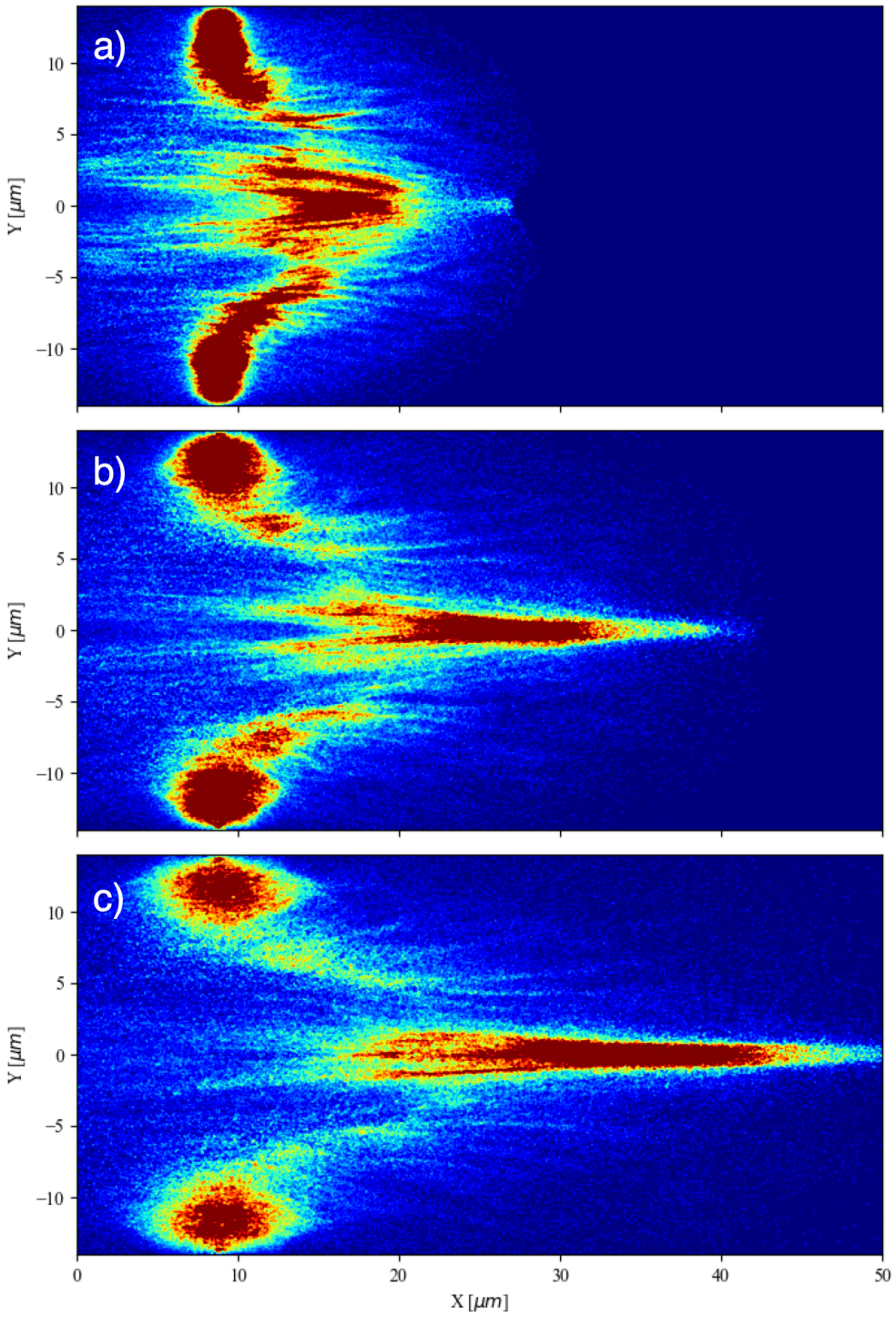

Figure A.11: The accelerated protons for a $\delta r = 2.9 w_{in}$ shown at a) $t = 350.2\ fs$, b) $t = 500.4\ fs$, and c) $t = 650.4\ fs$

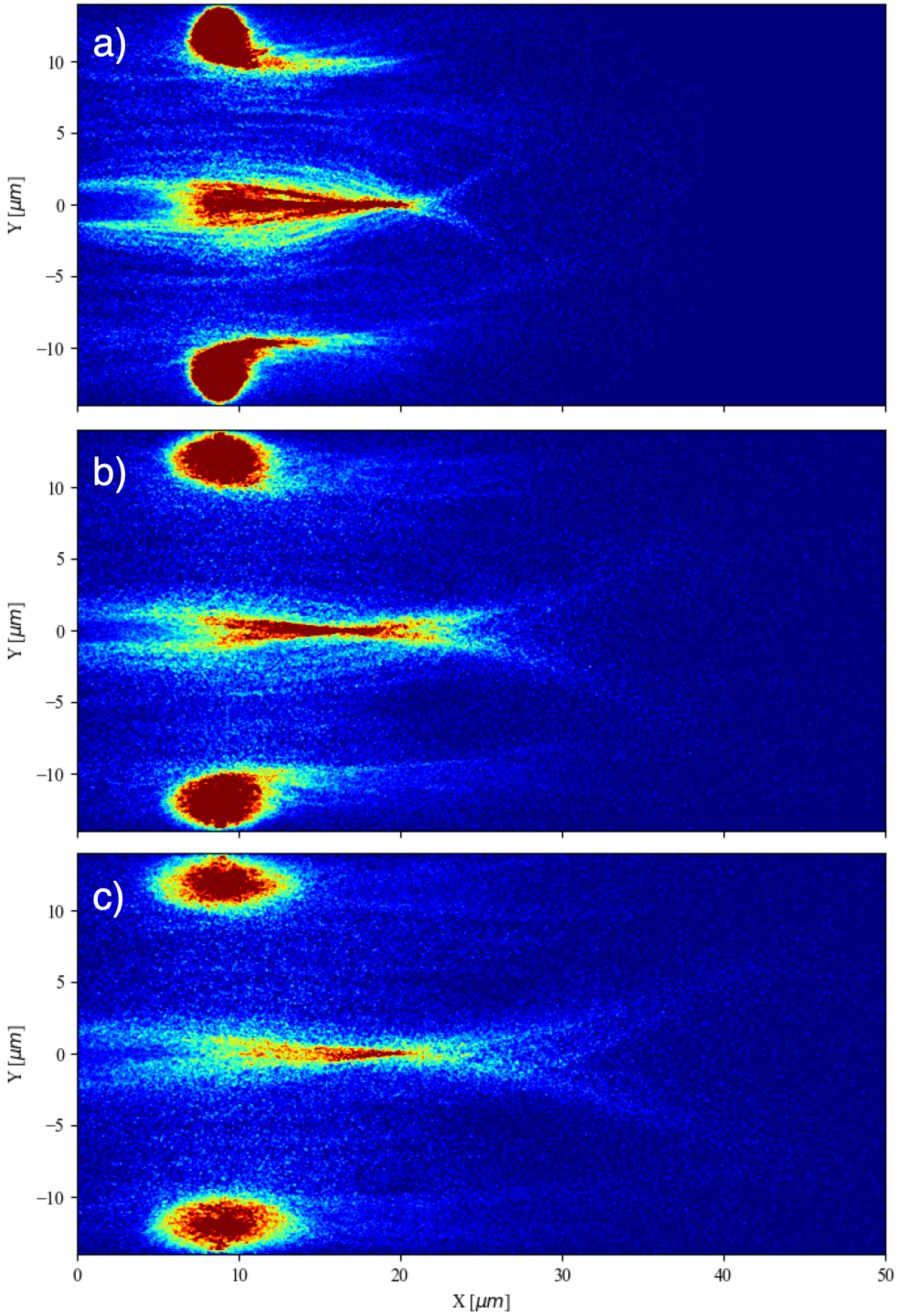

Figure A.12: The accelerated protons for a 2 beam approximation of a PFT 60° shown at a) $t = 350.2\ fs$, b) $t = 500.4\ fs$, and c) $t = 650.4\ fs$

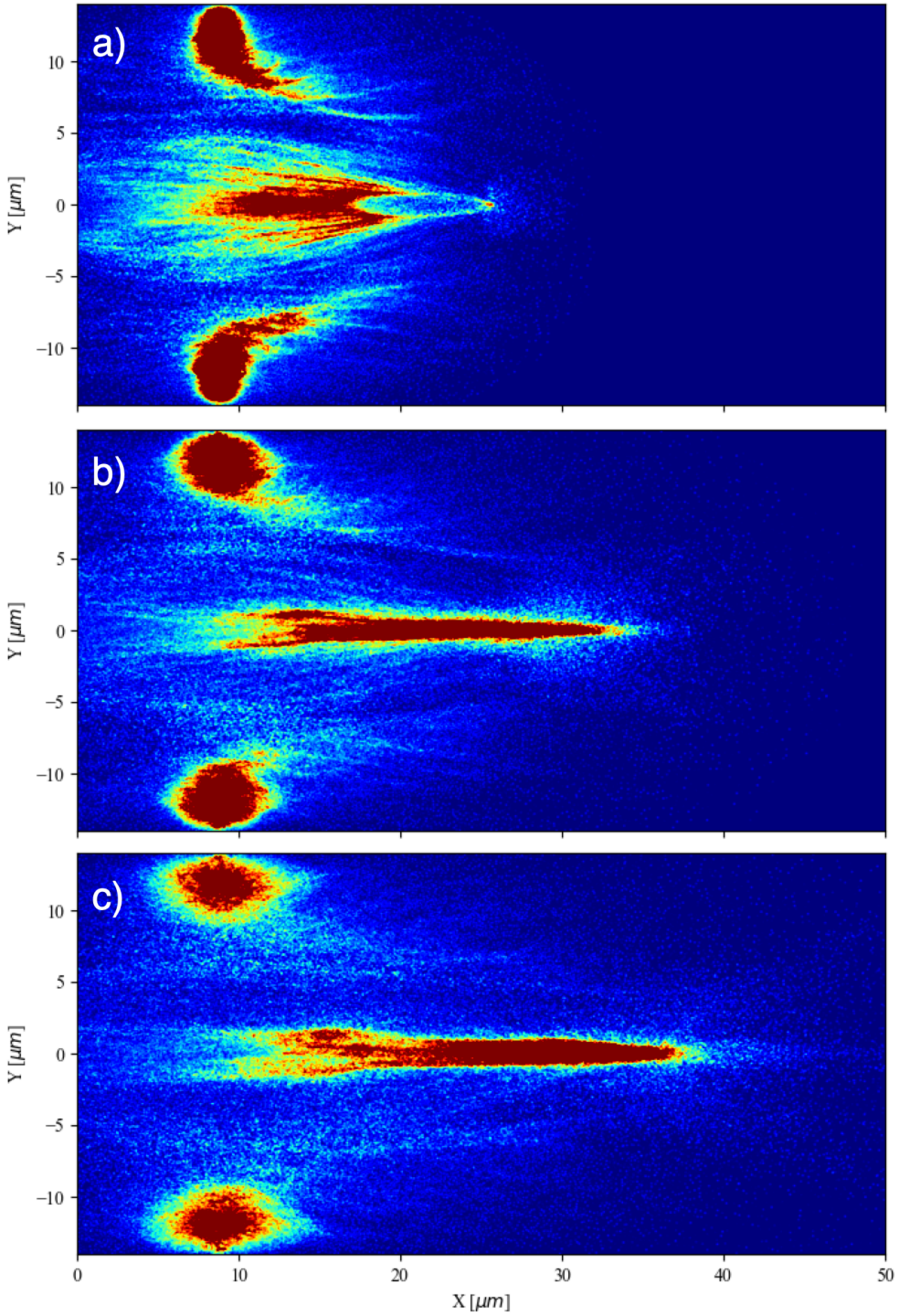

Figure A.13: The accelerated protons for a 4 beam approximation of a PFT 60° shown at a) $t = 350.2\ fs$, b) $t = 500.4\ fs$, and c) $t = 650.4\ fs$

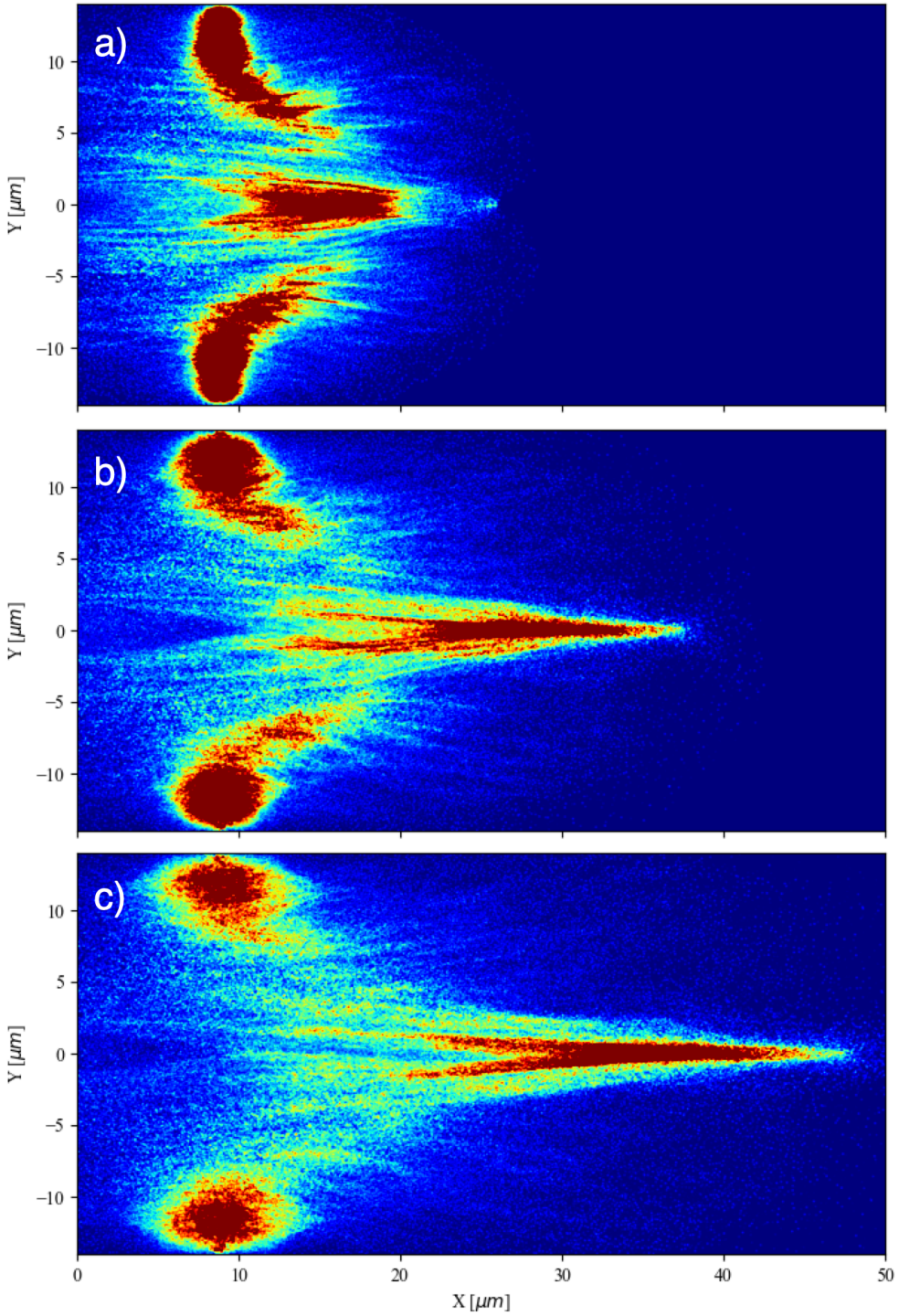

Figure A.14: The accelerated protons for a 6 beam approximation of a PFT 60° shown at a) $t = 350.2\ fs$, b) $t = 500.4\ fs$, and c) $t = 650.4\ fs$

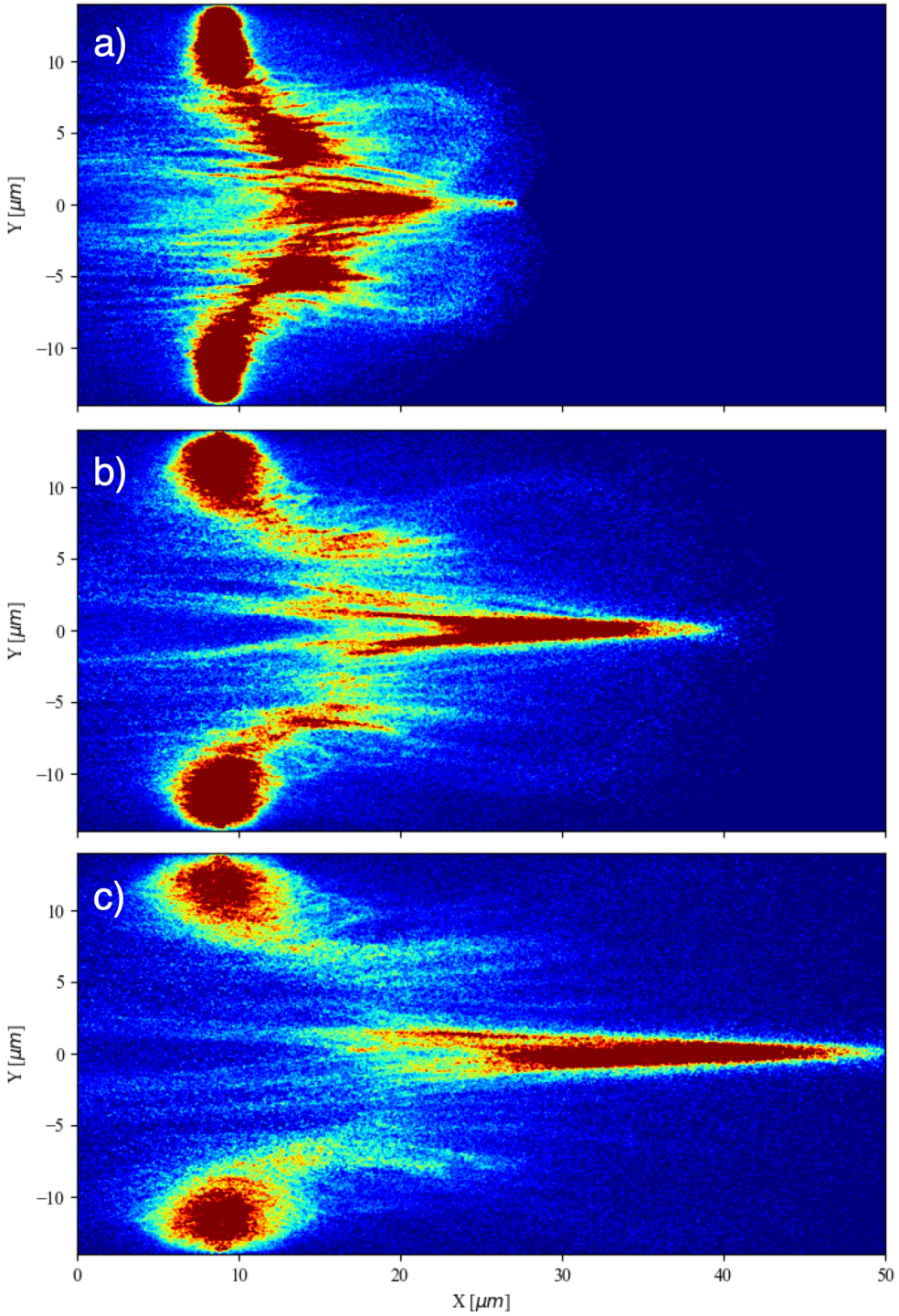

Figure A.15: The accelerated protons for a 8 beam approximation of a PFT 60° shown at a) $t = 350.2\ fs$, b) $t = 500.4\ fs$, and c) $t = 650.4\ fs$

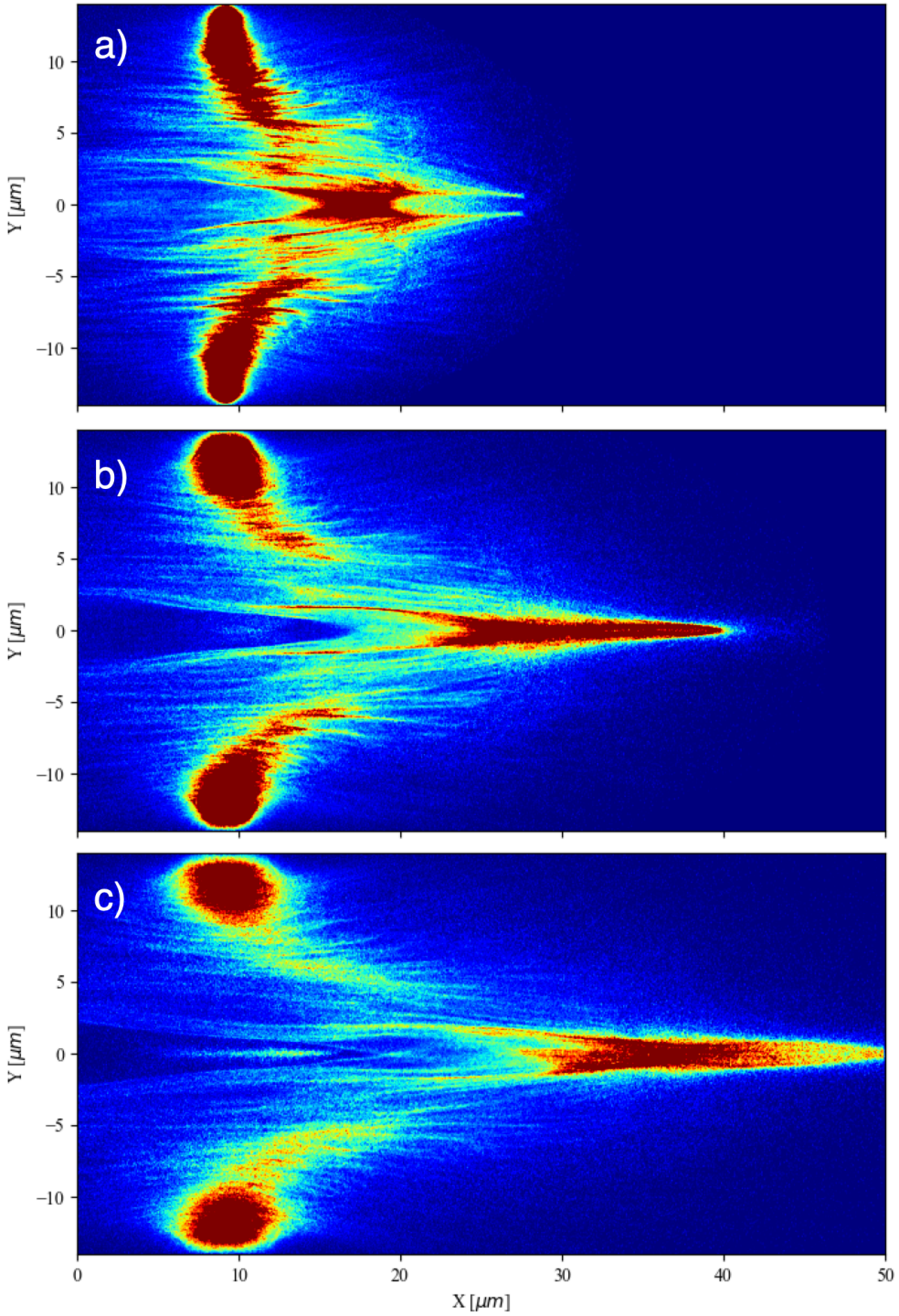

Figure A.16: The accelerated protons of the high resolution simulation for a PFT of 60° shown at a) $t = 350.2\ fs$, b) $t = 500.4\ fs$, and c) $t = 650.4\ fs$

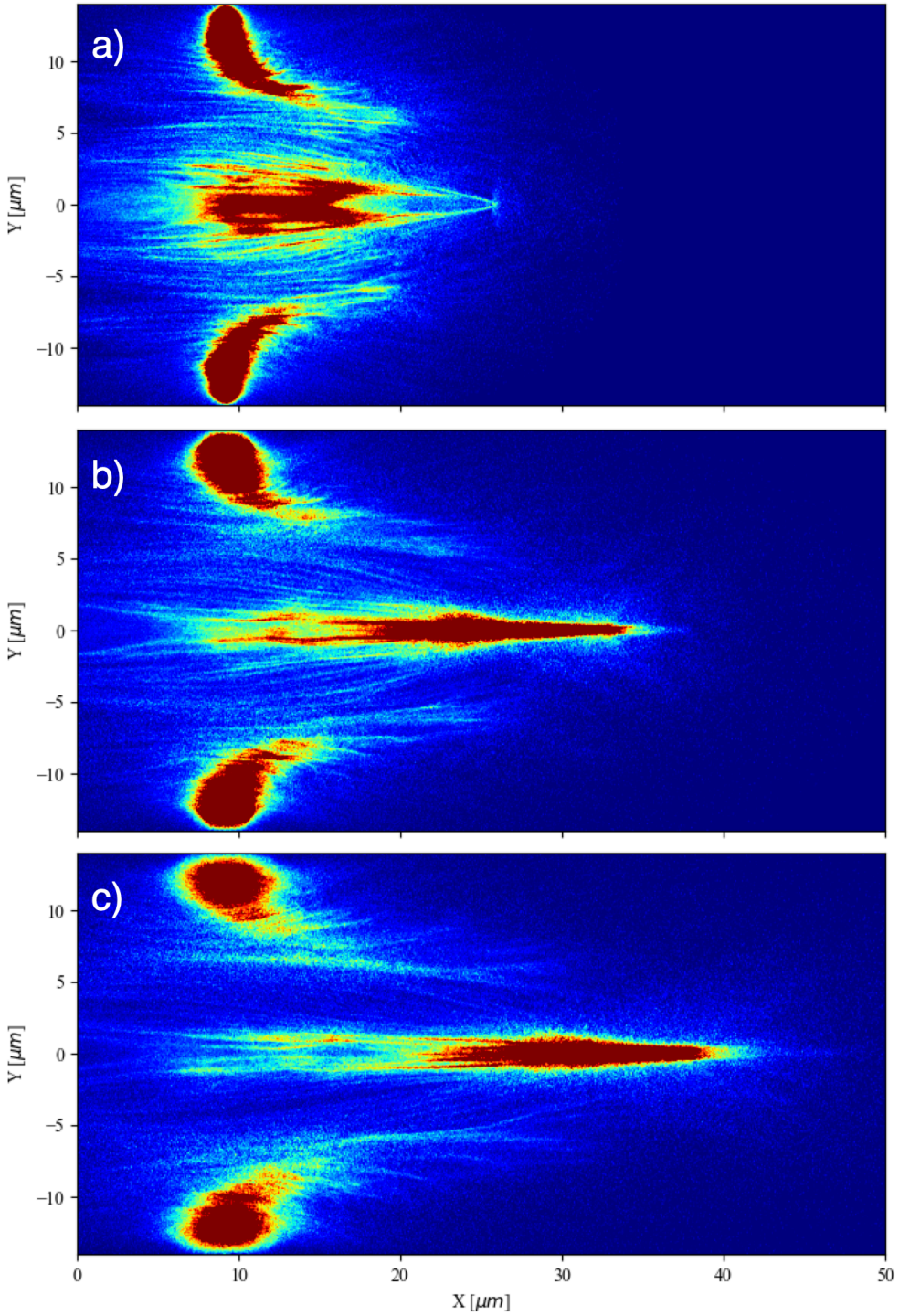

Figure A.17: The accelerated protons of the high resolution simulation for a 4 beam approximation of a PFT 60° shown at a) $t = 350.2\ fs$, b) $t = 500.4\ fs$, and c) $t = 650.4\ fs$